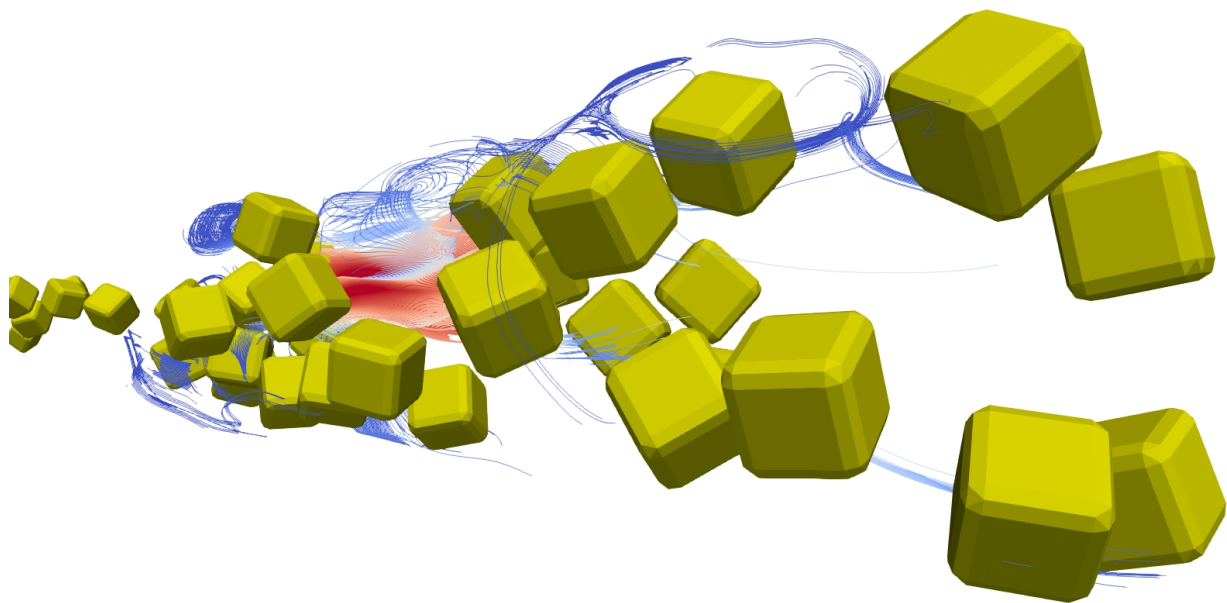# Simulations of Particle Integrity in Food Technology Related Flow

Simulation and modelling of deformable objects in a laminar constricting pipe flow with non-Newtonian fluid using Immersed Boundary Method

Alexander Backstam

This degree project for the degree of Master of Science in Engineering has been conducted at the Division of Fluid Mechancs, Department of Energy Sciences, Faculty of Engineering, Lund University and at Tetra Pak Processing Systems in Lund.

Supervisor at the Division of Fluid Mechanics was Professor Johan Revstedt.
Supervisor at Tetra Pak Processing Systems was Professor Fredrik Innings.
Examiner at Lund University was Professor Christoffer Norberg.

Simulations of Particle Integrity in Food Technology Related Flow

Simulation and modelling of deformable objects in a laminar constricting pipe flow with non-Newtonian fluid using Immersed Boundary Method

Author:
Alexander BACKSTAM

Supervisor:
Prof. Johan REVSTEDT
Prof. Fredrik INNINGS

July 9, 2019

LUND UNIVERSITY

Abstract

With an increasing demand for packaged food containing a variety of particles in the last decade has increased the expectations provided by processing systems. These particles ranges from products such as strawberry, potato, carrot, mango and everything in between. In order to satisfy the market need and retain the level of food quality and safety an expanded understanding of how to process these products is required. Today Tetra Pak Processing Systems is one of the worlds leading manufacturer and developer of food processing systems for liquid products containing particles. This master's thesis work, in collaboration with Tetra Pak, focuses on modelling and simulating large deformable cubic objects in a liquid flow through a pipe restriction.

The aim was to understand how particles behave and what stresses they are subjected to. The simulations were performed using the multiphase software IBOFlow. The chosen system was a simple pipe restriction using a non-Newtonian fluid. Parallel to this work, another master's thesis work was conducted with an experimental focus with similar goals. Collaboration and comparison between the different works were made throughout the entire thesis.

The particle size and flow situation was chosen to resemble the experiments. Simulations of a single and a high concentration of particles were performed. The developed simulation model was tested for its numerical stability and accuracy towards predicted stresses in the particles. A few issues were discovered which affected the authenticity towards reality. They were mended in various ways in order to obtain as high level of accuracy and authenticity as possible.

The particles were found to be subjected to a large variation in stress magnitude depending on situation and location in the pipe. Several different phenomena was identified that was considered to impact the particles and might affect their integrity. As the experimental results showed no significant sign of breakage of the particles, no definitive conclusion could be drawn towards the particles integrity. The simulation model did prove to be an adequate representation of reality and highlighted different areas of concern in the restriction pipe. The simulation model could be used in future work to great affect in order to understand the flow phenomena and particle behaviour in various systems.

Acknowledgements

I would like to express my gratitude towards the following people for their support during my work:

Firstly, I would like to thank my supervisors Johan Revstedt and Fredrik Innings. Thank you both for your help, guidance and interesting discussion that has aided and improved my work. The help with trying to explain and solve unexpected problems or complex phenomena has been greatly appreciated. Thank you to Andreas Mark and the developers of IBOFlow for your continuous support with simulations and expertise within multiphase systems. Many thanks to Michael Olsson who has always been there for me to discuss my ideas and thoughts with. It has helped me move forward in my work faster and with greater precision towards the final goal. Thank you to Jeanette Lindau for all you patience and help to always keeping me focused and with the main goal in mind. The colleagues at Tetra Pak are also acknowledged for all your assistance and providing me with a pleasant and fun work environment.

Lastly, it is difficult fully express my gratitude to you all, Thank you!

Contents

List of Figures

List of Tables

1

Introduction to the thesis

1.1 Background

Today, Tetra Pak processing systems is one of the worlds leading manufacturer and developer of food processing systems for liquid products containing solid particles, such as soup and yogurt. The costumer requirements are many and strict. The variation of particles ranges from strawberry to mango, potato, and everything in between. To maintain an edible product it has to be treated to the specifications. An important aspect is retaining the desirable texture of the product, this introduces added challenges. As particles are susceptible to breakage when exposed to an external load, the system has to be designed so that particles remain intact and with good quality all the way to packaged product. Tetra Pak has a diverse range of processing systems, modules and components for all types of products and requirements. Each processing line can be built to costumers specification with different modules and components. With a wide range of components the possible combinations in a processing line becomes vast. It is therefore vital to understand how each individual component interacts with the particles that might affects its quality. Tanks, pumps, heat exchangers, flow meters and valves are a couple of examples that are commonly used, with variations in design and specifications within each respective category. An example of how a Tetra Pak processing line might look is shown in figure 1.1. During processing the liquid product with submerged particles go through several different stages. These include heating, sterilization, filling and packaging to name a few. Each stage affects the particle in a different way.

As the demand for packaged food containing a variety of particles has increased in the last decade, it has increased the expectations on processing systems. It needs both to be efficient, gentle to particles and remain aseptic. In order to meet these requirements more knowledge and expertise in the area is needed. To achieve this deeper and increased understanding of what affects the integrity of a particle and its break mechanisms, both simulations and experiments has been conducted. The simulations focus on understanding the forces that each particle is subjected to. The response and effect depends on multiple different factors such as magnitude, area and volume affected, and type of phenomena. The experiments can reveal the magnitude of particle breakage and give an understanding of the breakage mechanism. By combining these two disciplines it is possible to obtain knowledge about the important factors and phenomena in which particles of different types are susceptible

to breakage.

To date there does not exist a complete simulation model for a multiphase system with deformable objects for food technology applications. The work in this thesis has been, in collaboration with Tetra Pak Processing Systems, to model a system capable of simulating these type of systems and components in a processing line for investigating the affects on the particles using the computational software IBOFlow.

Figure 1.1: Example of a processing line built by Tetra Pak.

1.2 Introduction

Multiphase flows is a common recurrence both in nature and industry. Their physical interaction and fundamental behaviour is well understood, but remains an area that has a large potential for development. There has been some recent development within this field, both improved understanding and simulation modelling efficiency. ANSYS, which is one of the most used commercial software for CFD calculations, introduced a static version of the immersed boundary method in 2009 with the purpose of decrease the difficulty of importing and simulating complex geometries. There does exists other softwares capable of predicting and simulating dynamic multiphase flows, where one of them is IBOFlow (Immersed Boundary Octree Flow), developed at Fraunhofer-Chalmers Centre (FCC) in Gothenburg, Sweden. The IBOFlow software is capable of simulating multiphase flows with dispersed deformable objects in a transient dynamic system. To date only a hand full of softwares in the world are capable of performing these types of simulations, where IBOFlow is one of them. It is a GPU based software thus using computational graphic cards to perform the computations. Most other commercially availabe software's use CPU computation, such as ANSYS and Star-CCM+. In theory, the GPU based computational software's can potentially achieve a higher efficiency in computation for large, transient, and complex dynamic systems as used in this thesis.

In many cases accurate numerical simulations are preferred and superior to experiments when considering efficiency, economics and understanding. Simulation allows for visualization and understanding of physical phenomena that would be difficult or impossible to observe from a physical experiment. It provides a diverse and flexible tool for testing and research with minimal resources required. The exponential increase in development in computational capabilities in recent years has made it possible to solve complex and nonlinear mathematical problems in a relatively short time. There has therefore been a shift of focus in resent years from performing time consuming and expensive experiments to a more simulation intensive use in both R&D and prototyping.

Parallel to this thesis work, another master thesis work was conducted by Roland and Tuck Hutasingh [26] within the same project and area at Tetra Pak with focus on the experimental procedure. The purpose of their work was to develop an experimental method for determining characteristics of particle integrity. A continuous collaboration between the associates were made in order to take advantage and utilize the separate knowledge and areas of expertise. At a later stage the results from both the experiments and simulation were compared with the objective of finding validation and further explain the individual findings and results. Different characteristic parameters used in the simulations to model the fluid and solid were extracted from performed experiments by Roland and Tuck Hutasingh.

1.3 Scope of the thesis

The goal of the thesis work was to model and validate a simulation model for a dynamic multiphase system using deformable objects with focus on particle integrity. To increase the validity of the simulations, comparison with the experiments were made, both using captured high speed videos and post-processing results. The purpose was to gain additional knowledge and insight into how fracture and breakage of various particle types occur and if it could be predicted from simulations. This requires it to accurately predict the forces, and in turn stresses, acting on particles as they pass through a component used in a processing line for various flow situations. The definition of particle integrity is varying from case to case and was customized and evaluated for each specific situation. In general, integrity refers to the degree of which the particle retain the desired quality and geometric shape. A particles integrity is influenced by many factors such as temperature, heat transfer, velocity, shape irregularities, surface roughness, interior imperfection or defects, etc. Due to limitations both in the computational software and time available a number of simplifications and omissions in the system were made.

The computational software IBOFlow that is used in the thesis has some limitations and therefore narrows the scope. To date a turbulence model that supports wall functions as objects collide has not been implemented and validated. Therefore only laminar flow cases was simulated.

As to not introduce too many physical phenomena and reduce computational cost the energy equation was excluded. This means that the system does not take temperature or heat transfer in to account, it therefore considered isothermic.
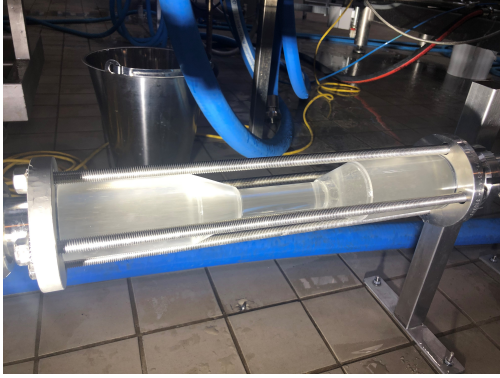
(a) Image of the 26 mm transparent pipe contraction rig mounted in the experiment

(b) Visualization of the 16 mm pipe from CAD drawing using PTC Creo.

Figure 1.2: Images of the pipe geometries used both in the experiments and simulations.

A major simplification regarding the particles were that they were considered as perfect bodies consisting of a hyper-elastic material. This means that any plastic deformation or fracture was not considered. They had a smooth surface, i.e no surface roughness, and were without shape irregularities or defects, either on the surface or interior.

To fully understand particle behaviour and what critical factors that affects is integrity, a simple pipe constriction was used both in simulation and experiments. A visualization of the pipe constriction is depicted in figure 1.2b. The reasoning behind this was to simplify the case in an effort to eliminate unnecessary complex behaviour due to the surrounding environment, to obtain a better understanding of the particles them-self. Similar types of pipe contractions can be found in industrial applications, such as flow meters. They do however in general have a lower slope angle and less contraction. The purpose for choosing a more harsh contraction was to observe more extreme cases. In theory this subjects the particle to a more severe conditions such that the experiments could in theory show breakage. It also increases the demand for accuracy and stability in the simulation.

As dynamic multiphase simulation with deformable objects is a relatively unexplored area, a major part of the work included investigation of stability and accuracy validation of the contact between solid phases. No previous work was found on this using the IBOFlow software.

The parallel thesis work by Roland and Tuck Hutasingh performed experiments on the same configuration as made in the simulations. For the experiment a transparent contraction rig was manufactured out of PMMA acrylic plastic. The mechanical properties of the different particle samples was determined in the experiments. During the experiment a high speed video camera captured videos as the particles flow through the transparent contraction rig. An image of the transparent contraction rig set-up in the experiment can be seen in figure 1.2a.

2

Introduction to multiphase simulation

In this chapter an introduction and background to multiphase simulations of large objects will be presented. The purpose is to give the reader a brief insight into how multiphase simulations are treated in general together with previous work in the field. The definition of a multiphase system is a domain that contains two or more phases separated by a distinct interface. Common systems are gas-liquid and solid-liquid, where gas bubbles or solid objects respectively are surrounded by a liquid. It does also includes liquid-liquid systems where the liquids are immiscible, such as water and oil. As the work in this report focuses on large deformable particles the presented methodology framework is for application within this specific area.

2.1   Fluid Structure Interaction (FSI)

Fluid-Structure Interaction (FSI) refers to the interaction between a fluid and solid structure in a multiphase system. It is a collection of various methods of describing the phenomena. The purpose is to combine two separate disciplines, finite element solid/structural analysis and finite volume fluid analysis. The difficulty of this is to accurately capture the complex interaction of the multiple phases. In order to achieve this, it is essential to resolve the spacial length and time scales on a small scale close to the fluid-structure interface. Direct Numerical Simulations (DNS) are therefore advantageous from an accuracy perspective. The advantage of true DNS is no approximations are used and solves the full Navier-Stokes equations directly, but it is however very computationally expensive compared with other available methods [12].

FSI can be classified into two sections, conforming and non-conforming mesh. In a conforming mesh the elements are adapted to fit the structural domain by having the nodal points on the interface. The non-conforming mesh is, on the other hand, not adapted to the structural domain. This means that the element nodes are not exclusively placed on the interface between the phases. The two variations of mesh method is depicted in figure 2.1.

(a) Conforming mesh   *(b) Non-conforming mesh*
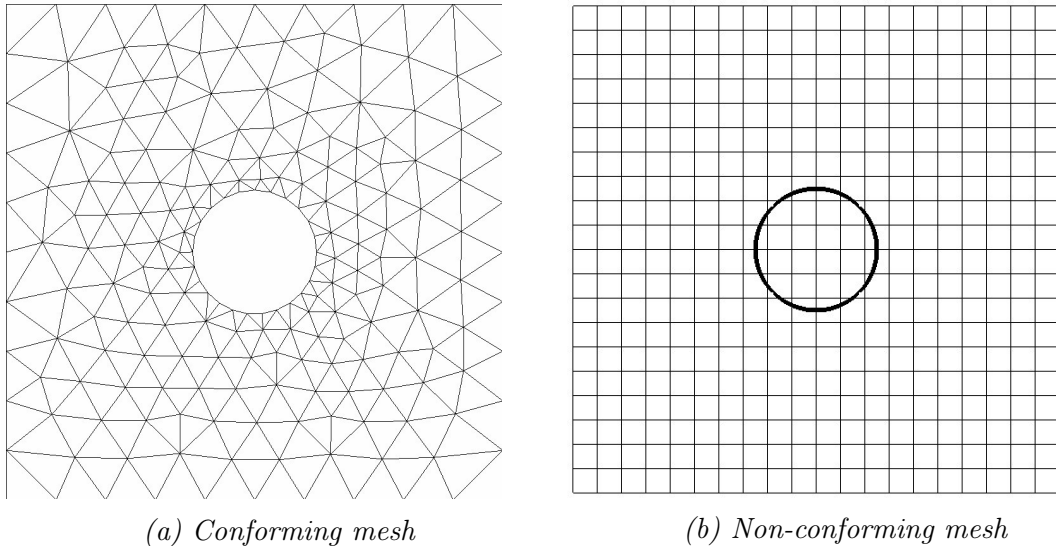
Figure 2.1: Example of conforming and non-conforming mesh [24].

Two seperate approaches of solving a FSI system exists, monolithic or partitioned approach. In the monolithic approach the governing equations for each phase are treated in the same mathematical framework. This constitutes a single system of equations, for both fluid and structure, and therefore only requires a single matrix for solving the system.

In the partitioned approach the governing equations for each phase are solved separately as individual problems with their own mathematical framework. They are then coupled by an algorithm that communicate explicitly or semi implicitly to ensure system continuity.

The monolithic approach can potentially achieve higher accuracy and stability for multiphase systems, but might require more resources and expertise to develop an algorithm to accurately treat a multidisciplinary problem. Since it treats the problem in one framework the interface is solved implicitly and only requires a single matrix. The drawback is that the matrix can become quite large even for simple problems which might be computationally expensive. The partitioned approach is an effective method of dealing with multidisciplinary problem and has the possibility of catching the detailed physics along the fluid structure interface. The drawback of the method is the high dependence on coupling algorithms. They can prove difficult to develop and implement with satisfactory accuracy and stability with minimal computational effort. [17, 24].

Within FSI there exists several methods for dealing with the interface between the different phases, where Immersed Boundary (IB) is one of them. IB is a collection name that consists of several subsets and employs a non-conforming mesh. The most common subsets are Immersed Boundary Method (IBM) and Immersed Domain Method (IDM). The difference between the methods are that the IBM does not cover a finite volume in space and the fluid domain becomes the entire computational domain. The IDM on the other hand does cover a finite volume in space where the motion in of the IB is simulated. To extend the fluid to the entire computational domain the IB is filled with an artificial fluid [17]. A visual representation of IBM

and IDM can be seen in figure 2.2 As the work done in the thesis is regarding IBM no further description of discussion will be done on IDM.
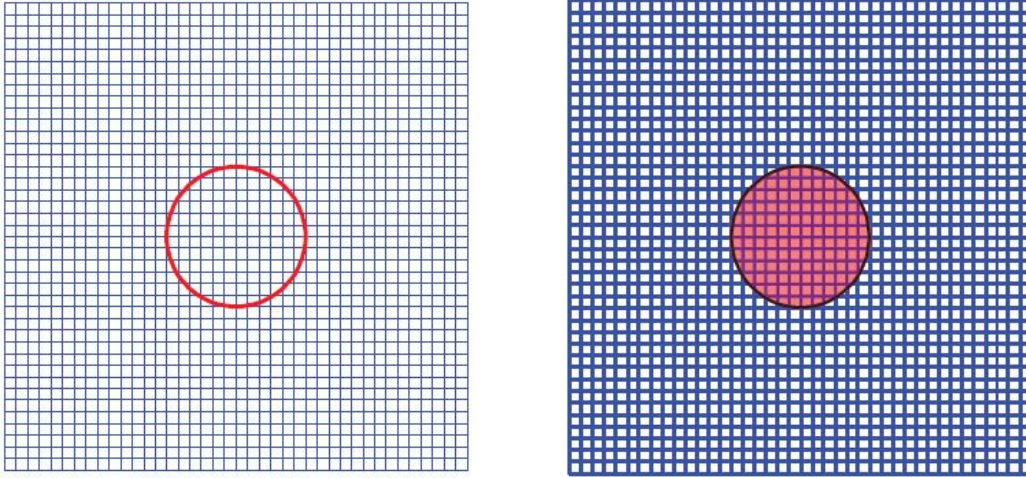
(a) Immersed boundary method

(b) Immersed domain method

Figure 2.2: Example of different types of immersed boundary methods.

The Immersed Boundary Method was originally formulated by Peskin [3] as a numerical method for analyzing the blood flow around a human heart valve. The purpose was to capture the the interaction between the blood flow and the heart valve during its motion of opening and closing during a heart beat. Peskin did this by replacing the boundary with a field of forces which was defined on the mesh points and calculated from the boundary configuration.

Since then other methods within FSI has been further developed and improved. Hu proposed in 1996 a method of accurately simulating fluid-solid flow by using the arbitrary Lagrangian-Eularian (ALE) method [6, 9]. The idea was to create an unstructured conforming mesh around the solid phase particle that was adapted as the particle moved through space. This produced good results with good accuracy but required re-meshing at each time step, which was cumbersome and computationally expensive.

To avoid this, Kalitzin and Iaccarino (2003) presented a Cartesian method or cell-splitting method of dealing with this. The name cell-splitting comes from the effect of the immersed boundary "splitting" the cells which creates a non-conforming mesh. This avoids the need for re-meshing at each time step, but requires some method of extrapolating information and boundary conditions between the cell faces and the two phase interface and vise-versa.

The Mirroring Immersed Boundary method (MIB) has been developed by Mark and Wachem [12, 15] as an extension of the IBM. The MIB mirrors the velocity field over the immersed boundary so that the fluid flow follows the surface of the body. This results in a generated fictitious velocity field inside the immersed boundary. This has in previous IB implementations created nonphysical mass flux across the boundary. In the implementation by Mohd-Yusof (1997), a source term was added to the continuity equation to mend this error. The MIB implementation in IBOFlow

excludes the fictitious velocity field from the continuity equation and corrects any mass flux that might occur. This eliminates any mass flux across the IB and the need for a corrective source term. Therefore the method does not generate any non-physical oscillations around the IB and is implicitly formulated with second-order accuracy in space.

3

Theory

3.1 Fluid dynamics

3.1.1 Governing equations

For a fluid in a continuum, the motion is described by the conservation equations, known as the governing equations. The governing equations for a general case include conservation of mass, conservation of momentum, conservation of energy and equation of state. For an incompressible fluid, meaning a constant density, this results in a decoupling of conservation of mass and conservation of momentum from conservation of energy. The equation of state is also removed due to this assumption.

The conservation of mass for an incompressible fluid is stated as

$$\frac{\partial u_i}{\partial x_i} = 0 \quad , \tag{3.1}$$

and conservation of mass is given by

$$\rho\frac{\partial u_i}{\partial t} + \rho u_j \frac{\partial u_i}{\partial x_j} = -\frac{\partial p}{\partial x_i} + \frac{\partial \tau_{ij}}{\partial x_j} + \rho g_i \tag{3.2}$$

The stress tensor, τ_{ij}, for incompressible flow is given by

$$\tau_{ij} = \mu \left(\frac{\partial u_i}{\partial x_j} + \frac{\partial u_j}{\partial x_i} \right) \quad , \tag{3.3}$$

where μ is the dynamic viscosity of the fluid. For non-Newtonian fluids there exists many different ways of describing the viscosity. In this work the viscosity of the fluid is described by a power law as

$$\mu = K\dot{\gamma}^{n-1} \quad , \tag{3.4}$$

where K and n are constant parameters and $\dot{\gamma}$ is the shear rate of the fluid.

3.2 Structural Solver

In order to solve the deformable structural domain it is discretized using a finite element discretization with total Lagrangian formulation used to predict the motion

of the structure. The Newmark time stepping scheme is employed in the temporal discretization.

3.2.1 Total Lagrangian

The total Lagrangian formulation uses the nodal displacement field and originates from the virtual work, $\mathcal{V}$, equations. The term "virtual" comes from the thought of a small imaginary displacement provided by the work done by a force (virtual work). For the system to be in equilibrium the internal and external virtual work needs to be equal.

$$\mathcal{V}(\boldsymbol{u}, \delta\boldsymbol{u}) = \mathcal{V}_{\text{int}} - \mathcal{V}_{\text{ext}} = 0 \tag{3.5}$$

Where $\boldsymbol{u}$ is the nodal displacement and $\boldsymbol{\delta u}$ is the nodal incremental displacement. By introducing the balance of linear momentum in a continuum it is given by [19]

$$\nabla \cdot \boldsymbol{\sigma} + \rho\boldsymbol{b} - \rho\boldsymbol{a} = \boldsymbol{0} \tag{3.6}$$

Where $\boldsymbol{\sigma}$ is the Cauchy stress tensor, $\boldsymbol{b}$ is the volume forces, e.g gravity, $\boldsymbol{a}$ is the acceleration, ρ is the density and ∇ is the divergence operator. In continuation, the weak form (3.7) can be formulated as the spatial virtual work by following the steps presented by Krenk [13]. The formulation becomes as [19]

$$\delta\mathcal{V} \int_V (\nabla \cdot \boldsymbol{\sigma} + \rho\boldsymbol{b} - \rho\boldsymbol{a}) \cdot \delta\boldsymbol{v} dV = 0 \quad , \tag{3.7}$$

where $\delta\boldsymbol{v}$ is an arbitrary incremental virtual velocity and V denotes the volume of the current configuration. The Cauchy stress tensor can be described using the second Piola-Krichhoff stress tensor, $\boldsymbol{S}$, as

$$\boldsymbol{\sigma} = J^{-1}\boldsymbol{F} \cdot \boldsymbol{S} \cdot \boldsymbol{F}^T \tag{3.8}$$

Where $\boldsymbol{F}$ is the deformation gradient and J is the Jacobian, defined as $J = det(\boldsymbol{F})$. Using the deformation gradient the Green strain can be formulated as

$$\boldsymbol{E} = \frac{1}{2}\left(\boldsymbol{F}^T\boldsymbol{F} - \boldsymbol{I}\right) \quad , \tag{3.9}$$

where $\boldsymbol{I}$ is the second order identity tensor. For a more detailed and extensive explanation on the total lagrangian formulation the reader is referred to the book by Krenk [13].

3.2.2 Material models

In this section the mathematical formulation of the two material models used to model the solid particles are presented. For both material models the second Piola-Kichhoff stress tensor is formulated from the strain energy density and coupled with (3.8) in the total Lagrangian formulation. The defining material parameters are the Young's modulus, E, and Poisson's ratio, ν. The particles are assumed to be isotropic and without any imperfections, cracks or voids.

The St. Venant Kirchhoff material model is based on linear elasticity with a isotropic

constitutive relation together with the Piola-Kirchhoff stress. It is one of the most widely used material models due to its simplicity and stability. It is a non-linear hyperelastic material model used to predict large deformations [8].

The non-linear Neo-Hookean material model is a hyper-elastic material model commonly used to model materials such as polymers or rubber. In previous work it has been used to model and predict various phenomena and stress-strain response in rubber-like materials with good agreement to physical experiments [25, 21].

St. Venant Kirchhoff

A St. Venant Kirchhoff material is described using the strain energy density in (3.10).

$$\Psi = \frac{1}{2}\lambda \left(tr\boldsymbol{E}\right)^2 + \mu \boldsymbol{E} : \boldsymbol{E} \tag{3.10}$$

The Lamé model parameters λ and μ can be described using the Young's modulus, E, and Poisson's ratio, ν, as

$$\begin{cases} \lambda = \dfrac{E\nu}{(1+\nu)(1-2\nu)} \\ \mu = \dfrac{E}{2(1+\nu)} \end{cases} \tag{3.11}$$

By using the expression of the strain energy density (3.10) the second Piola-Kirchhoff stress tensor can be formulated as

$$\boldsymbol{S} = \lambda \left(tr\boldsymbol{E}\right)\boldsymbol{I} + 2\mu\boldsymbol{E} \tag{3.12}$$

Neo-Hookean

The strain energy density for a Neo-Hookean material is defined as

$$w = \frac{1}{2}K\left[\frac{1}{2}(J^2-1) - \ln(J)\right] + \frac{1}{2}\mu(J^{-2/3}tr(\boldsymbol{C}) - 3) \quad, \tag{3.13}$$

where the Lamé parameters K (bulk modulus) and μ (shear modulus) can be described using the Young's modulus and Poisson's ratio as

$$\begin{cases} K = \dfrac{E}{3(1-2\nu)} \\ \mu = \dfrac{E}{2(1+\nu)} \end{cases} \quad, \tag{3.14}$$

and $\boldsymbol{C}$ is the Cauchy-Green deformation tensor

$$\boldsymbol{C} = \boldsymbol{F}^T \cdot \boldsymbol{F} \tag{3.15}$$

The second Piola-Kirchhoff stress tensor can be formulated for a Neo-Hookean material as

$$\boldsymbol{S} = \frac{K}{2}(J^2-1)\boldsymbol{C}^{-1} + \mu J^{-2/3}(\boldsymbol{I} - \frac{tr\boldsymbol{C}}{3}\boldsymbol{C}^{-1}) \tag{3.16}$$

3.2.3 Newmark Scheme

The temporal discretization of the governing equation used to resolve the system was done with the Newmark algorithm. It is a time stepping algorithm for dynamic systems developed by Newmark [2]. The differential equations that governs the dynamic response of a system can be written as

$$\boldsymbol{M\ddot{x}}^{n+1} + \boldsymbol{C\dot{x}}^{n+1} + \boldsymbol{Kx}^{n+1} - \boldsymbol{f}_{ext(n+1)} = \boldsymbol{0} \tag{3.17}$$

where $\boldsymbol{M}$ is the mass tensor, $\boldsymbol{C}$ is the damping tensor, and $\boldsymbol{K}$ is the stiffness tensor. The superscript $n+1$ refers to the subsequent time step and n refers to the most recent found equilibrium state. The Newmark scheme uses predictions for the nodal velocity and position as an initiation state, formulated as

$$\begin{cases} \boldsymbol{\dot{x}}_s^{n+1} = \boldsymbol{\dot{x}}_s^n + \Delta t \left[(1-\gamma)\,\boldsymbol{\ddot{x}}_s^n + \gamma\boldsymbol{\ddot{x}}_s^{n+1} \right] \\ \boldsymbol{x}_s^{n+1} = \boldsymbol{x}_s^n + \Delta t\boldsymbol{\dot{x}}_s^n + \frac{1}{2}\Delta t^2 \left[(1-2\beta)\,\boldsymbol{\ddot{x}}_s^n + 2\beta\boldsymbol{\ddot{x}}_s^{n+1} \right] \\ \gamma \in [0,1] \text{ and } \beta \in [0,1/2]\,, \end{cases} \tag{3.18}$$

where β and γ are constants. The nodal position and velocity of the previous equilibrium state is assumed to be known. In order to achieve numerical stability using the Newmark scheme the constants β and γ need to meet the following requirements.

$$\gamma \geq \frac{1}{2} \quad \text{and} \quad \beta \geq \frac{1}{2}\gamma \tag{3.19}$$

If they are set to $\beta = 1/4$ and $\gamma = 1/2$ it is known as the trapeziodal rule or constant average acceleration method. If they are selected as $\beta > 1/4$ and $\gamma > 1/2$, this results in numerical damping of the system acting on low frequencies of wave propagation. A representation of this can be seen in figure 3.1. The term wave propagation refers to the transfer and distribution of information and energy inside a solid material. For more explanation and insight into the Newmark method and algorithm the reader is referred to Krenk [13].

The Newmark algorithm retains full response of high frequency components of propagation. This may introduce complications such as build of energy in the system which might lead to noise in the solution and convergence problems. In order to prevent this, a cut-off frequency is added such that the frequencies above the limit is filtered out and the frequencies below the limit retain close to full response [13]. There are multiple methods of achieving this. In this thesis work, the Rayleigh damping method is used in the numerical implementation for damping ranges of frequencies.
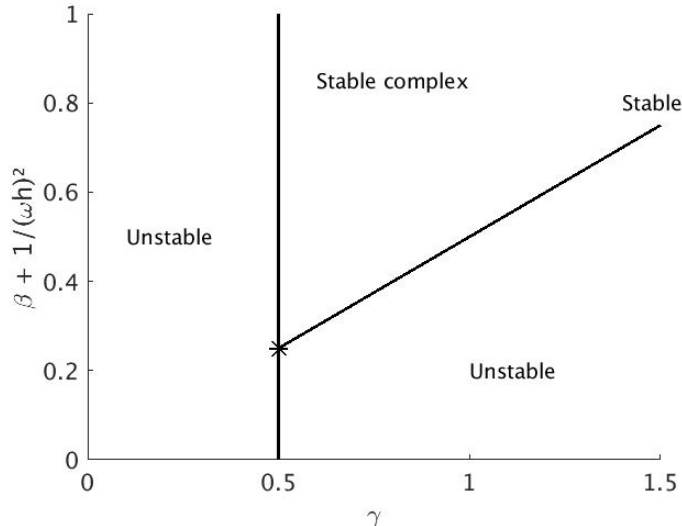
Figure 3.1: Stability diagram for the Newmark algorithm. ω is the frequency and h is the timestep length.

3.2.4   Rayleigh damping

Rayleigh damping is a form of structural damping of propagation waves within a solid material. The purpose is to a certain extent damp different intervals of wave frequencies. It is formulated using the mass tensor, $\boldsymbol{M}$, and the stiffness tensor, $\boldsymbol{K}$, in (3.20).

$$\boldsymbol{C} = \alpha\boldsymbol{M} + \beta\boldsymbol{K} \quad , \tag{3.20}$$

where α and β are damping coefficients, known as Rayleigh damping coefficients, that are selected depending on system and material. The damping ratio, ζ_d is defined using the Rayleigh coefficients as

$$\zeta_d = \frac{1}{2}\left(\beta\omega + \frac{\alpha}{\omega}\right) \tag{3.21}$$

As can be seen in (3.21) α and β will increase the damping ratio on low and high frequencies respectively [20, 22].

3.3   Particle treatment

In this section the theory and mathematics behind how the particles are treated in the simulation will be presented. It contains the fluid structure coupling and methodology of the used IBOFlow software.

The definition of a two-phase flow is a system containing two media with different physical properties, this includes fluids, solids, and media with different viscoelastic properties. The formulation varies depending on the type of media that is modelled. The Eulerian formulation is constructed with a reference stationary control volume with finite space. This is seen as the observer is stationary in space and the observational media moves through space. This is implemented in all commercial computational fluid dynamics (CFD) codes and mainly used for simulation of fluid

flows. The Lagrangian formulation is, on the contrary, defined as the observer fixed to the observational media and follows its path through space. This is mainly used for simulation of solid materials in Finite Element Method (FEM) codes.

3.3.1 Fluid Structure Interaction (FSI)

The entire considered computational domain, denoted as Ω, is bounded by the boundary Γ. Within the computational domain the structural domain, Ω_s, and the fluid domain, Ω_f exists. The interface between the two phases is denoted as Γ_s such that the two phases are separate as $\Gamma_s = \Omega_s \cap \Omega_f$, see figure 3.2. Each phase has their own governing equation, as presented in previous sections. The following presented equations are used to determine the interaction between the different phases.
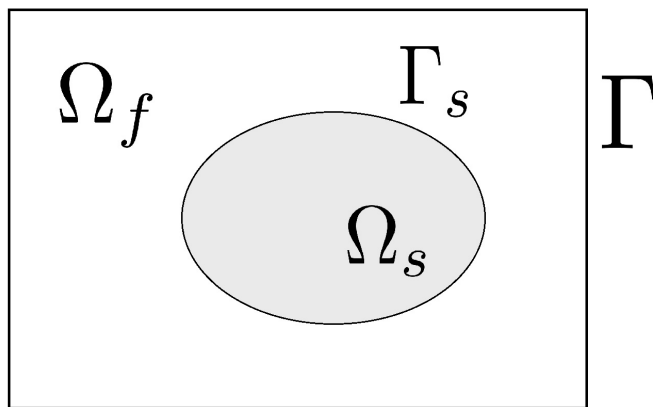
Figure 3.2: Representation of computational domain in FSI formulation.

The D'Alembert's principle is used to formulate the equations of motion for the fluid and structure as

$$\rho \frac{\partial^2 u_i}{\partial t^2} - \frac{\partial \sigma_{ij}}{\partial x_j} + f_i = 0 \quad , \tag{3.22}$$

where u_i is the displacement and f_i is the body force, such as gravitational force. It can be written for the structural domain as

$$\rho^s \frac{\partial^2 u_i^s}{\partial t^2} - \frac{\partial \sigma_{ij}^s}{\partial x_j} + f_i^s = 0 \quad , \tag{3.23}$$

where the superscript s denotes the solid phase. Depending on the material model of the structural domain the stress, σ_{ij}, will be defined differently. This will be presented later in section 3.2.2. In similar way the equation of motion for the fluid phase can be written as

$$\rho^f \frac{\partial^2 u_i^f}{\partial t^2} - \frac{\partial \sigma_{ij}^f}{\partial x_j} + f_i^f = 0 \quad , \tag{3.24}$$

Similar to fluid interaction with walls, the no-slip condition along the interface, Γ_s, is enforced. The Dirchlet boundary condition states that the fluid and solid velocity at the interface must be equal,

$$\dot{u}_i^s = \dot{u}_i^f \quad \text{on } \Gamma_s \tag{3.25}$$

The Neumann condition states that the stress should be equal on the fluid and solid at the interface,

$$\sigma_{ij}^s n_i = \sigma_{ij}^f n_i \quad \text{on } \Gamma_s \tag{3.26}$$

3.4 Immersed Boundary Method

The Immersed Boundary Method used in IBOFlow is a cell-splitting method that uses a structured non-conforming mesh grid. Cell-splitting refers to the occurrence of the discrete sharp IB passing through fluid cells, depicted in figure 3.3. The interaction between each phase is represented by a Lagrangian force, calculated either explicitly from the momentum equations or by enforcing a boundary condition at exactly the IB [12].

3.4.1 Mirroring Immersed Boundary

In the Mirroring Immersed Boundary method the cells are divided into one of four classifications. At the immersed boundary extrapolation and mirror cells are defined. Extrapolation cells are defined as cells with the center of the cell outside of the IB with a minimum distance of one half cells size from the IB. Mirror cells are cells with their center inside the IB with a minimum distance of one and a half cells size to the IB. The remaining cells outside the IB are classified as fluid cells and the remaining cells inside the IB are classified as interior cells. This classification is extended in all three dimensions. A representation of these classifications can be seen in figure 3.3.
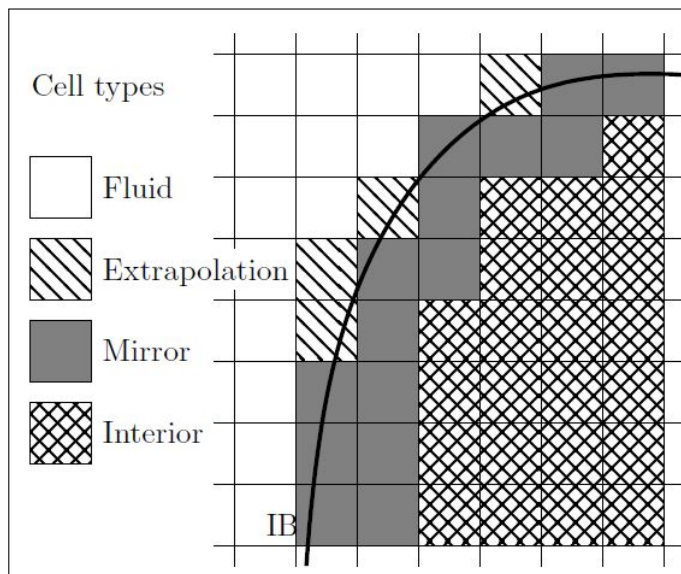
Figure 3.3: Representation of the four different classifications of cells when using Mirroring Immersed Boundary [15].

Mirroring Immersed Boundary Condition

The discrete Interior Immersed Boundary (IIB) point ,$\vec{r}_{iib}$ is mirrored outside of the IB as the point, $\vec{r}_e$. The positions of $\vec{r}_e$ is determined by the normal of the triangle plane closest to $\vec{r}_{iib}$. From this the point on the IB $\vec{r}_{ib}$ is determined as the point where the line between $\vec{r}_e$ and $\vec{p}_{iib}$ crosses the IB, see figure 3.4. The velocity at the exterior point is set by trilinear interpolation. The interior velocity $\vec{u}_{iib}$ is determined by interpolation of the velocity at the exterior point, $\vec{u}_e$, and at the IB, $\vec{u}_{ib}$ by

$$\frac{\vec{u}_{iib} + \vec{u}_e}{2} = \vec{u}_{ib} \tag{3.27}$$

The Dirchlet boundary condition (3.25) is enforced on the IB and thereby the reversed IIB velocity can be determined, as in figure 3.4. To avoid existence of mass flux across the IB due to the fictitious velocity field it is excluded in the continuity equation. This can however created oscillations of mass flux across the IB. To mend this the Neumann boundary condition (3.26) is enforced on the IB. This results in a decreased mass flux due to zero pressure force over the IB, however some minor mass flux might still exist.
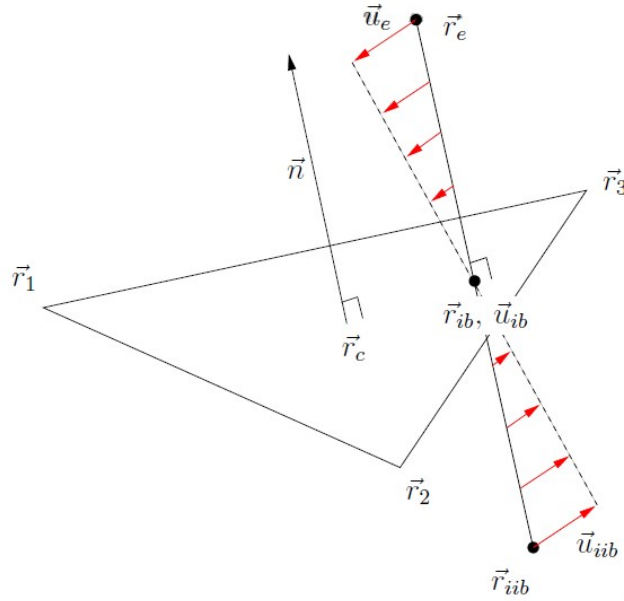
Figure 3.4: Three-dimensional visualization of the immersed boundary and the generated mirrored velocity field [12]. The points are denoted as $\vec{r}$ and velocities as $\vec{u}$.

Hybrid Immersed Boundary Condition

The hybrid immersed boundary condition uses both mirroring and extrapolation of the velocity field. By trilinear interpolation the velocity of the fluid is projected to an fictious exterior point, $\vec{p}_{ex}$, with the velocity $\vec{u}_{ex}$, see figure 3.5. The velocity is set to the mean of the velocity of the exterior point, $\vec{p}_e$, and the point on the immersed boundary, $\vec{u}_{ib}$. The condition reads

$$\frac{\vec{u}_{ib} + \vec{u}_e}{2} = \vec{u}_{ex} \tag{3.28}$$
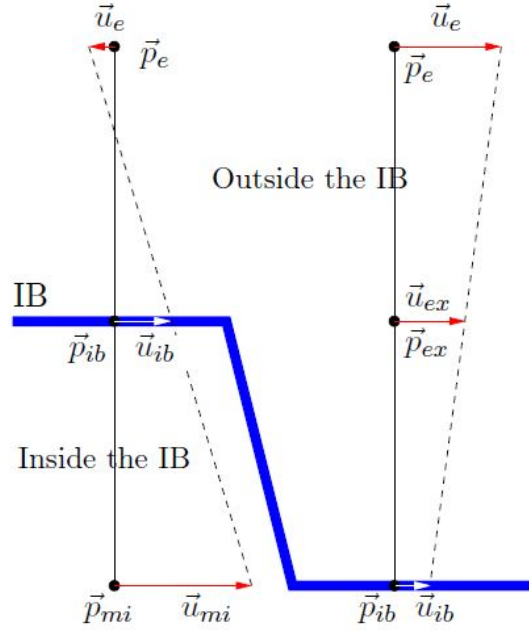
Figure 3.5: Two-dimensional visualization of the hybrid immersed boundary condition and the generated mirrored velocity field [15]. The points are denoted as $\vec{p}$ and velocities as $\vec{u}$.

3.5 Contact Models

In this section the numerical treatment and modelling of contact between solid objects in a multiphase system will be presented. A short explanation of a multibody system is also given.

3.5.1 Multibody systems

A dynamic multibody system is comprised of several interconnected bodies that experience large translations and rotations. In order to resolve the complex physical behaviour in a multibody system, a number of simplifications are made. This is obtained by using mathematical expressions for individual components, e.g springs, dampers, rotational joints or external forces, in superposition with each other. An abstract representation of a multibody system depciting some of the most common components used in modelling can be seen in figure 3.6.
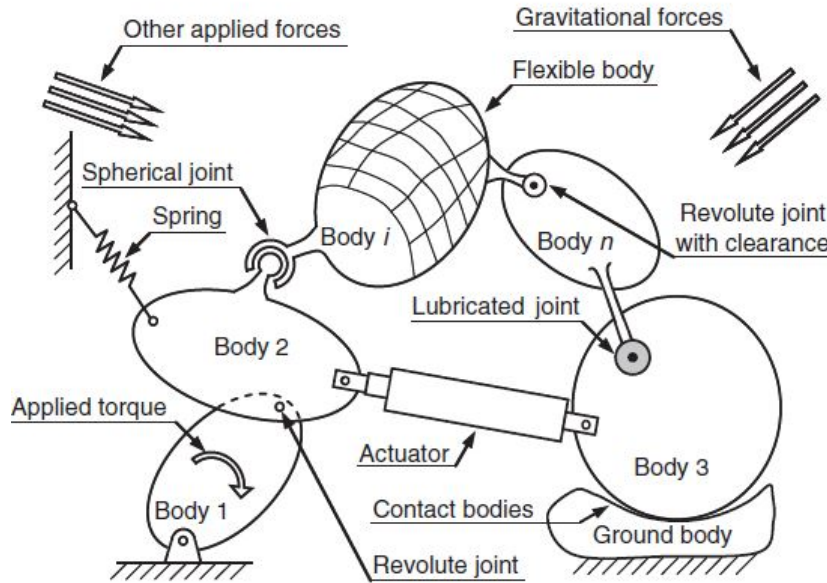
Figure 3.6: Abstract representation of a multibody system with some of the most relevant parts [18].

3.5.2 Contact Kinematics

Generalized contact kinematics between two bodies uses the vector position of each body in space, r_i and r_j, and the vector position of the contact point, r_i^P and r_i^P, to describe the contact interaction. For each body a contact point is defined, P_i and P_j that are separated by a distance d if not in contact or δ if in contact. During contact the bodies overlap which creates an indentation or penetration, denoted as δ. A representation of two bodies before and after contact can be seen in figure 3.7a and 3.7b.

(a) Before contact.   *(b) During contact with indentation δ.*
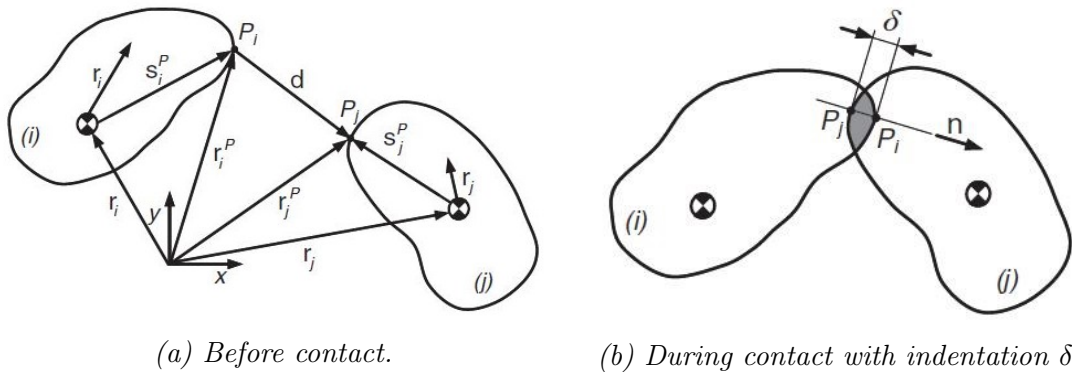
Figure 3.7: General representation of two bodies before and during contact [18].

3.5.3 Hertz Contact Model

The deformable particles utilizes the Hertz contact model with a nonlinear power law function to describe the contact interaction between two or more objects. The contact model is purely elastic without any damping and the contact force acting on and between each object during contact is formulated as

$$F = K\delta^n \quad , \tag{3.29}$$

where K is a stiffness scalar, n is a constant and δ is the indentation as depicted in figure 3.7b. The stiffness K is formulated using the mass of each object, m_i, the contact time, δ_t, and characteristic contact area, A_c.

$$\begin{cases} K = \dfrac{M\pi^2}{\delta_t^2 A_c} \\ M = \dfrac{1}{1/m_1 + 1/m_2} \end{cases} \tag{3.30}$$

4

Computational software

In this chapter the computational software IBOFlow that was used in the thesis work will be presented together with previous work done using IBOFlow.

4.1 IBOFlow

The numerical software used to perform the computational simulations in the thesis was IBOFlow (Immersed Boundary Octree Flow Solver), developed by Fraunhofer-Chalmers at Chalmers univeristy in Gothenburg, Sweden. It is an incompressible finite volume fluid flow solver for multiphase systems. Octree refers to the architectural structure of the mesh grid. It is built up a structured grid in hierarchies that are extended downwards depending on the level of refinement in the grid. A visual representation can be seen in figure 4.1
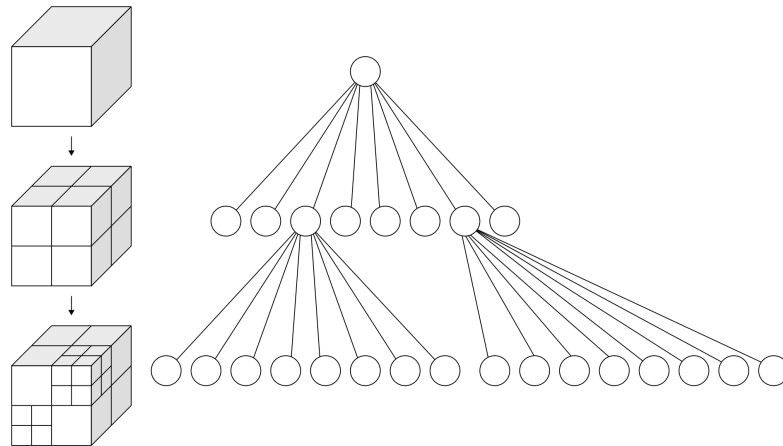
Figure 4.1: A visual representation of the hierarchical structure that builds up an octree mesh grid [14].

The software uses the mathematical framework presented in chapter 3, where the Navier Stokes equations are coupled with the SIMPLEC [4] method which relates the velocity and pressure fields. The Mirror Immersed Boundary was used to treat the multiphase system of fluid and particles. The temporal discretization of the system was made by the explicit second order finite difference Crank and Nicolson [1] time scheme.

4.2   Previous work in IBOFlow

In the master thesis work by Ottosson [24], he presents the numerical stability and accuracy of the IBOFlow software by the use of different coupling methods in FSI. In his work a rigid sphere attached to a spring was simulated with low Reynolds number to take advantage of the existence of an analytical solution for the drag coefficient of the system. The simulations were performed with minimum cell size of 0.04D, where D is the diameter of the sphere, different values for β and a CFL number of approximately 1. The results showed good agreement with minor oscillations of the numerical solution compared to the analytical solution. This is in accordance with the rule of thumb that the cell size should be in the approximate range $0.03D < L_{cell} < 0.06D$. L_{cell} denotes the maximum side length of a cell close to the boundary. Of course the grid can be refined with $L_{cell} < 0.03D$ but this might not lead to more accurate results and increases the computational cost without any benefit.

In similar work presented by Mark and Wachem [12], the MIB method used in IBOFlow was tested in Reynolds number up to 1000 with respect to its validity and accuracy. A rigid stationary sphere, with diameter D, was used to to numerically calculate the drag and pressure coefficient across the surface in a steady state solution. Their results showed that the value of the coefficient has only minor changes when altering from $0.024D$ to $0.08D$ in cell size. Meaning that the method is stable for a large range om cell sizes. However large deviations can be seen in a transient solution for various grid sizes. The numerical solution for $L_{cell} = 0.125D$ and $L_{cell} = 0.2D$ stabilizes and converges at apporximately the same value. This shows that the method can be accurate for cell size large than $0.06D$ for simple cases.

This was further studied and validated by Mark, Rundqvist, and Edelvik [15] for Reynolds up towards 1000. The drag coefficient was used, as in previous studies, and the response of a sphere when released into a free vertical fall. Grid sizes down towards $L_{cell} = 0.03D$ showed good accordance and accuracy compared with analytical solutions.

In the work presented by Förster, Wall, and Ramm [11] showed that FSI implementations might be sensitive to low density ratios between the solid and fluid phase ($\rho_r = \rho_s/\rho_f$). In later work done by Kim, Lee, and Choi [23] a coupling method and implementation was proposed and evaulated with the aim of mending the issues with instabilities for low density ratios. A solid sphere with an elastic bar attached at the back was simulated in a fluid flow with density ratios ranging from 2.3 to 0.3. Their implementation proved efficient and stable in terms of computational cost and convergence respectively for ratios well below unity. The same method was implemented in IBOFlow and tested using the same set-up in the thesis work presented by Ottosson. It showed similar results as [23] and proved it to be a stable method of dealing with low density ratio issues.

5

Computational set-up

In this chapter the computational set-up for the simulations in both MATLAB and IBOFlow is presented.

5.1   Material model evaluation

In this section the methodology used to the evaluate two different material models is presented with the numerical approach as described in section 3.2.2.

The computational framework for evaluating the material models was written in MATLAB. The implemented code uses the same numerical method for the material models as the IBOFlow software. A Newton-raphson algorithm with load control was used to solve the non-linear system. This means that the applied force is incrementally increased for each load step. Equilibrium is found using an iterative method in each load step.

A two dimensional computational domain was used with a square representing the cubical particles used in the experiment. The assumption of plane strain was used in the computations. Two meshes were tested in order to determine an solution independent of the mesh. A coarse and a fine mesh with 324 and 1248 number of nodes respectively were selected. The meshes are shown in figure 5.1. Each mesh were created using *PDEtool* in MATLAB.
The load was applied as compression at the top boundary of the square with the bottom boundary being fixed in both x and y direction. The initial length of the square was 10 mm with a depth of 10 mm. The residual tolerance was set to $1 \cdot 10^{-4}$ and number of load increments to 400 for all cases. The input parameters for each case test was the Young's modulus and maximum applied stress and are shown in table 5.1. The parameter values were taken from experiments performed by Roland and Tuck Hutasingh [26].

Material	Potato	Carrot	Mango
Young's modulus (MPa)	0.194	0.143	0.0123
Maximum applied stress (kPa)	60	49	5

Table 5.1: Input parameters from experiments for evaluation of material model.

The Poisson's ratio was set to 0.49 for all different materials. The strain on the

22

(a) Coarse mesh

(b) Fine mesh
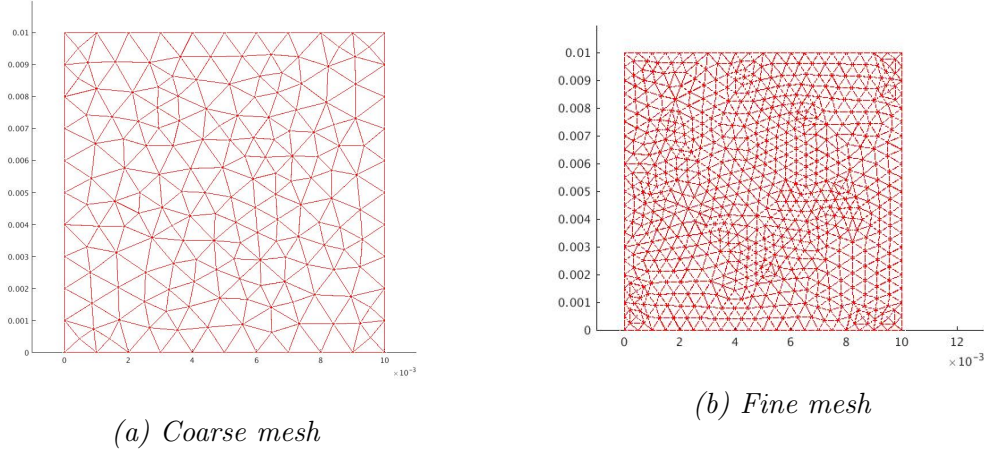
Figure 5.1: *Computational mesh in MATLAB used in the material model evaluation.*

system used in as comparison to experimental data was an average vertical strain on the top of the particle square as

$$\varepsilon_{y,avg} = \frac{\sum_{i=1}^{n_{nodes,top}} \varepsilon_{y,i}}{n_{nodes,top}} \quad , \tag{5.1}$$

where $\varepsilon_{y,avg}$ is the average vertical strain, $\varepsilon_{y,i}$ is the vertical strain of node i on the top boundary and $n_{nodes,top}$ is the number of nodes on the top boundary. The vertical strain was calculated as

$$\varepsilon_{y,i} = \frac{y_i - y_{0,i}}{y_{0,i}} = \frac{\Delta y_i}{y_{0,i}} \quad , \tag{5.2}$$

where y_i is the current location of node i in vertical direction and $y_{0,i}$ is the initial location of node i in vertical direction.

5.2 Mesh dependency study

In this section the methodology of the mesh dependence study is presented. The simulations were performed using IBOFlow described in section 4.1. Extensive studies on the mesh with respect to the fluid using IBOFlow has already been made and proven to produce accurate results as presented in section 4.2. Therefore the focus of the mesh dependence study has been on evaluating solid contact. Two different types of contact are present in the system, particle-particle contact and particle-wall contact. A table of the parameters that were constant in all cases can be seen in table 5.2. The term "Solid steps per fluid step" refers to the number of time steps the solid solver takes per fluid time step.

23

Constant parameters

Fluid viscosity	80 mPas	Contact stiffness	$1 \cdot 10^9$
Fluid density	1032 kg/m^3	Friction coefficient	0.5
Particle density	1300 kg/m^3	Young's modulus	1 GPa
Newmark γ	0.3025	Poisson's ratio	0.49
Newmark β	0.6	Solid steps per fluid step	5

Table 5.2: *Table of constant parameters used in the mesh dependence study.*

The density was selected with regards to the work done by Wang and Brennan [5]. They found that the density of the potato varied from 1380 kg/m^3 to 1080 kg/m^3 depending on the moisture content. The density was then selected to be 1300 kg/m^3 as the moisture content in the submerged potatoes was assumed to be high.

The fluid mesh used in the mesh dependence study was anisotropic, i.e the cell side lengths are not equal. In table 5.3 the smallest cell size is presented with respect to number of refinements that were used in the different cases.

Refinement	Cell size vs particle length	Cell size Δx	Cell size Δy	Cell size Δz
0	1/8L	2.35 mm	1.25 mm	1.25 mm
1	1/16L	1.175 mm	0.625 mm	0.625 mm
2	1/32L	0.5875 mm	0.3125 mm	0.3125 mm
3	1/64L	0.29375 mm	0.15625 mm	0.15625 mm

Table 5.3: *Table of smallest cell size in the fluid mesh with respect number of refinements. Where L denotes the side length of the particles and Δx, Δy and Δz denotes the cell length in each respective direction.*

The simulation domain was a circular pipe with an inner diameter of 0.1 m and a length of 0.3 m. A cyclic boundary condition for both the fluid and particles was set at both ends of the pipe with ambient pressure. Each particle had a total number of 215 nodes.

For each case the CFL number was calculated as

$$\text{CFL} = \frac{U \Delta t}{\Delta x} \quad , \tag{5.3}$$

where U is the velocity, Δt is the time step and Δx is the cell size. In order to evaluate how the stresses relate to the kinetic energy in the system the stored strain energy density from deformation is calculated as

$$\varrho_e = \int \sigma(\varepsilon) d\varepsilon \approx \int E \varepsilon d\varepsilon = \frac{1}{2} \sigma \varepsilon \quad , \tag{5.4}$$

with the approximation that the stress in linearly dependent on the strain. This gives the energy density per unit volume. Multiplied with the volume of the particle gives the total energy stored. This was related to the kinetic energy of the system one time step prior to initial contact.

$$\%_{\Delta E} = \frac{\varrho_e \cdot V - mv^2/2 \cdot e}{mv^2/2 \cdot e} = \frac{2\varrho_e}{\rho v^2 e} - 1 \tag{5.5}$$

This assumes that all of the kinetic energy is converted into strain energy during contact i.e deformation, which is a rough approximation and not fully correct. e is the coefficient of restitution and was approximated using the kinetic energy of the system as

$$e = \sqrt{\frac{E_{\text{kin,before contact}}}{E_{\text{kin,after contact}}}} \tag{5.6}$$

5.2.1 Particle Particle Contact

The set-up of particle-particle contact mesh dependence study consisted of two particles with a distance of 25 mm from each other, as depicted in figure 5.2. One particle (right) was placed at rest with zero initial velocity and the other particle (left) was set with an initial velocity of 2 m/s and rotated such that the tip of an edge was directed at the particle at rest. The surrounding fluid was initiated at rest.
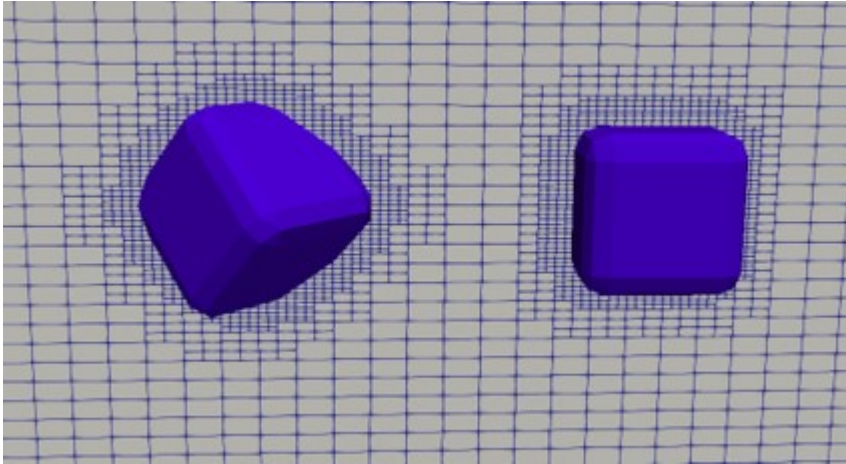
Figure 5.2: Image of the initial set-up with two refinements around each particle.

The parameters that was altered during can be seen in table 5.4, where refinement refers to the refinement around each particle.

Parameters	Values			
Fluid time step (ms)	0.03125	0.0625	0.125	0.250
Solid time step (ms)	0.00625	0.0125	0.025	0.05
Refinement	0	1	2	3

Table 5.4: Table of altered parameters used in the mesh dependence study.

5.2.2 Particle Wall Contact

A particle was placed a distance of 35 mm from the pipe wall with an initial velocity of 2 m/s downward towards the wall and 0.5 m/s tangent to the pipe wall. The particle, when placed, was rotated such that an edge pointed downward towards the pipe wall. The particle had one refinement around the body, depicted in figure 5.3. The number of wall refinements and time step was altered and their values can be seen in table 5.5.
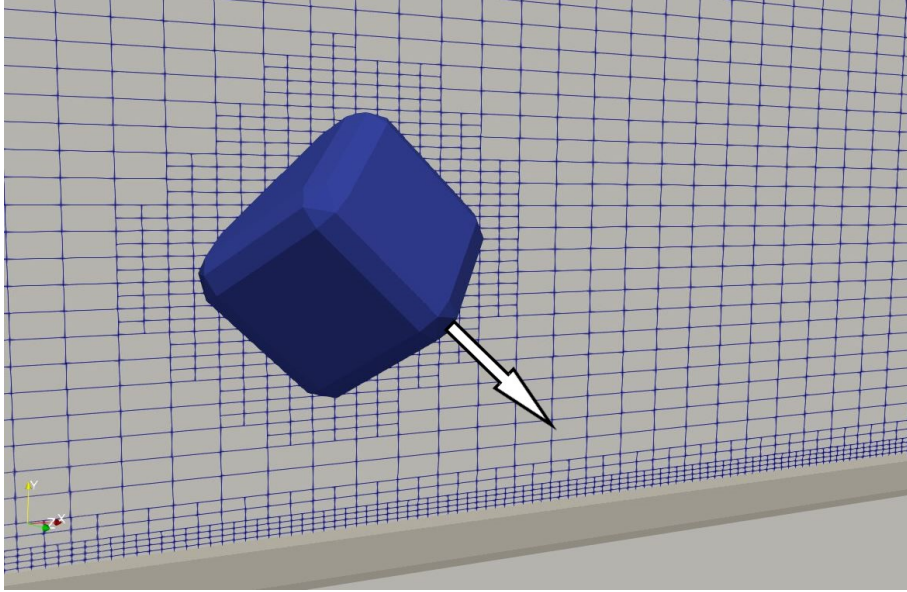
Figure 5.3: Image of initial set-up with one refinement around the particle and two refinements around the wall.

Parameters	Values		
Fluid time step (ms)	0.0625	0.125	0.250
Solid time step (ms)	0.0125	0.025	0.05
Wall refinement	0	1	2

Table 5.5: Table of altered parameters used in the mesh dependence study.

5.3 Parameter study

In this section the two parameter studies will be presented. The parameters were identified and chosen with the assumption or conclusion that they were of importance for the simulation, either for stability or accuracy.

5.3.1 Study of Rayleigh damping

It was discovered that the numerical stability of the system was dependent on amount of damping in (3.23) and required further investigation and evaluation. The same set-up as in the particle-particle contact in section 5.2.1 was used with a time step of 0.125 ms and two refinements around the particles. The methodology consisted of starting with a high value for Rayleigh β and a low Young's modulus. The β is decreased until an unstable system occurred with the same Young's modulus. The Young's modulus was then increased until a stable system was found. Then β was lowered and the procedure was repeated until the particle display a subjectively satisfactory magnitude of rotation due to the contact. The Rayleigh α was set to zero during the entire study as the hypothesis was that the instability came from the high frequencies. The starting values were $1 \cdot 10^{-2}$ and 0.2 MPa for the Rayleigh β and Young's modulus respectively.

5.3.2 Investigation of contact stiffness

As the value of the contact stiffness determines the stiffness of the contact this was evaluated in order to obtain a satisfactory contact. The same set-up as in the particle-particle contact study in section 5.2.1 was used. One refinement around the particle was used with a time step of 0.125 ms. The value of the contact stiffness was varied from $1 \cdot 10^7$ to $1 \cdot 10^9$.

5.4 Investigation of pipe restriction

Two different pipe geometries were chosen to use in the simulations regarding the ratio between the smallest pipe diameter and particle size. Both geometries has the same inner diameter of 48.5 mm before the contraction and after the expansion. The small pipe diameter between the contraction and expansion was 16 mm and 26 mm for the two cases. A visual representation of the pipes with displayed dimensions are depicted figure 5.6.

Two sizes of particles were used in the simulations, 10 mm and 17 mm in side length. These were determined average size of the samples used in the experiments. A visual representation of the particles with displayed mesh can be seen in figure 5.4. The particles were symmetric, i.e all sides had the same length. The 10 mm particle was simulated in both single and high concentration in both pipe domains. The 17 mm particle was only simulated with a single particle in the 26 mm pipe. Each case that was set-up and simulated was done to resemble the experiments by Roland and Tuck Hutasingh [26] as much as possible.
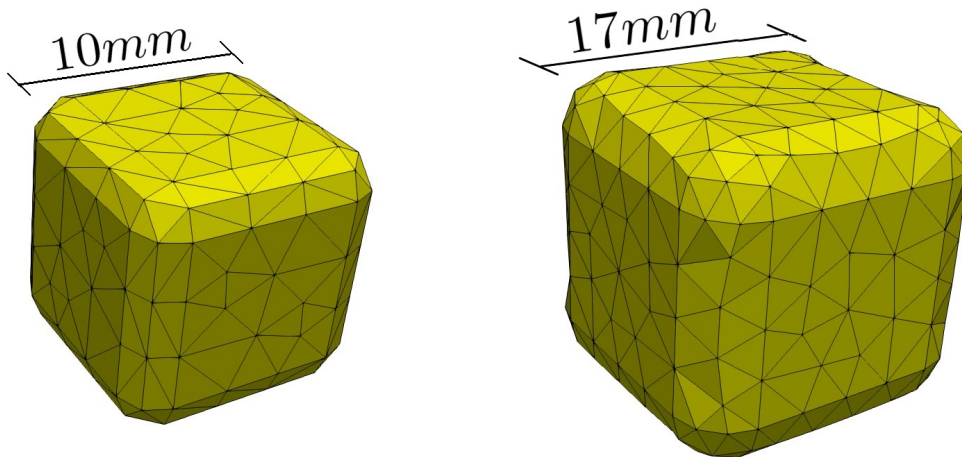
(a) Particle with a side length of 10 mm   (b) Particle with a side length of 17 mm

Figure 5.4: Image of the cubic particles used in the simulation with displayed mesh. The particles are symmetric with the same side length on all sides.

The system is initiated from rest with particles placed from the inlet and forward in a systematic arrangement. An illustration can be seen in figure 5.5. The fluid and solids are treated with two separate boundary conditions. The fluid is set to

have an inlet volume flow rate of 3 m^3/h with a parabolic velocity profile. The fluid is accelerated from rest up to the specified flow rate over 25 time steps, in order to avoid any numerical oscillations during start-up. The outlet is set as a fluid pressure outlet with an initial pressure of 10 kPa. The inlet and outlet for the fluid are not connected in a non-cyclic manner. The particles are treated at the inlet and outlet using a cyclic boundary conditions. Meaning that as a particle exits the outlet it enters the inlet.
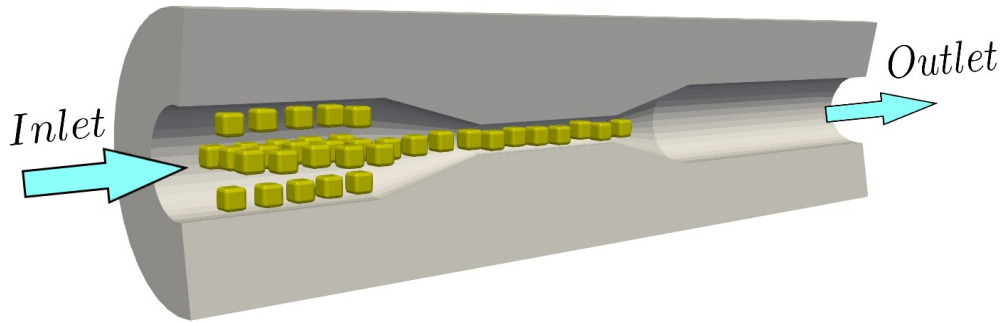
Figure 5.5: Visual representation of the initiation state of the simulation with the arrangement of particles using a high concentration.

In table 5.2 the constant parameters for all cases can be seen. Only the Young's modulus was changed depending on case due to stability issues.

Section	**Parameter**	**Value**
Solid	Young's modulus	0.1-1 GPa
	Poisson's ratio	0.49
	Friction coefficient	0.5
	Density	1300 kg/m^3
Fluid	Density	1032 kg/m^3
	Volume flow	3 m^3/h
Rayleigh damping	α	0 rad/s
	β	$1 \cdot 10^{-9} \frac{1}{rad/s}$
Newmark algorithm	γ	0.6
	β	0.3025
	Residual tolerance	$1 \cdot 10^{-4}$
Simulation	Cell size (zero refinement) $\Delta x \times \Delta y \times \Delta z$	2.35 x 1.25 x 1.25 mm
	Contact Stiffness	$5 \cdot 10^7$ N/m

Table 5.6: Table of constant parameters used in the simulation cases.

For cases with a single particle two different fluid viscosities were used, 265 mPas and

1695 mPas at a shear rate of 100 s^{-1}, denoted as low and high viscosity respectively. The parameters used in the power law (3.4) are shown in table 5.7.

	Viscosity at 100 s^{-1} shear rate	n	K
Low viscosity	265 mPas	0.408	4.05
High viscosity	1695 mPas	0.263	50.4

Table 5.7: *Values of the parameters used to model the viscosity of the fluid medium using power law.*

In order to approximate a fully developed flow before the contraction in the pipe a parabolic velocity function was applied on the inlet as

$$\begin{cases} U(r) = (ar^2 + br + c) \cdot U_{max} \\ \quad a = \dfrac{-1}{R^2} \\ \quad b = 0 \\ \quad c = 1 \quad , \end{cases} \tag{5.7}$$

where U is the velocity at a point with the distance r from the center of the pipe and R is the inner radius of the pipe at the inlet. U_{max} is the maximum velocity of the flow profile, calculated from the mass flow with (5.7) as

$$\begin{aligned} \dot{m} &= \int_0^R 2\pi r U(r) dr \iff \\ U_{max} &= \frac{2\dot{m}}{\pi R^2} \end{aligned} \tag{5.8}$$

To obtain a more complete understanding of how the system affects the particles, two types of cases were set-up for both the 16 mm and the 26 mm pipe. The flow flows from left to right and the pipe length after the expansion was longer in order to allow the flow the reattach to the wall.

The two cases consists of a single particle and a high concentration of particles. The high concentration of particles was set to 5% of the fluid volume inside the pipe. Depending on the pipe diameter, the number of particles varies as the volume was different. For the 16 mm pipe 36 particles was used and for the 26 mm pipe 37 particles was used.
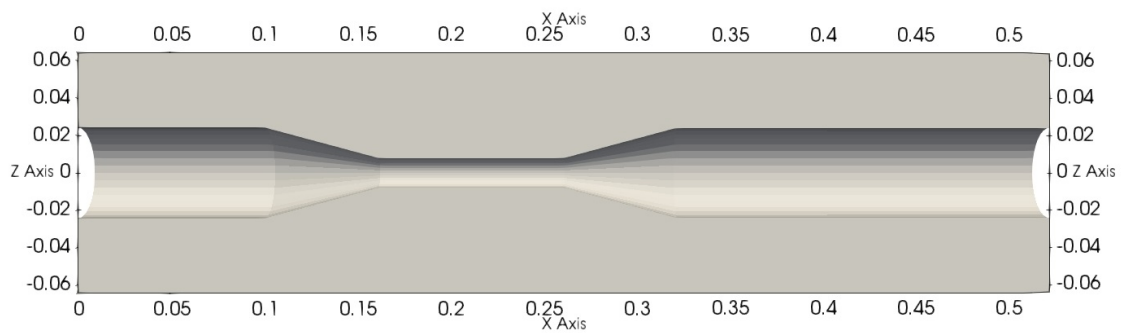
(a) 16 mm.
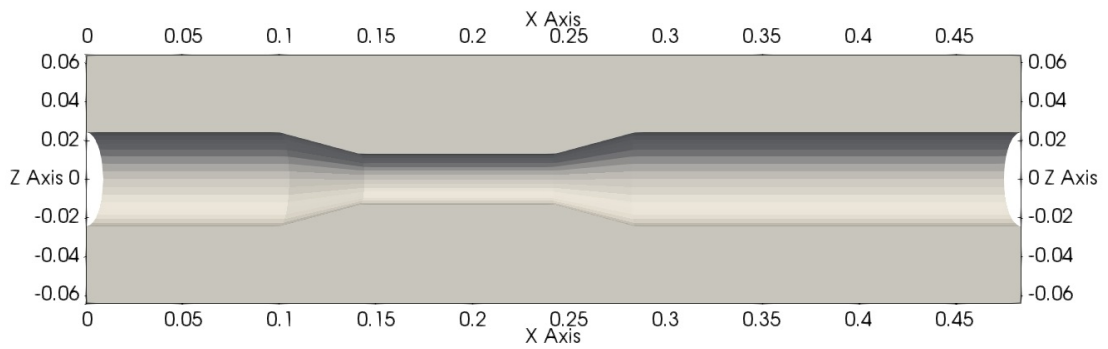
(b) 26 mm.

Figure 5.6: Visual representation of the two pipes used in the simulations sliced through the y-plane. The dimensions of each pipe are displayed in meters.

6

Results and discussion

6.1 Material model evaluation

In this section the results from the material model evaluation described in section 5.1 is be presented. The experimental data used to compare the material models with was gathered by the parallel master thesis work by Roland and Tuck Hutasingh [26].

The Young's modulus used for each simulation was taken from experiments at a point where the experimental sample had a certain strain percentage. Each strain percentage and point chosen is indicated by a black circle for each material sample in figures 6.2, 6.3 and 6.4 with legend displaying the strain percentage.

6.1.1 Mesh dependence

As can be seen in figure 6.1 both material models gave nearly the exact same strain response for the coarse and fine mesh when exposed to equal applied pressure. Therefore the solution is independent of the cell size of the mesh.

(a) St. Venant Kirchhoff   *(b) Neo-Hookean*
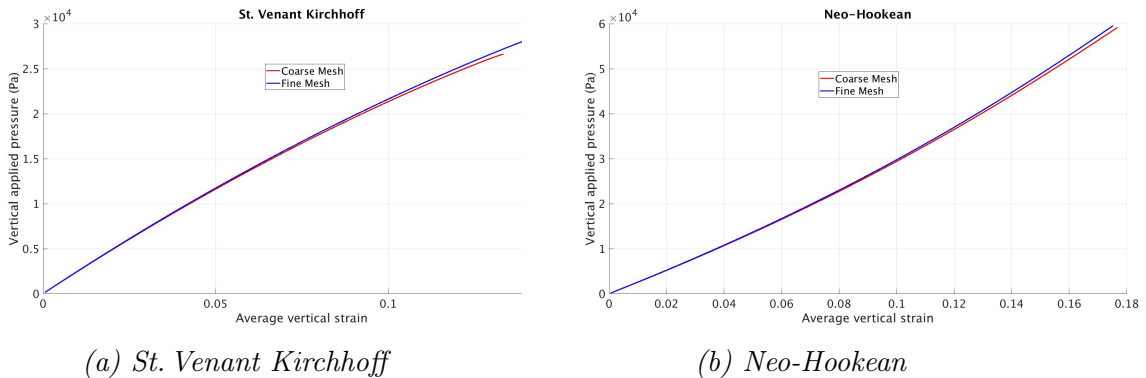
Figure 6.1: Vertical applied pressure vs vertical average strain for each material model using coarse (red) and fine mesh (blue).

In the continued evaluation of the material models for each material product the coarse mesh was used, due to the decreased computational time and therefore faster iteration cycles.

6.1.2 Potato

The St. Venant Kirchhoff simulation diverged after 181 load steps which equals to 27.15 kPa in applied load. The Neo-Hookean converged through the entire simulation.

Figure 6.2: Vertical applied pressure vs average vertical strain for both material models and experimental data with mean and standard deviation for potato. Experimental measurement (green), St. Venant Kirchhoff (red) and Neo-Hookean (blue)

As can be seen in figure 6.2 neither material model seems to accurately approximate the experimental data for larger strains. For strains up towards 0.04 both material models predict the same response but deviates from each other for strains above 0.04. For small strains the best choice of material model is not explicit. For larger strains the Neo-Hookean model has a higher degree of agreement with experimental data, but still contains large errors. The experimental data does however have large standard deviations and both material models lay within the range. With this in regard, the Neo-Hookean material model still seem to follow the overall behaviour more closely.

The large differences from the material models compared with the experimental data might be due to the model not considering plastic deformation. Even though the Neo-Hookean, according to literature, is often used for rubber-like materials it might not be sufficient for predicting deformation of potato material. There exists a high uncertainty of the micro-structural and mechanical behaviour inside the potato, which in turn leads to a poor understanding of what are the critical fracture mechanics and why they occur. The experimental data indicates that the sample hardens during deformation, which might be caused by compression of the potato and increasing the density.

Neither material model seemed to have a good correlation with experiments. The large standard deviation in the experimental results makes it more difficult to draw any definitive conclusion. However the Neo-Hookean material model seem does seem to agree more with the overall behaviour during deformation, but the actual value is incorrect.

6.1.3   Carrot

The St. Venant Kirchhoff simulation diverged after 184 load steps which equals to 22.54 kPa in applied load. The Neo-Hookean converged through the entire simulation.
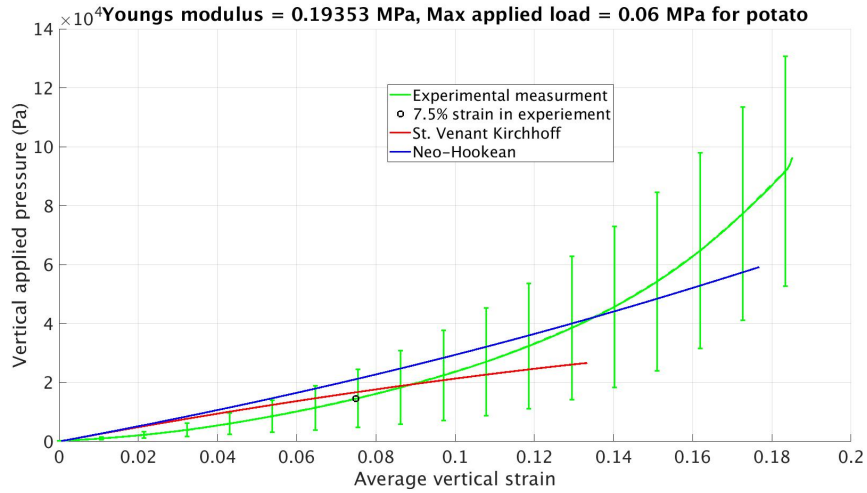

Figure 6.3: Vertical applied pressure vs average vertical strain for both material models and experimental data with mean and standard deviation for carrot. Experimental measurement (green), St. Venant Kirchhoff (red) and Neo-Hookean (blue)

As can be seen in figure 6.3 the Neo-Hookean material model has good agreement with experimental data with minor deviations in general. The largest relative difference between simulation and experiment can be found at low strains. The St. Venant Kirchhoff material model has the same level of agreement for strains approximately 0.035 and below, but deviates from the experimental data for larger strains. The standard deviation of the experimental data is relatively low. Overall it seems to indicate that the Neo-Hookean material model is a good approximation of carrot materials for strains up towards 0.2.

6.1.4   Mango

The St. Venant Kirchhoff simulation diverged after 155 load steps which equals to 1.94 kPa in applied load. The Neo-Hookean converged through the entire simulation.

By observing figure 6.4 it can be seen that neither material model has good agreement for the entire strain range. The curvature at the end of the Neo-Hookean model is due to the collapse of individual elements which significantly weakens the whole structure. At high strains, about 0.2 and above, the range of validity for the material models can be put into question and could perhaps be linked to the quality of the mesh. Both material models predicts similar behaviour up towards strains of about 0.04 and then deviate from each other. The St. Venant Kirchhoff material model has better agreement for strains approximately 0.13 and below, but still with significant errors compared with experimental data. How ever the experimental data has large standard deviations and does need to be considered. For strains above 0.13 the St. Venant Kirchhoff seems to flatten out and the error increases, where as the

Neo-Hookean has better agreement, also still with large errors but within the area of standard deviation.

Similar to the potato, the large errors between the simulation and experimental data might be due to not considering plastic deformation. There also exists a high uncertainty of the micro-structural and mechanical behaviour inside the mango. This means that there is a poor understanding of the fracture mechanics, how it occurs and why. The standard deviation in the experiments are also quite large, but the Neo-Hookean seem to be a more accurate model for predicting the strain response in mango.
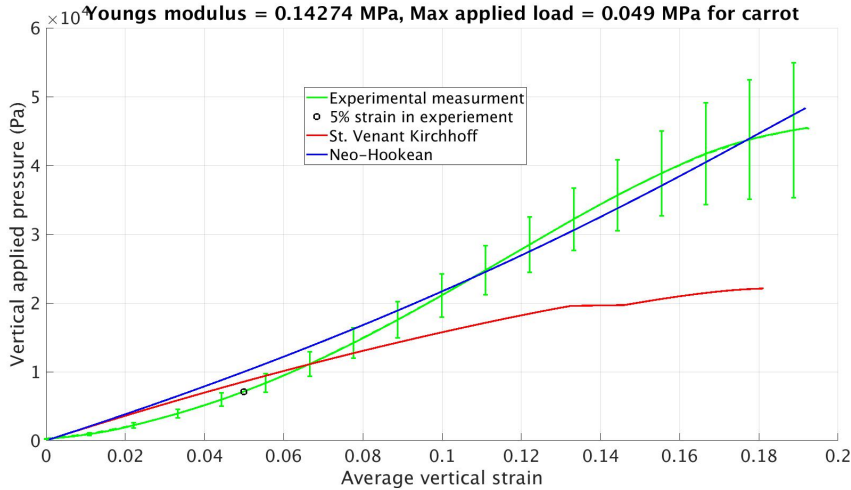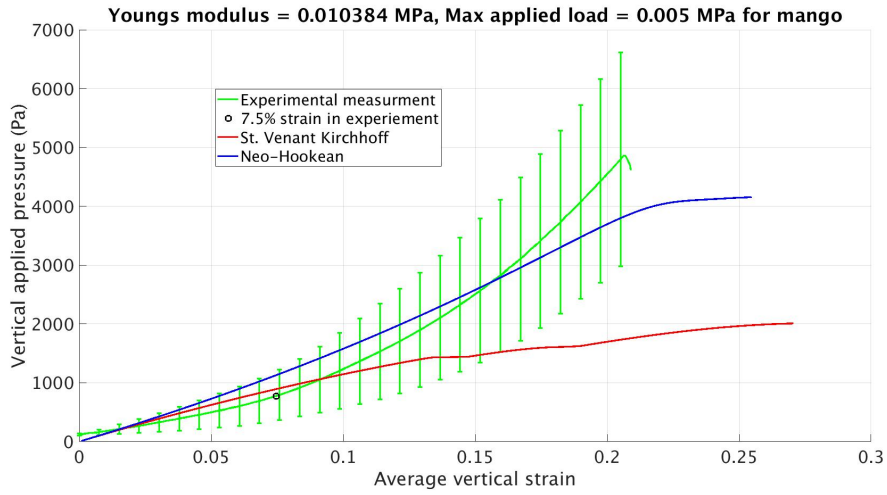

Figure 6.4: *Vertical applied pressure vs average vertical strain for both material models and experimental data with mean and standard deviation for mango. Experimental measurement (green), St. Venant Kirchhoff (red) and Neo-Hookean (blue)*

6.2 Parameter study

6.2.1 Study of Rayleigh damping

In this section the study of the effects of change in parameter value of the Rayleigh damping is presented as described in section 5.3. The results are interpreted in terms of numerical stability and the physical behaviour of the particles.

The *stable* and *unstable* mentioned in figure 6.5 refers to if the solver converged or diverged during simulation. The circles denote the value of the parameters used. In the same figure three areas are highlighted, *no rotation*, *minimal rotation*, and *good rotation* enclosed by the black lines. Minimal rotation refers to the phenomena that the particle rotated during contact but ceased to rotate immediately or shortly after contact between the particles ended. The area denoted as *good rotation* is the area were the particles continued to rotate sufficiently long after contact. The observations of rotation were made using a continuous rendered animation in the post-processing software Paraview.
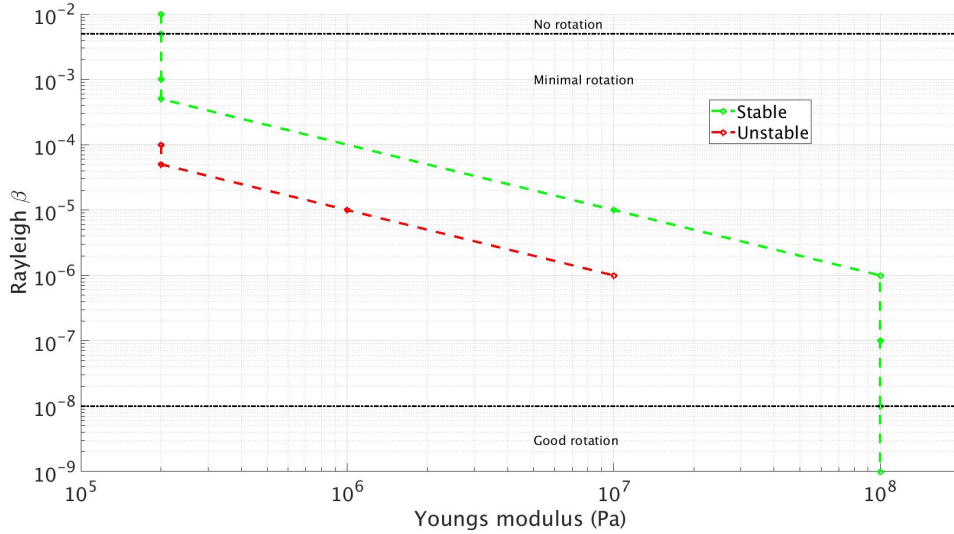
Figure 6.5: Visual representation of stable and unstable simulations for different Rayleigh β and Young's modulus.

From the same figure it can be seen that there exists a trend for the area in which stability is achieved. If the Rayleigh β and Young's modulus are chosen such that it lies above and/or to the right of the green line the system is stable. In order to obtain a system where the particle has a rotation that is not inhibited or damped to an extent that is presumed nonphysical, the value of β should be below 10^{-8}. In the performed simulations β 10^{-9} was selected in order to be certain that the rotation of the particles was not damped by the numerical scheme.

Due to the selection of β equal to 10^{-9} a higher Young's modulus than initially expected had to be used to achieve stability. The smallest value for the Young's modulus to achieve stability, as seen in figure 6.5, is significantly higher than the measured Young's modulus of the samples from the experiments. The consequence of this is that the deformation of the particles and large strains is not accurately predicted. As the strains will be low the difference in strain response with respect to stress for the different material models is negligible. The St. Venant Kirchhoff material model was therefore selected due to its stability and less computational cost compared with the Neo-Hookean.

The reason for instability is still uncertain. One possibility is a build up of energy in the system, a similar problem that might occur in the Newmark scheme. Another possibility might be due to the eigenfrequency of the particle. The reasoning behind this hypothesis is that the oscillation of the propagation waves in the particle are amplified if they are close to the eigenfrequency. In order to confirm this it requires further and more extensive investigation of purely the implications of the Rayleigh damping and the mathematical framework of both the FSI and FEM solver.

6.2.2   Investigation of contact stiffness

In this section the influence of the contact stiffness with respect to the stress due to collision and physical behaviour of the particles was studied as described in section 5.3.2.

By lowering the contact stiffness the impact between the particles became softer. This can be seen in figure 6.6 as the maximum stress in the particles decreased with decreasing contact stiffness. It can also be seen in figure 6.7 as the momentum of the stationary particle after contact decreases slightly with decreasing contact stiffness. The momentum of the moving particle seems to be the approximately the same for contact stiffness $5 \cdot 10^7$ N/m and above. As the contact stiffness was lowered to $25 \cdot 10^6$ N/m and below the contact displayed an oscillatory behaviour. When reviewing this behaviour as an animation in Paraview, it was reasoned to be unphysical and incorrect. This was based to a majority on observational intuition and subjective reasoning.
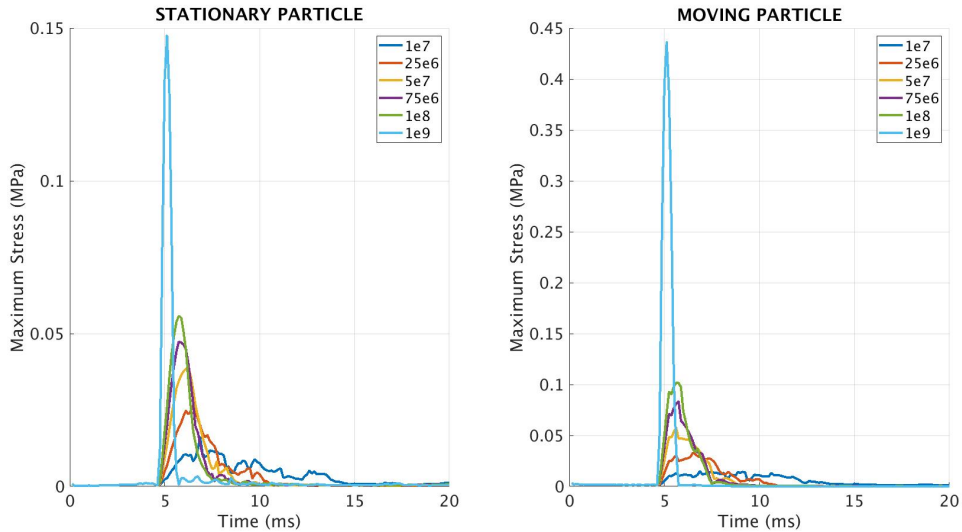
Figure 6.6: Maximum stress of stationary and moving particle for different values of contact stiffness.

The peak maximum stress, as seen in figure 6.9, increases significantly as the contact stiffness is increased above 10^8 N/m. This is due to the fact that approximately the same amount of momentum is transferred from the moving particle to the stationary particle but during a a shorter time period. This can be seen in figure 6.7 as shortly after contact the moving particle has nearly the same momentum and the stationary particle has a moderate difference in momentum with respect to contact stiffness of $5 \cdot 10^7$ N/m and above. The difference in contact time can be seen in figure 6.8 as the maximum penalty visualizes, when above zero, when the particles are in contact with respect to time. If the contact time is lower but the energy of the system is the same, it results to a higher peak maximum stress as observed. The maximum penalty is a relative measure of the overlap between the particles during contact.

In figure 6.10 a visual representation of the contact between the particles with the
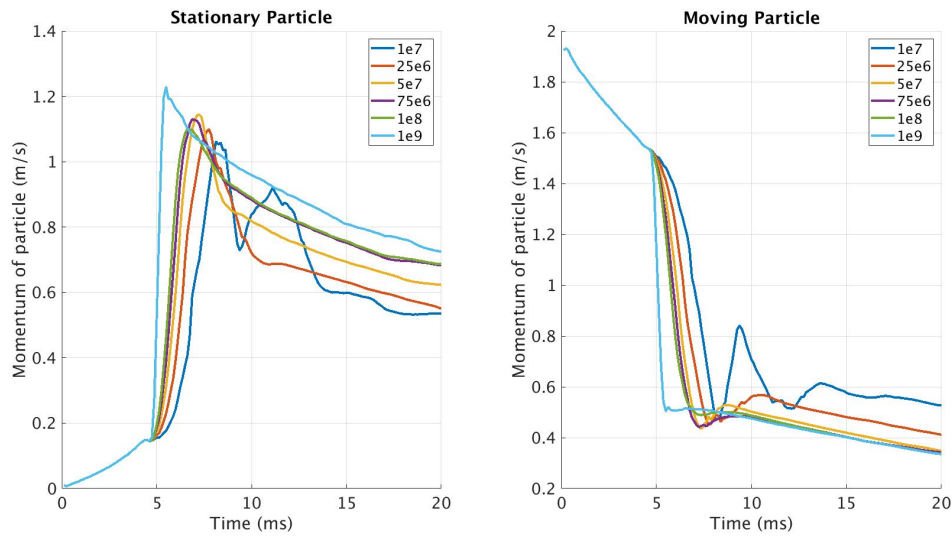
Figure 6.7: Momentum of stationary and moving particle for different values of contact stiffness.
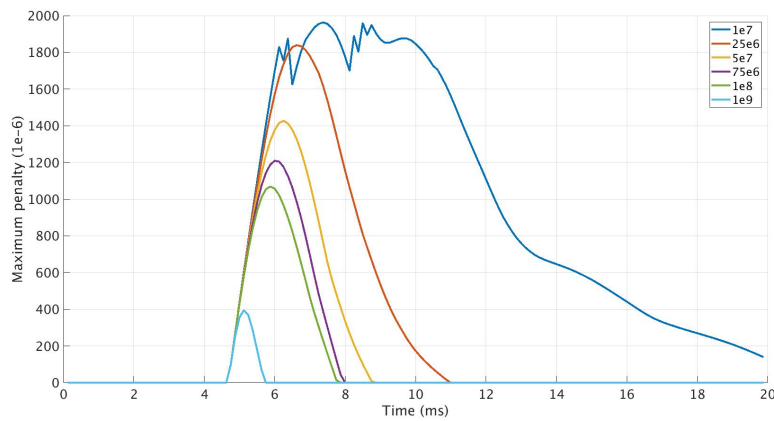

Figure 6.8: Maximum penalty using different values for contact stiffness.
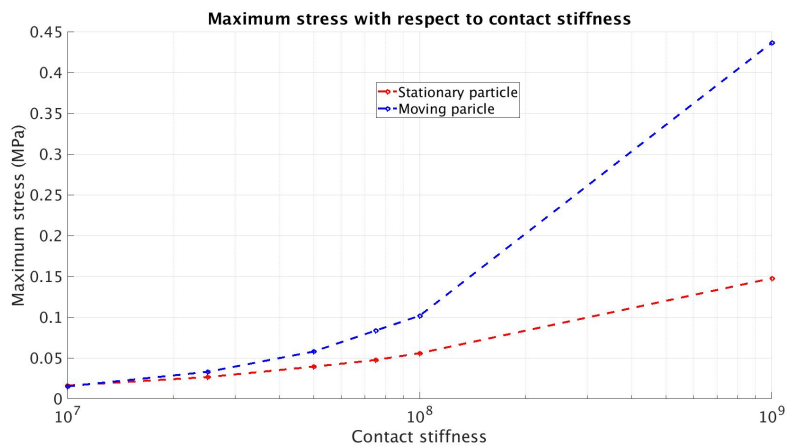

Figure 6.9: Peak maximum stress on the particles with respect to the contact stiffness.

indentation for a contact stiffness of $5 \cdot 10^7$ N/m. It was considered the most accurate prediction of the contact. This was based on visual observation with partial judgment of what is assumed to be a correct physical behaviour made using Paraview together with the changes in maximum stress and momentum. Collision between particle could be seen in the captured high speed videos of the particle flowing through the contraction. Any more accurate comparison then visual analysis between simulation and video could not be made. The overall simulated collision behaviour for the selected contact stiffness did however seem to resemble reality sufficiently. The indentation in the figure is however not ideal, but is a result of the necessity of having a high Young's modulus to achieve computational stability as discussed in section 6.2.1. The contact stiffness might therefore be lower than it would have been if the Young's modulus was the same as in the measured experiments. This lower contact stiffness allows a larger overlap between the solid phases.
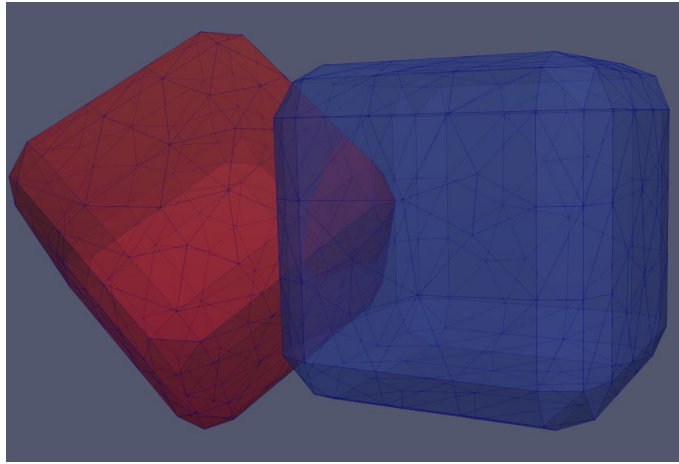
Figure 6.10: Visual representation of particle contact at a contact stiffness of $5 \cdot 10^7$ and the indentation (overlap) of the moving particle (red) in the stationary particle (blue).

6.3   Mesh dependency study

In this section the results from the mesh dependence study as described in section 5.2 will be presented.

For each plot where the CFL number is written beside each data point, it was extracted at system initiation and rounded off to the first decimal point. For the presented results where the CFL number is constant, the fluid time step was decreased relative to the decrease in cell size due to the refinement.

One important aspect that needs to be taken into consideration when reviewing and analyzing the results is the point in time when the quantities are calculated. As the time step is decreased, the time between initial contact and the time at the previous time step decreases. This means that at which point in time the quantities are calculated, one time step before or after contact begins or ends respectively, will be different depending on the time step used. In other terms, as the time step length is decreased, the simulation gets closer to the exact moment in time of initial

contact. This might be a possible source of error or might cause slight differences in result. Another possible source of error might be that data is only extracted from every 10th time step.

6.3.1 Particle particle contact

By observing figure 6.11 it can be seen that there seems to be a collective convergence trend as the mesh is refined both before and after contact. The difference between each data point seems to decrease as the refinement is increased for all values of CFL tested.

By looking at figure 6.11a the CFL number seems to have a significant impact on the deceleration of the moving particle up until initial contact occurs. However at the point of three refinements the moving particle has the same velocity before contact regardless of CFL number. For two refinements the difference is small with a maximum difference in velocity of about 7%. This might be due to how accurately the boundary layer around the particle is resolved. This indicates that with regards to the velocity of the moving particle before initial contact it reaches moderate mesh independence at two refinements and fully mesh independent at three refinements.
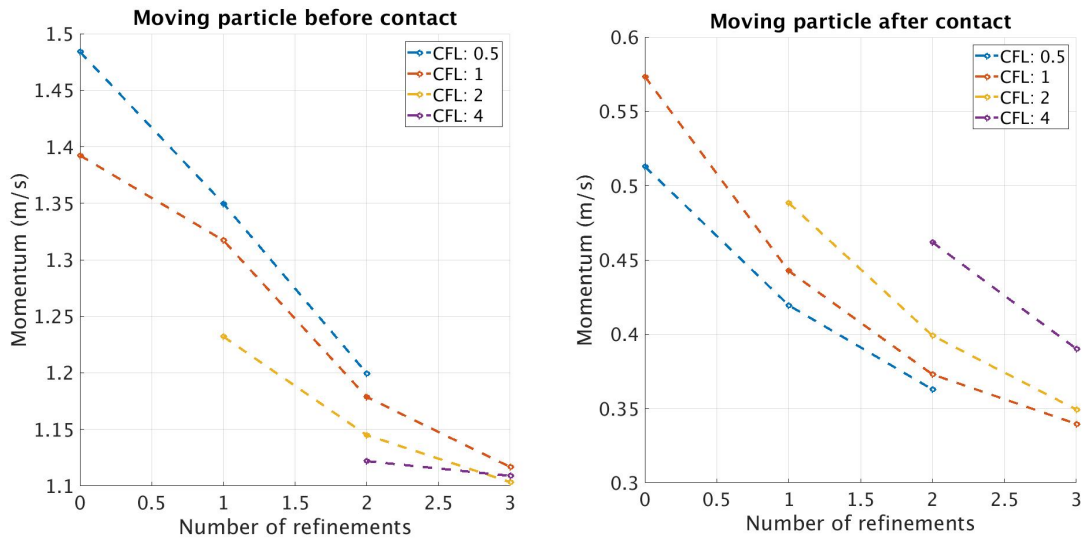
For the moving particle after contact in figure 6.11b, it takes both the aspect of contact and fluid interaction into consideration. In analogy, prior to contact it exhibits a similar trend. At two and three refinements the difference is relatively small, except for a CFL number of four. The difference in velocity between CFL number 0.5 and 2 at two refinements is approximately 11%, which is considered a relatively small difference. Similar to the moving particle before initial contact, after contact it seems to reach a moderate mesh independence at two refinements. When studying figure 6.12a of the moving particle, where the same result is presented but with constant time step length instead of constant CFL. It shows a similar trend of mesh independence at two refinements or higher. It can also be seen that there is a large difference for different time step lengths, but the difference decline as the time step is decreased. This seems to show that the contact is resolved more accurately as the time step length is decreased. The difference between fluid time steps 0.03125 ms and 0.0625 ms, with solid time step 0.00625 ms and 0.0125 ms respectively, for two and three refinements is nearly inconsequential.

In figure 6.11c it is difficult to draw any definitive conclusions as it is highly dependent on the moving particle. It is however possible to see the conservation of momentum by comparing it to figure 6.11b. At the point where the stationary particle has its highest velocity magnitude the moving particle has its lowest magnitude and vice versa. This can be further confirm by observing the loss of momentum in figure 6.13. There it can be seen that the percentage change in momentum of the system before and after contact ranges from a maximum of 2% to a minimum of approximately -3% for different refinements. This is assumed to be close to negligible since the difference might be an affect of the fluid, sampling time, numerical oscillations in the solution or other unknown factors. If refinement two is studied alone the difference is even less. The contact can therefore be considered as momentum conservative for all set-ups.

(a) Moving particle before initial contact.

(b) Moving particle after contact.
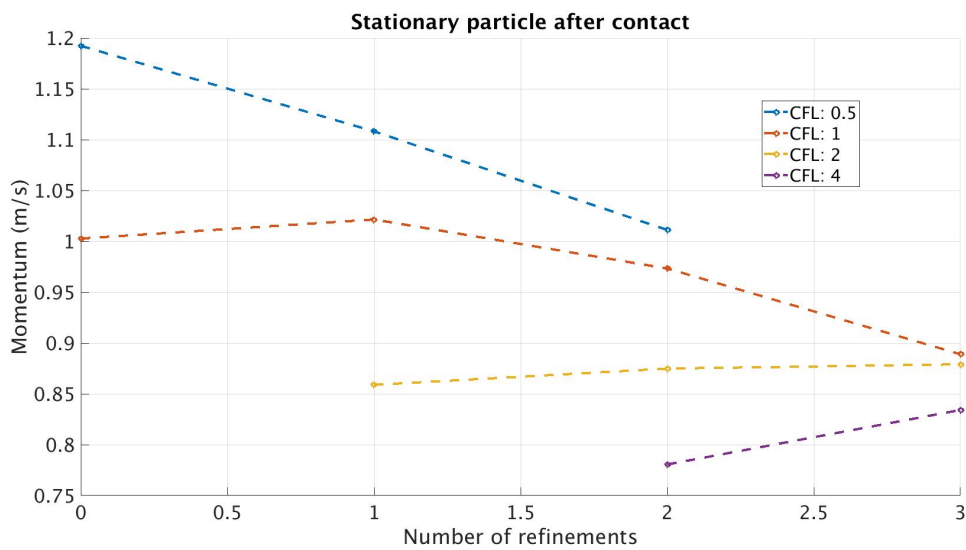
(c) Stationary particle after contact.

Figure 6.11: Momentum of each particle before and after contact with respect to number of refinements. Each curve has the same value of CFL number.
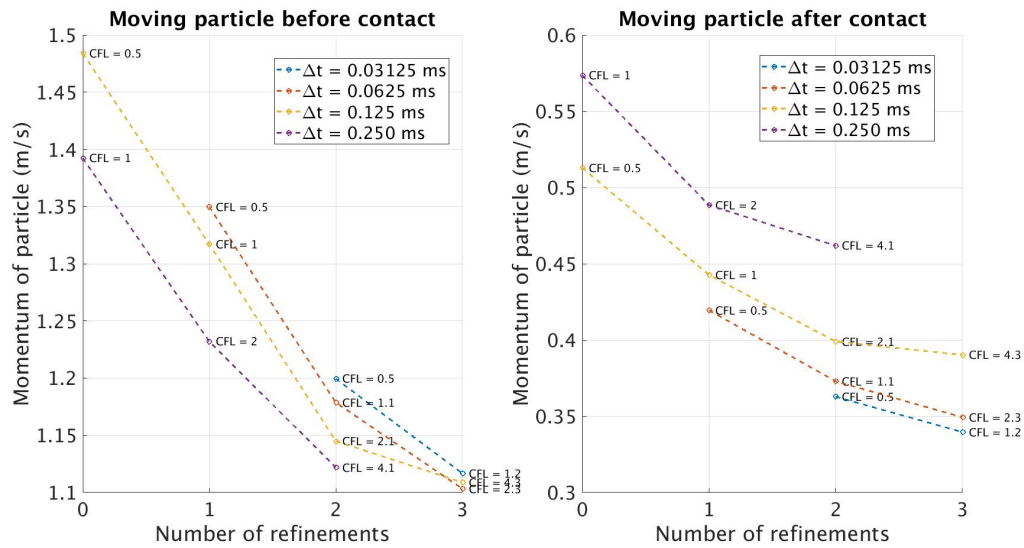
(a) Moving particle.
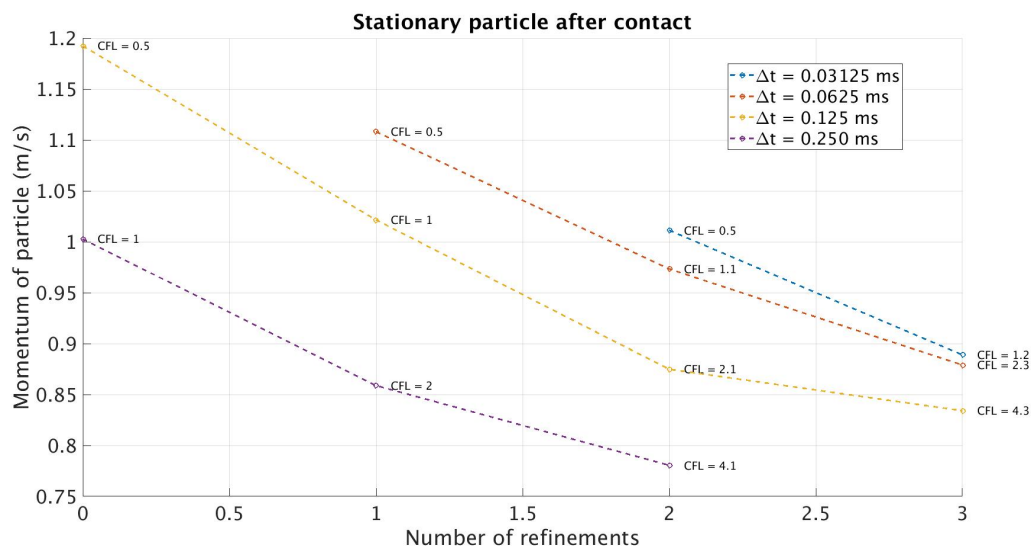
(b) Stationary particle

Figure 6.12: Momentum of each particle before and after contact with respect to number of refinements. Δt is the fluid time step.
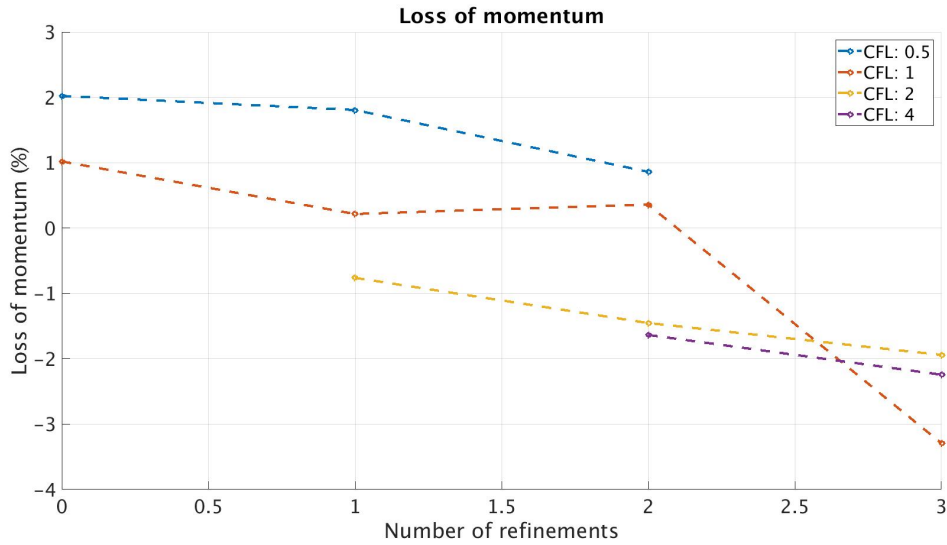
Figure 6.13: Change in particle momentum in the system. The momentum is calculated one time step prior to contact and one time step after contact between the particle has ended.

By viewing figure 6.14 there is a large spread in the magnitude of the maximum stress exerted on each particle for each CFL number. It seems to become moderately mesh independent at two mesh refinements for CFL ≤ 2. The large difference between CFL two and four might be because of the contact not being accurately resolved due to a too large time step. This is indicated in figure 6.16 where the same result is presented but each line has the same time step length. There it is possible to see that time steps 0.125 ms and below for two refinements and higher show similar behaviour with moderate difference in maximum stress magnitude. This implies that the maximum fluid time step in order to obtain an accurate solution of the stress and contact is 0.125 ms with a solid time step of 0.125/5 ms = 0.025 ms. With these time step restrictions the CFL number should also be two or below.
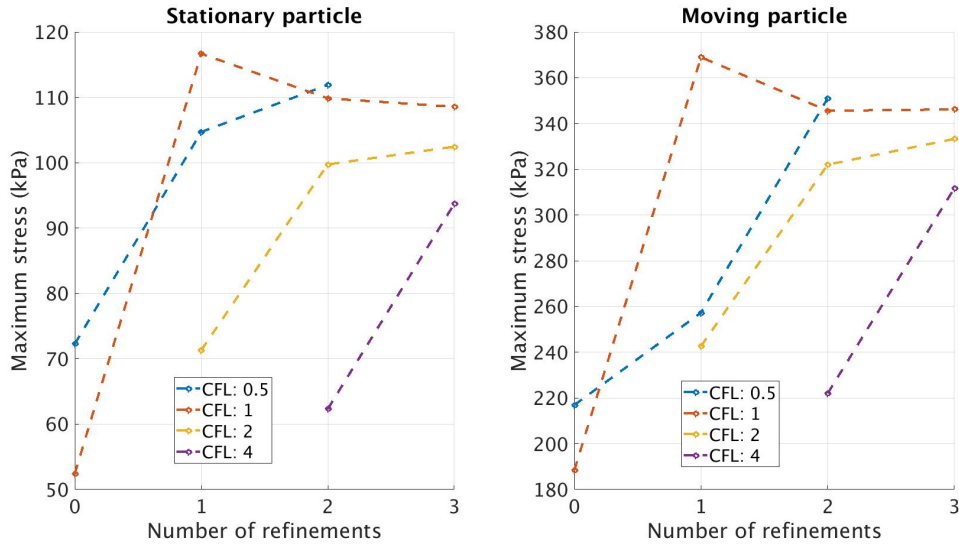
Figure 6.14: Maximum stress for each particle during contact with respect to number of refinements. Each curve has the same value of CFL number.

The percent difference between kinetic energy prior to contact and stored strain energy in the particles is presented in figure 6.15. A similar trend as discussed previously can also be seen here. The plot shows tendencies of stabilizing at two or more refinements. The CFL number has a large affect on the difference in energy. For one or less refinements there is a large difference when exceeding a CFL of one. When increasing the refinement to two, the CFL threshold is increased to two.

Figure 6.15: Percent difference between stored strain energy in the particles with respect to the difference in kinetic energy of the particles before contact using (5.5).

In conclusion the study of mesh dependency for particle-particle contact seem to suggest a threshold for the CFL number of 2. Ideally the simulations should maintain CFL ≤ 1, but can go up towards two and retain accuracy. The time step length had a significant effect on accuracy when resolving the contact between the particles. At the solid time step of 0.00625 ms seemed to be low enough in order to accurately
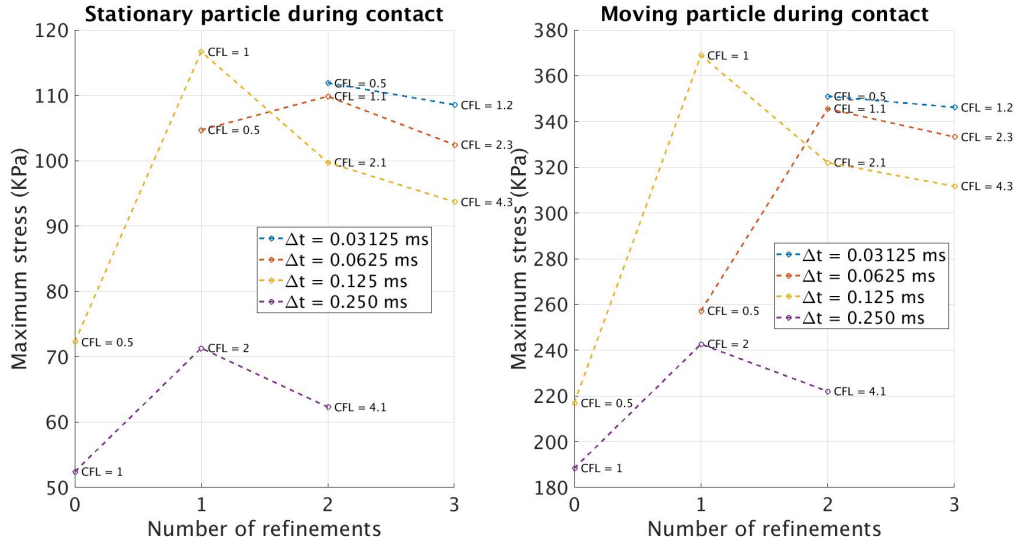
Figure 6.16: Maximum stress of each particle during contact. Δt is the fluid time step.

resolve the contact. The fluid time step should be selected such that the CFL number requirements are satisfied. As for the mesh, a level of refinement of two seems to be sufficient. Three refinements could be argued is less sensitive to the CFL number but does increase the computational cost significantly compared with two refinements as the number of cells increase exponentially.

6.3.2 Particle wall contact

It was discovered that there existed a hierarchy in mesh refinements between the particle and wall within IBOFlow. The mesh refinement around the particle has a higher hierarchy than the wall, meaning that the refinement around the particle overwrites the mesh around the wall. This can be seen in figure 6.17 and due to that the particle refinement was set to one for all cases this has to be taken in to consideration.
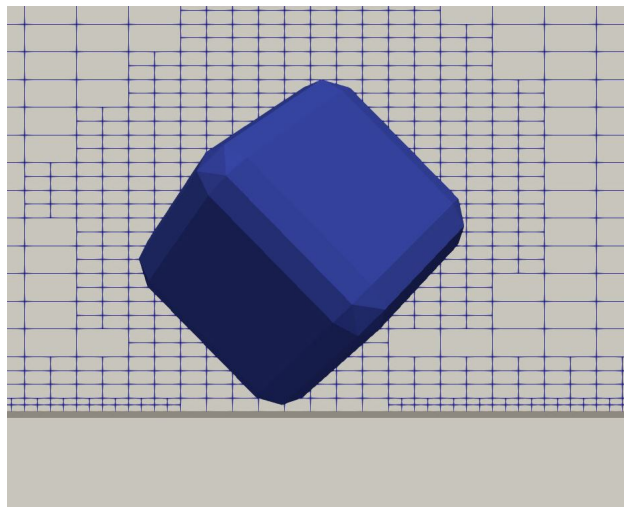
Figure 6.17: Visualization of the particle refinement overwriting the mesh refinement around the pipe wall.

44

As can be seen figures 6.18, 6.19, and 6.20 there is no change between different mesh refinements when using the same time step. There is however a large difference between different time steps. This indicates that the contact is highly dependent on time scale of which it is resolved. As the number of solid time steps per fluid time step was set to 5, the shortest solid time step was 0.0625/5 ms = 0.0125 ms.
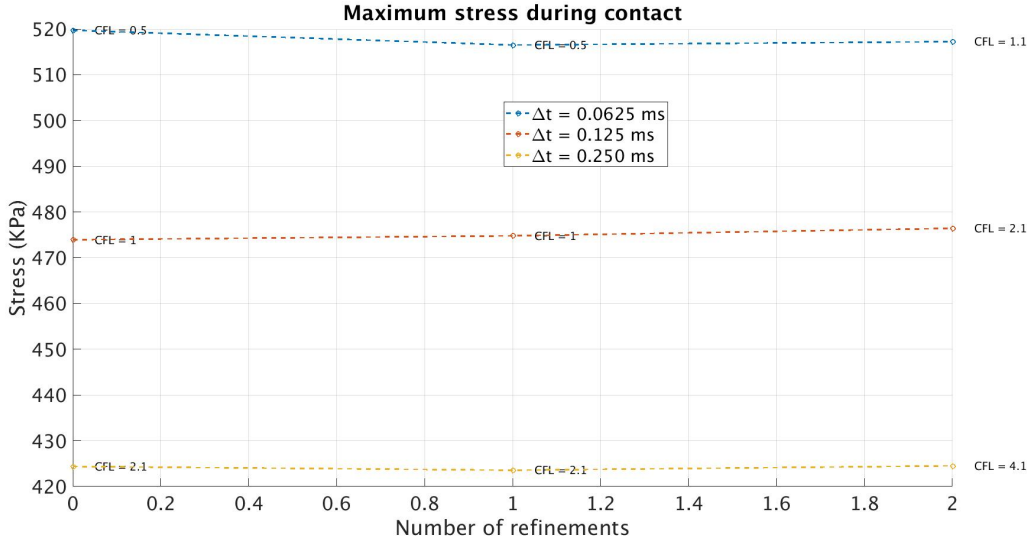
Figure 6.18: Maximum stress of the particle during contact. Δt is the fluid time step.
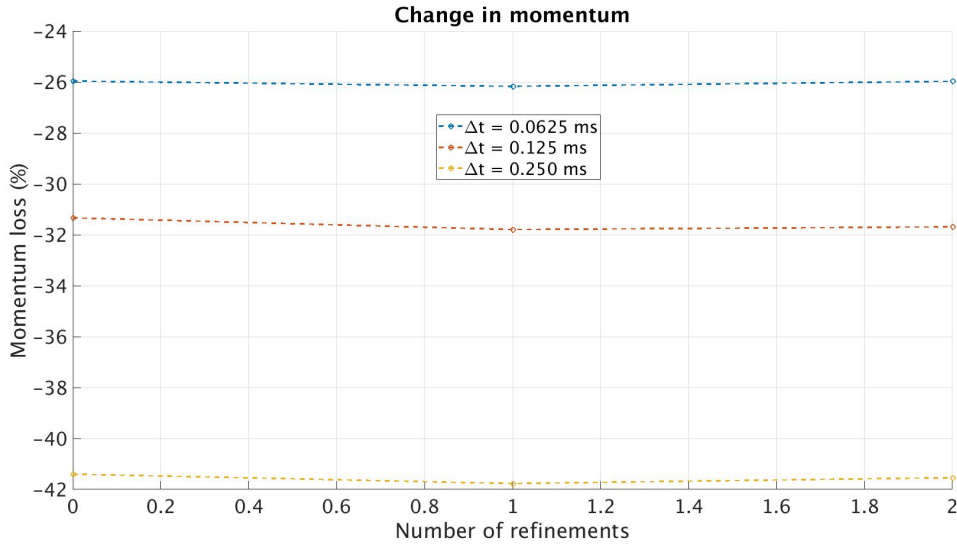
Figure 6.19: Change in momentum of particle with respect to before and after contact. Δt is the fluid time step.

In figure 6.20 it can be seen that for the fluid time step 0.0625 ms the stored strain energy in the particle is higher than the kinetic energy prior to contact. This might be due to the fact that the surrounding fluid was accelerated by the motion of the particle through the medium. During particle-wall contact the fluid in motion pushes on the particle once it has decelerated to a velocity which is lower than the surrounding fluid. This pressure increases the stresses and in turn strain energy in the particle and might be the cause of a positive relative energy percentage.

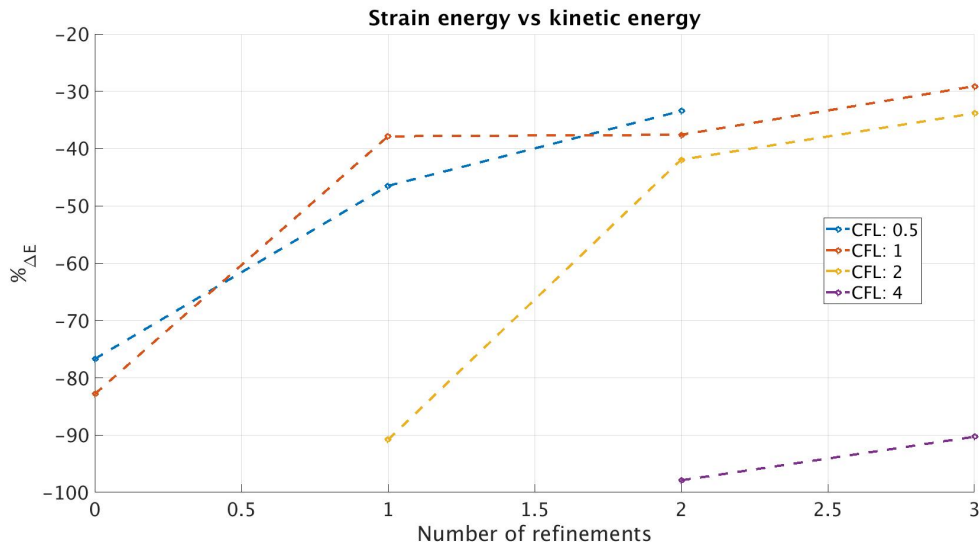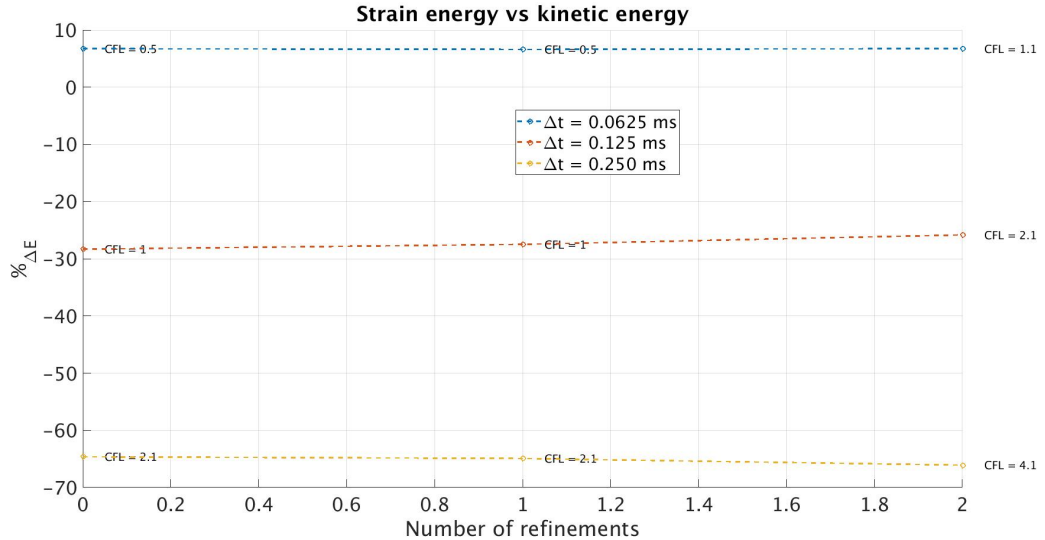*Figure 6.20: Percent difference between stored strain energy in the particle with respect to the kinetic energy before initial contact. Δt is the fluid time step.*

Two other possibilities that can contribute to an error is an incorrect calculated approximation of the coefficient of restitution, The second is the assumption of linear relationship between stress and strain in (5.4) when calculating the strain energy density.

As the particle reached at some point during collision a state of close to zero velocity, it is therefore a more reasonable assumption that all or nearly all of the kinetic energy should be converted into potential energy the particle due to deformation in the form of strain energy. By that reasoning the fluid time steps 0.125 ms and 0.250 ms seem to significantly under predict the strain energy with roughly -30% and -65% respectively. This indicates that the contact has not been resolved accurately for solid time steps 0.125/5 ms = 0.025 ms and above. The same trend can be seen in figure 6.19 as there is considerable difference in the loss of momentum for different time steps. It is more difficult to draw any definitive conclusions from the loss of momentum but seems to further validate the size of the time step needed to resolve the contact.

The results of the study of particle-wall contact seems to be in line with the particle-particle contact study in section 6.3.1. In order to accurately resolve the contact between particle and wall the solid time step should be 0.0125 ms or less. As there existed a hierarchy between the different mesh refinements, the wall refinements does not affect the accuracy as long as it has lower or the same refinement as the particles. Therefore the refinement at the wall is more of an consideration towards resolving the boundary layer of the fluid. Previous mesh independence studies, presented in section 4.2, has shown to accurately resolve the boundary layer for laminar flows for all cell sizes tested in this study. As to be certain that the boundary layer is accurately resolved, having one refinement is considered to be sufficient. This means that the wall has a lower refinement compared with the particles and therefore no further consideration towards collision with respect to wall refinement needs to be taken.

6.4 Additional findings

As shown in section 3.2.3 the parameters β and γ in the Newmark algorithm can cause numerical damping. When the same type of system as in the used in the investigation of Rayleigh damping it was discovered that for $\beta = 0.25$ and $\gamma = 0.5$ the system displayed stability issues. As some numerical oscillations occurred in the system these were amplified in the subsequent time steps and after a period of time led to divergence in the solution. Using the same set-up with $\beta = 0.3025$ and $\gamma = 0.6$ these oscillations diminished in subsequent time steps and the system retained stability. The system in question seems therefore to be sensitive and prone to divergence due to numerical oscillation if not damped by some means. The damping of the Newmark algorithm acts on low frequencies unlike the Rayleigh β that was studied which act upon high frequencies.

6.5 Investigation of pipe restriction

In this section the simulation results from the pipe restriction is presented as described in section 5.4. The simulations with a high concentration of particles were only done using the low viscosity fluid. Simulations containing a single particle was done with both the high and low viscosity fluid.

As can be seen in table 6.1 there is a significant difference in Stokes number for the low and high viscosity fluid in both pipes. The Stokes number was calculated as [16]

$$
\begin{cases}
Stokes = \dfrac{\tau_v U}{D} \\[2mm]
\tau_v = \dfrac{\rho_s L^2}{18\mu_f} \dfrac{24}{C_D Re} \\[2mm]
C_D = \dfrac{27}{Re^{0.84}}
\end{cases}
, \tag{6.1}
$$

where τ_v is the characteristic response time of the solid, L is the side length of the particle, μ_f is the fluid dynamic viscosity, C_D is the drag coefficient and ρ_s is the solid density. The smallest pipe diameter, 16 mm and 26 mm for each case, was used for the pipe diameter D with their respective fluid velocity U. A higher Stokes number means that the ratio between response time of solid and fluid increases. It can be thought of as measurement between solid objects inertia in the fluid. As the ratio increases the time needed for the particle to adjust to changes in the flow becomes longer. In both pipes the particle has a approximately five times longer response time in the low viscosity compared with the high viscosity. In the 16 mm pipe with low viscosity the Stokes number is above unity, meaning that the response time of the solid is longer than the fluid. This means that the particles might not follow the flow completely and move it a different path in a short time line. It should be noted that the highest Stokes number calculated is still relatively low. The importance lay in the difference and ratio in Stokes number between the low and high viscosity fluid.

STOKES NUMBER	16 mm pipe	26 mm pipe
Low viscosity	2.594	0.6533
High viscosity	0.5457	0.1374

Table 6.1: Stokes number for different the different cases.

6.5.1 16 mm pipe with 10 mm particles

One particle

When observing the maximum stress with respect to particle position in the pipe in figure 6.21 for both viscosities, it shows that the peaks occur around the contraction and shortly after it has entered the small section. These peaks are due to collision with the wall. The magnitude of the peak maximum nodal stress are relatively close for both cases. However when observing the quartile in figure 6.22 the is a large difference between the two cases. The quartile is the range between the first and third quantile in statistics. In other words, it is a range of stress with the mean nodal stress value in the middle. The range is 50% av all nodal stresses taken around the mean nodal stress. For the low viscosity, the peak stress for maximum and quartile stress is the same. For the high viscosity, there is a large difference. This suggest that the majority of the particle in the high viscosity fluid is subjected to less stress compared with the low viscosity fluid. As the stress occurred due contact with the wall, the collision seems to be more gentle in the high viscosity. This would indicate that the high viscosity creates a greater damping effect and decelerates the particle, making the collision overall more gentle towards the majority of the particle volume. When reviewing the animation of the simulation in Paraview, subjectively it would seem as the particle in the low viscosity seemed to be more "volatile". Meaning that it tended to bounce around more and thus subjecting the particle more frequently to collision with the wall and perhaps higher stresses compared with the high viscosity fluid. The number of individual contacts were approximated using the maximum penalty of the particle. The maximum penalty is a relative measure of the maximum overlap between to solid phases during contact. An approximation of a single contact event was considered to occur if the maximum penalty was higher than zero and less than 10^{-5} for the previous time step. The bottom threshold of 10^{-5} was chosen instead of zero to avoid any possible numerical oscillations around zero and increase certainty that it is a single contact. By this the number of contacts were calculated to be 177 and 13 for the low and high viscosity respectively. This method is highly approximate and might not be a complete accurate approach. However there is such significant difference in number of contacts that perhaps can not be explained purely by induced errors. It does therefore seem as there does occur more contacts in the low viscosity fluid. The intensity of each calculated contact is unknown, so the stress magnitude subjected to the particle is also unknown for each contact. These findings do seem to be in line with the hypothesis of the increased damping effect in high viscosity fluid before collision and perhaps making the contact less frequent and the flow more gentle in that regard.

(a) Low viscosity

(b) High viscosity

Figure 6.21: The maximum nodal stress on the particle with respect to x-position for different viscosities in the 16 mm pipe.

(a) Low viscosity

(b) High viscosity
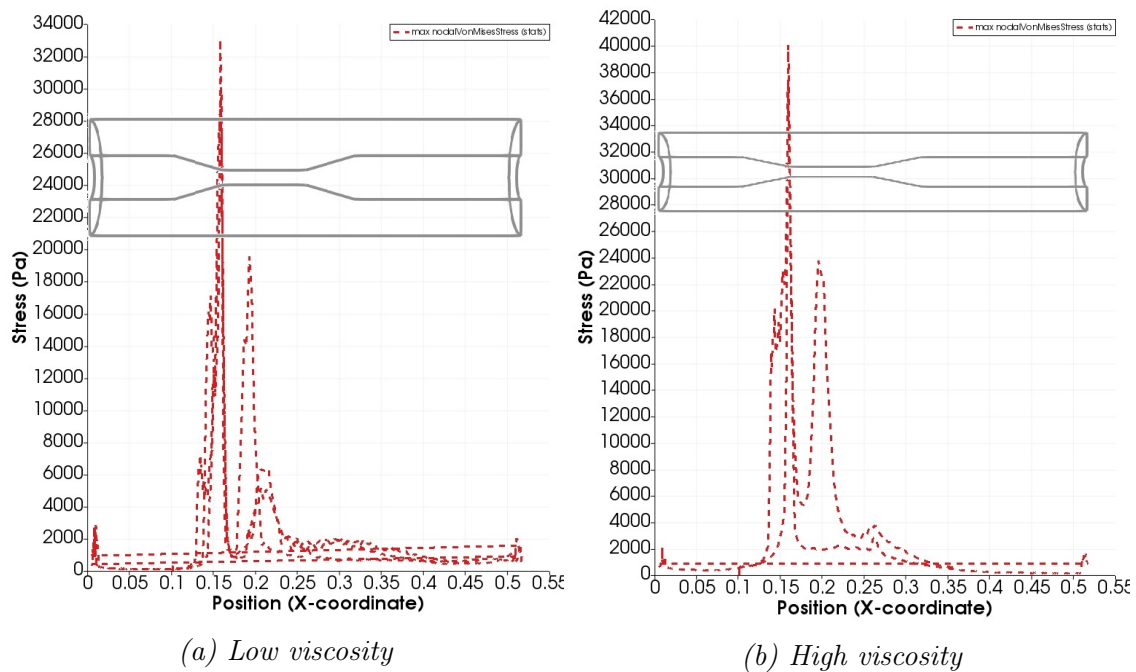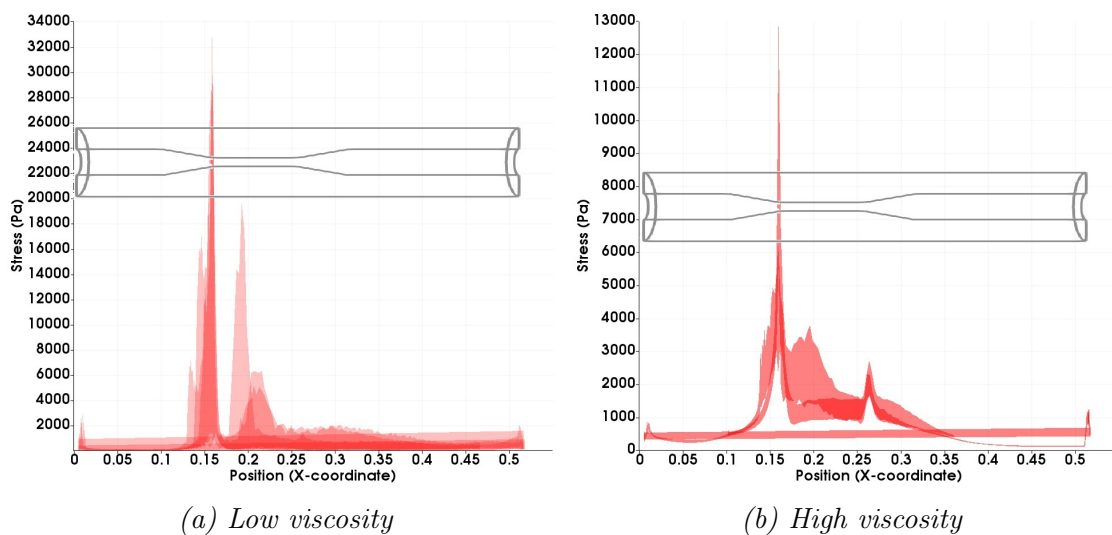
Figure 6.22: Quartile nodal stress on the particle with respect to x-position for different viscosities in the 16 mm pipe.

49

Figure 6.24 shows the shear stress subjected to the particle as it enters the contraction for both the low and high viscosity fluid without any contact with the wall. They are taken at the moment when the shear stress is largest. As shown, each particle in the two cases are at roughly the same position in the pipe. It can be seen from the histogram that the stress distribution across the particle resembles a normal distribution. The majority of the nodes lay around the mean stress and shows that pure shear seem to affect a large part of the entire particle volume. This is confirmed by viewing the corresponding stress field for each case. There is a significant difference in stress magnitude on the particle between the low and high viscosity fluid. The high viscosity fluid subjects the particle to roughly 2.5 times higher shear stress compared with the low viscosity fluid. This might be explained in part by looking at the Stokes number in table 6.1. The Stokes number is a factor 5 lower for the high viscosity compared with the low viscosity. With increasing Stokes number it is expected to occur increased slip at the particle surface in areas of accelerating fluid flow. This is due to an increased inertia of the particle in the fluid flow. In turn it should increase the shear stress on the particle. This argument is contradicting with what is seen in the simulations. However as the Stokes number is rather low for all cases it is therefore assumed to exist low slip and thus have no significant affect on the shear stress subjected to the particle. In theory, if the system would have had a much higher Stokes number an increased shear stress might be seen due to increased slip.

(a) Low viscosity   (b) High viscosity
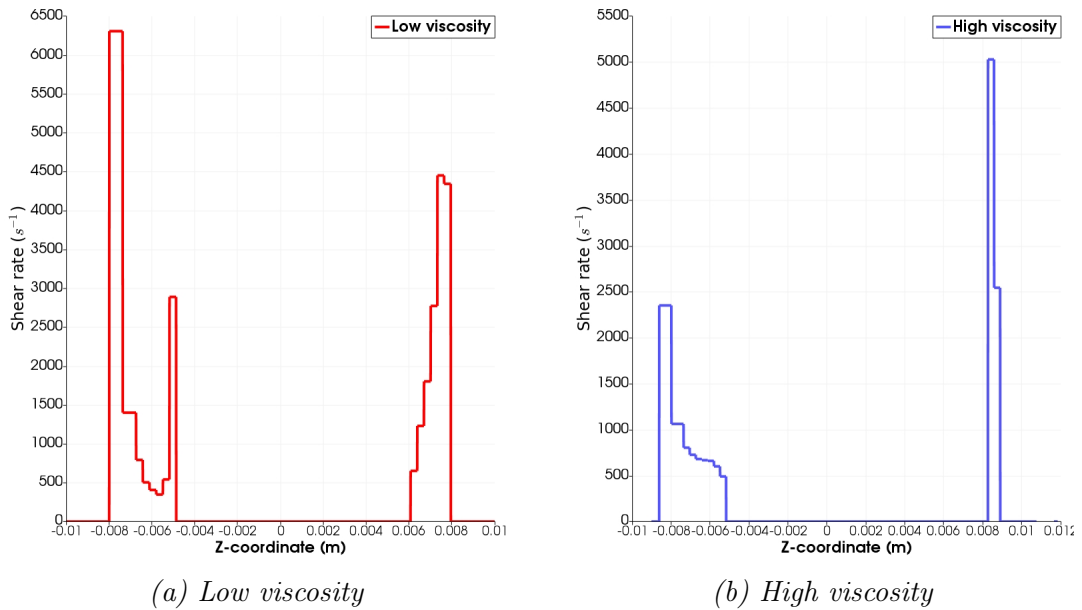
Figure 6.23: Shear rate plotted along a vertical line from the shearing of the particles shown in figure 6.24. The line passes approximately through the area of maximum shear stress on each particle.

The shear stress in a fluid is proportional as

$$\tau \propto K\dot{\gamma}^n \tag{6.2}$$

In figure 6.23 the shear rate is taken along a vertical line through the corresponding particle in figure 6.24. In the areas of the plot where the shear rate is zero is because

50

the line goes through a solid object. The area below -0.008 m and above 0.008 m is the pipe wall and the zero shear rate in the middle is the particle. The maximum share rate at the particle surface is approximately 3000 s^{-1} and 5000 s^{-1} for the low and high viscosity fluid. By using these shear rates, the ratio in shear stress between high and low viscosity using (6.2) is calculated to be 4.45. This theoretical value is higher than the ratio in shear stress for the particles, but shows the same trend. It does therefore seem to be valid that there does exist a large difference in shear stress subjected on the particle by the different fluids.
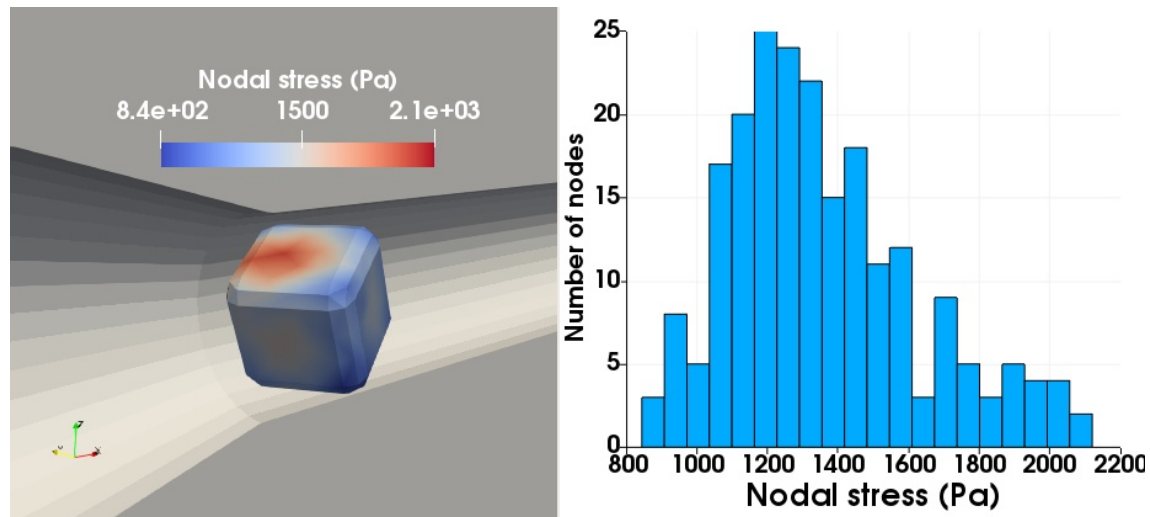
(a) Low viscosity
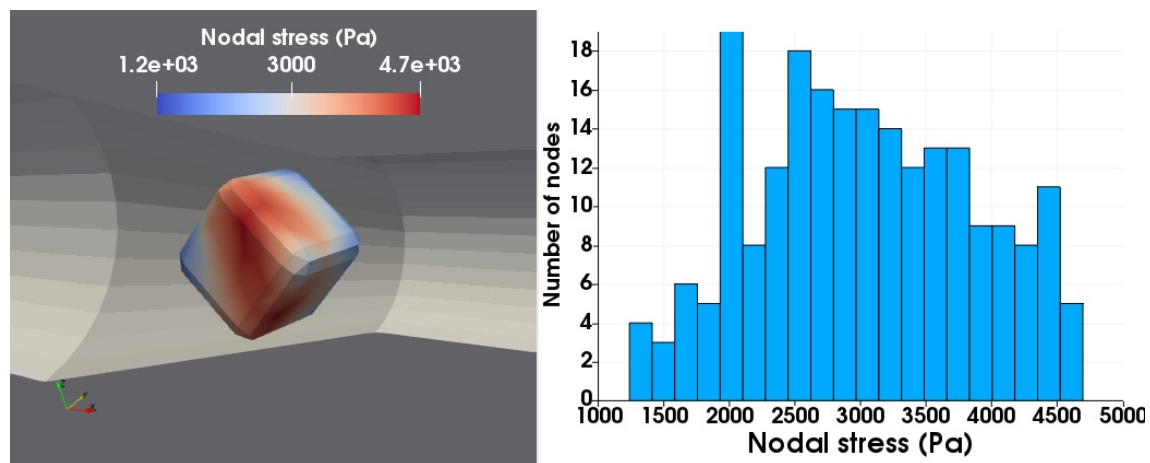
(b) High viscosity

Figure 6.24: Stress field of the particle due to shearing in the contraction of the 16 mm pipe with corresponding histogram of the nodal stresses.

High concentration

The simulation was ran for approximately 24 days with an average of 107 seconds per time step and produced a simulation length of about 1.20 seconds. Each particle passed through the entire simulation domain between 0.65-5 times, with an average of 1.68 passing's per particle. The large difference in number of passes through the

domain for each particle is due to the recirculation after the expansion. The particles get stuck in these recirculations and remain there for a long period of time. The simulation reached a state of approximately homogeneous distribution of particles around 0.4 seconds.

In figure 6.25 the maximum nodal stress for each individual particle with the low viscosity fluid, each with a different color, with respect to position in the pipe is shown. The small peaks at the inlet of the pipe is to due to the cyclic boundary condition that treats the particles. In reality these peaks do not exist at this location. Otherwise at the inlet the maximum stress is significantly lower compared with the rest of the domain, which was expected.
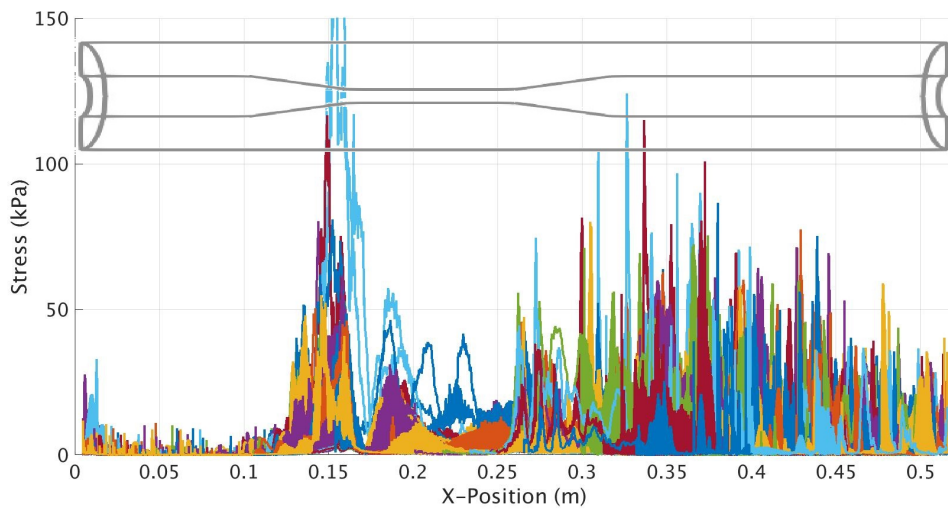
Figure 6.25: Maximum stress at different locations in the 16 mm pipe with the low viscosity fluid. Each color represent an individual particle.

In the contraction there are some large peaks in maximum nodal stress. These were determined to be due to squeezing of two or more particles as they enter the contraction, particle colliding with the wall, or a combination of the two. The peak colored in light blue at the contraction was caused by squeezing and is visually presented in figure 6.26. Four separate cases of squeezing in the contraction were identified. Their mean and maximum stress are presented in figure 6.27 with vertical bars showing the entire stress range in the particle. The phenomena described as squeezing seem to vary both in magnitude and how much of the particle that is effected, as no obvious trend can be seen. The mean stress is in one case close to the median indicating that a large part of the particle is subjected to high stress. In another case the mean stress is low as in the figure in the bottom right. Thereby indicating that only a small part of the particle is subjected to a high stresses. Apart from these observations the maximum stress for squeezing of particles in these cases are around 20-60 kPa, with one exception of a peak at 300 kPa.

In the pipe with a minimum inner diameter of 16 mm there exist large areas of recirculation after the expansion as seen in figure 6.28 and 6.29. This is due to a large jet at the center of the pipe with a velocity around 4 m/s. This causes particles to "get caught" in these recirculation zones and become either stationary or

Figure 6.26: Squeezing of particles at the contraction of the 16 mm pipe with the low viscosity fluid with corresponding histogram of the particle under the highest stress to the left.
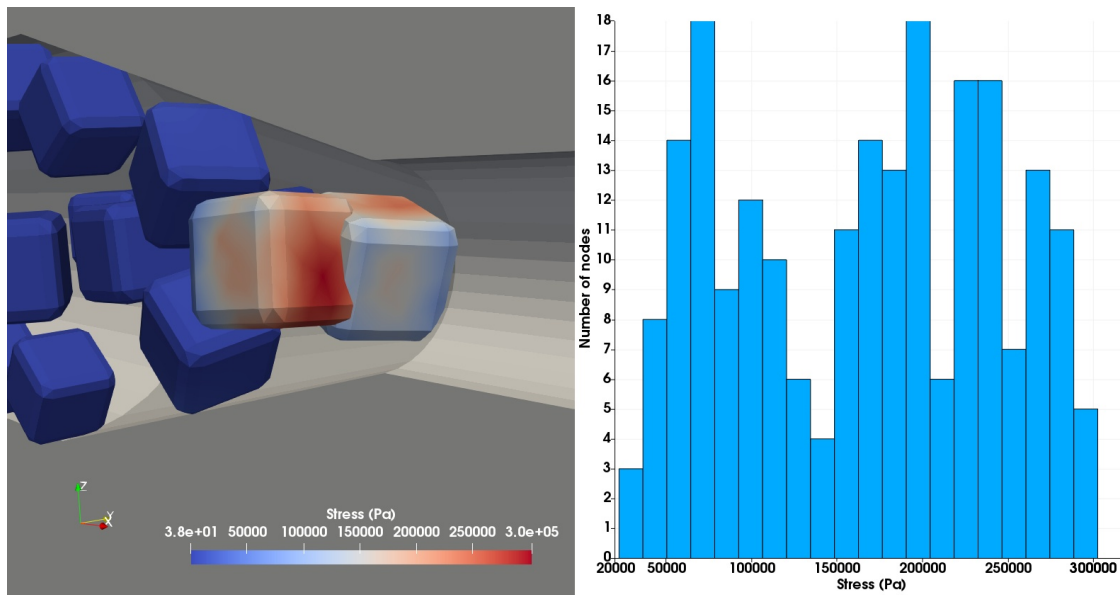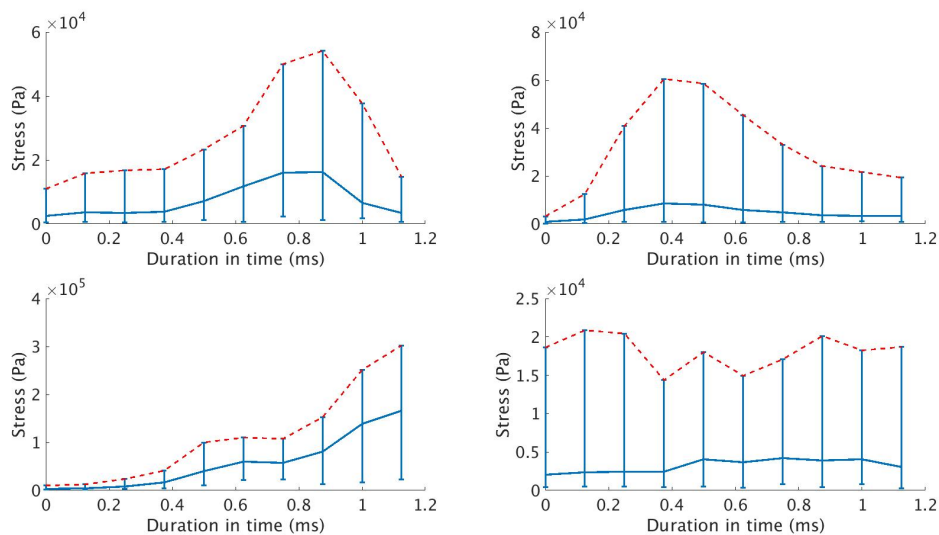

Figure 6.27: Four cases of particle squeezing in the contraction of the 16 mm pipe with the low viscosity fluid from when the event begins until the end. Mean nodal stress (blue) with corresponding nodal stress range and maximum stress (red).

53

moving in the opposite direction with respect to the main flow direction. In figure 6.28 particles colored in purple are caught by the fluid recirculation and moving against the main flow. In general all particles that are close to the wall are either stationary or moving slow, either in the opposite or in the same direction as the main flow. When looking at the high speed videos captured on the experiment the same behaviour of the particles could be seen. This increases the validity of the particle and flow behaviour that the simulation is predicting as it seems to resemble reality fairly closely.
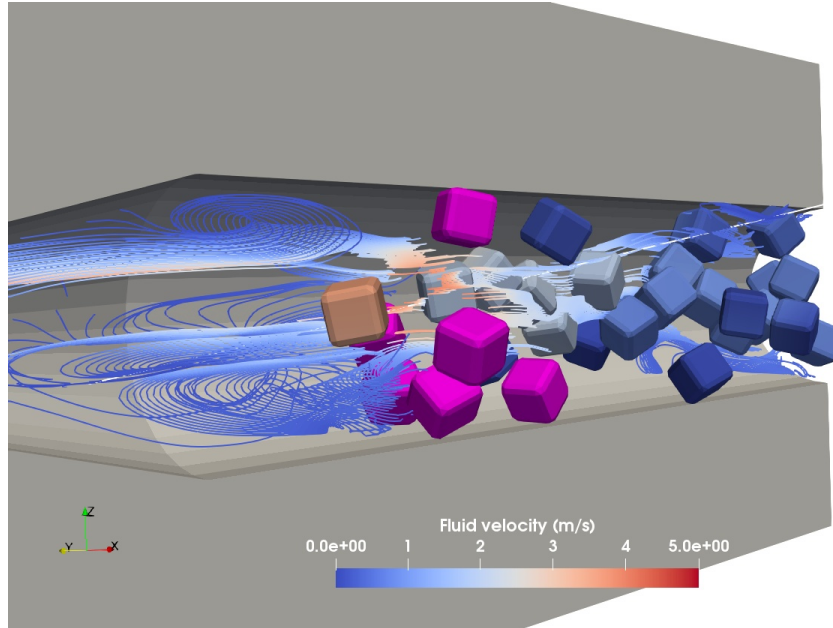
Figure 6.28: Particles after the expansion in the 16 mm pipe with the low viscosity fluid. Purple particles denote particles moving in the opposite direction to the main flow.

The recirculation causes particles to remain stationary and was found to be the main factor towards high velocity collision between particles at the expansion in the 16 mm pipe. This means that particles exiting the small part of the pipe at a velocity of about 4 m/s collide with stationary particles. An example of these collisions is depicted in figure 6.30 and has a maximum stress of about 65 kPa. From the histogram of nodal stress it can be seen that only a small part of the particle is subjected a high or close to the maximum stress. The majority of the particle is below 10 kPa. Four cases of particle collision with mean and max stress is depicted in 6.31. It can be seen that the peak maximum stress only occurs during a short period of time, meaning that it is a high impulse collision. For all cases the maximum stress is around 50 kPa with minor variations. The average stress subjected to the particle is much lower than the maximum stress. This would indicate, similar to the histogram in figure 6.30, that particle collision only effects a small part of the entire particle volume. The same was seen when looking at other cases, not presented here, of particle collision after the expansion.

In figure 6.32 the maximum stress of any particle with respect to different locations in the pipe over time is shown. The purpose of these plots is to visualize the the maximum stress of any particle in three distinct different areas of the pipe. It can

Figure 6.29: Figure of both fluid and particle velocity at the 16 mm pipe expansion with the low viscosity fluid.

Figure 6.30: Particle collision after expansion in the 16 mm pipe with the low viscosity fluid with corresponding histogram of one of the particles in contact. The histogram is taken from the particle with the highest stress in the middle of the image.

55

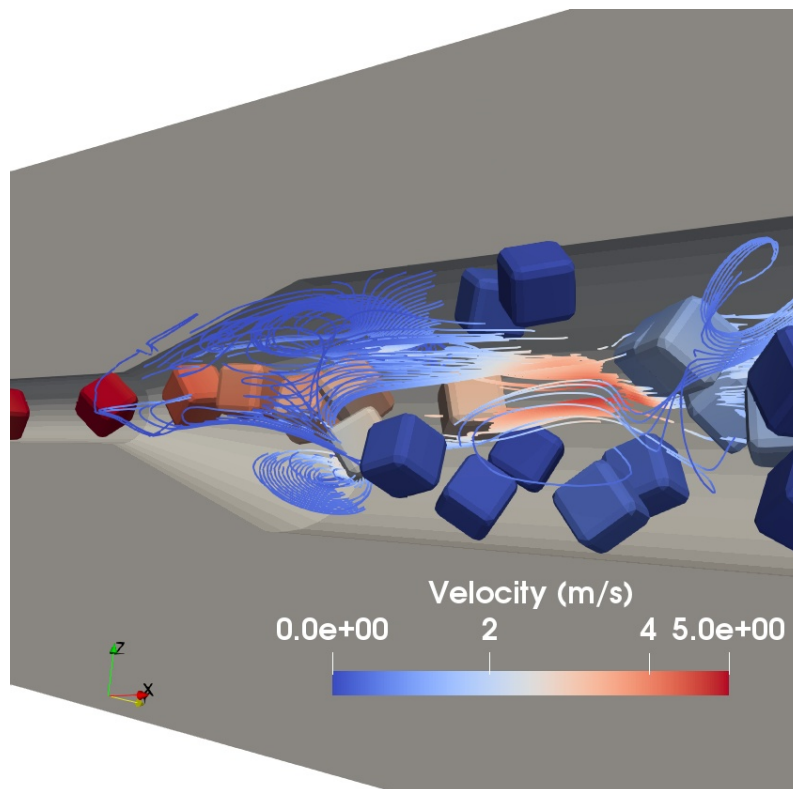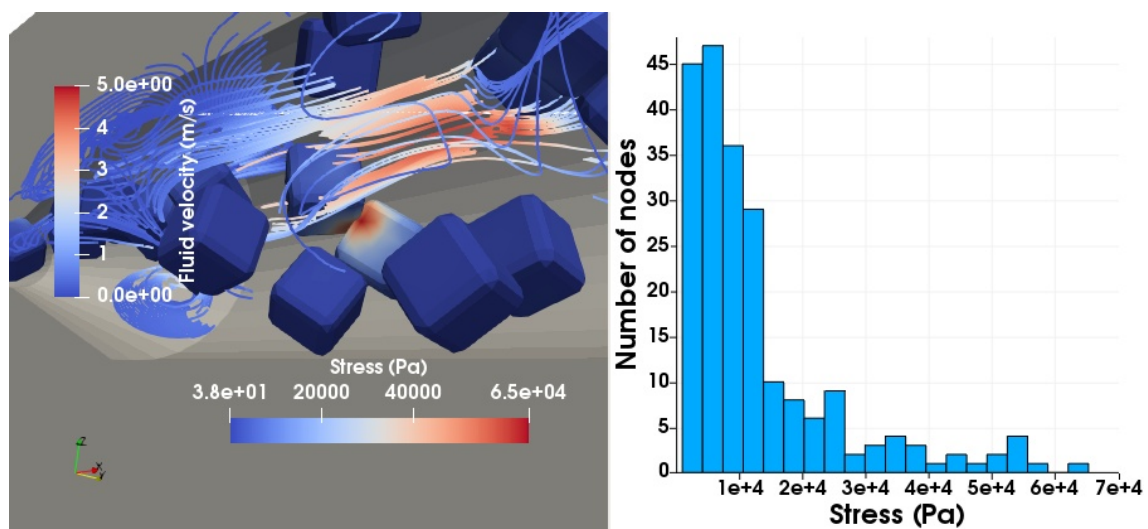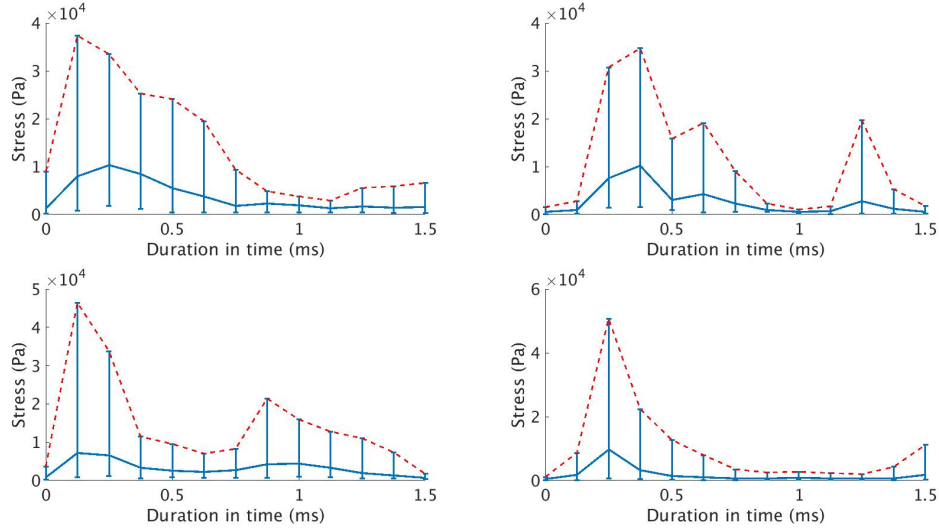*Figure 6.31: Four cases of particle collision after the expansion in the 16 mm pipe with the low viscosity fluid from when contact initiates until contact ends. Mean nodal stress (blue) with corresponding nodal stress range and maximum stress (red).*

give some insight into how the areas might affect the particles over time. For the contraction and up stream in figure 6.32a, the highest stress is prior to reaching an even distribution of particles. It is therefore uncertain if this peak is due to the computational set-up of the system or something that could occur in reality. Similar could be seen in figure 6.32b for the small pipe section. The individual peaks of high stress for the contraction and small pipe are infrequent in comparison to the expansion in figure 6.32c. The phenomena that creates these high stresses in the expansion occur frequently and continuously over time.

With regards to the magnitude of the maximum stress in each section, the small pipe section is significantly lower than contraction and expansion. From the simulation that was seen to be due to as the particle enters the contraction there is a lot of contact with the wall and other particles. However as soon as the particles enter the small pipe they flow through with only minor wall or particle contact. This was confirmed to be realistic as the high speed video displayed the same behaviour. In the contraction the stress peaks are about 20 kPa, with a few exceptions of higher peaks. In the expansion the peak stresses are more frequent and higher in magnitude. The magnitude of the stress varies greatly, but peaks up towards 120 kPa can be seen even after even distribution of particles has developed. It should be noted that the duration of the simulation is only roughly 1.2 seconds and relatively short to be able to draw any definitive conclusions from. It is however a good indicator of might be expected to occur when particles pass through this system over a longer period of time.

56
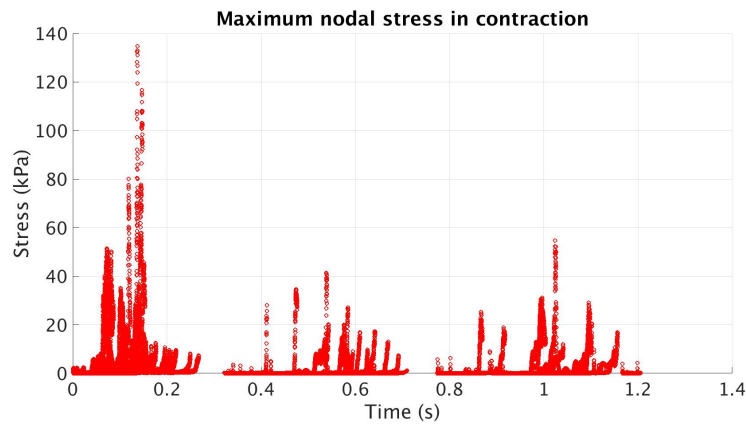
(a) Contraction and before
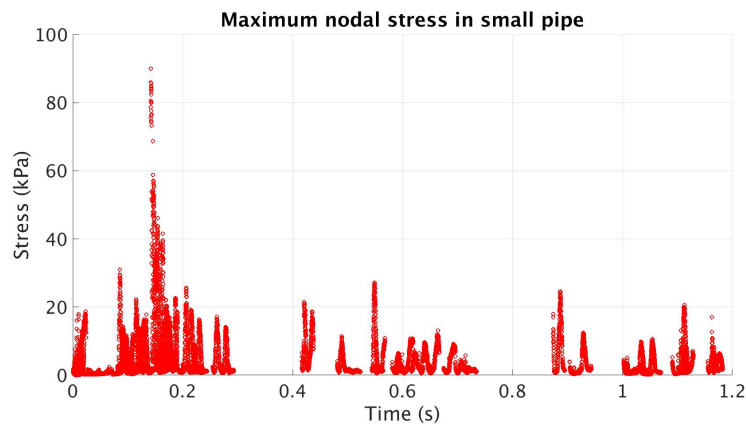
(b) In the small pipe
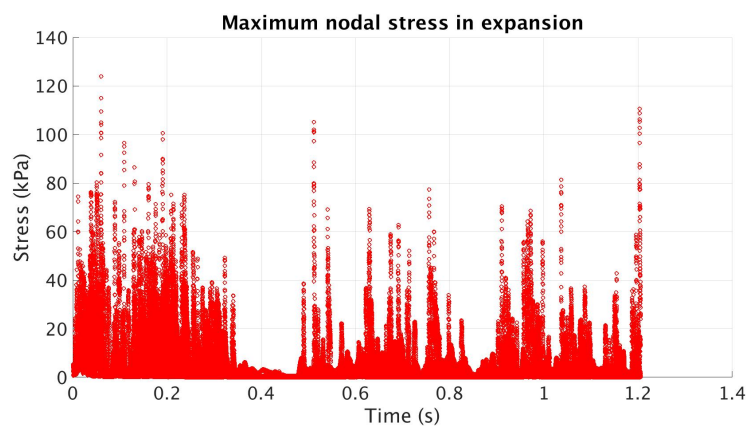
(c) Expansion and after

Figure 6.32: Maximum stress over time in different areas in the entire 16 mm pipe with the low viscosity fluid.

6.5.2   26 mm pipe with 10 mm particles

One particle

In figure 6.33 the maximum nodal stress is plotted with respect the the particle position in the pipe. There is a significant difference in stress magnitude. The drawn lines from the outlet to the inlet is due to when the particle exits the outlet and enters the inlet with the cyclic boundary condition. It treats it as the same point in the simulation both with different coordinates thus creating this effect in the plots. By comparing it to figure 6.34 the average stress for the high viscosity fluid is relatively close to the maximum stress. For the low viscosity fluid there is a large difference. This seem to imply that only a small part of the particle is subjected to a high stress in the low viscosity, as occurs during collision. It was confirmed that the peaks in the low viscosity was due to particle-wall contact and only affected a small region of the particle. This seemed to be due to the same damping effect as discussed for the 16 mm pipe in section 6.5.1. However the overall stress level is significantly lower in the 26 mm pipe compared with the 16 mm pipe stress in figure 6.25. This is thought to be partly because of the lower in fluid velocity in the contraction of the 26 mm pipe. Another possibility is the increased ratio between smallest pipe diameter and particle size. The particle has more space to move around in the 26 mm pipe without hitting the wall. The Stokes number is also lower with the same fluid viscosity. For the high viscosity fluid the Stokes number is 0.1374 in the 26 mm pipe, a factor 5 lower compared with the low viscosity. This might be another reason why the particle does not seem to collide with the wall. The time response of the particle in the high viscosity fluid is fast enough for the particle to follow the fluid flow and avoid any contact with the wall.
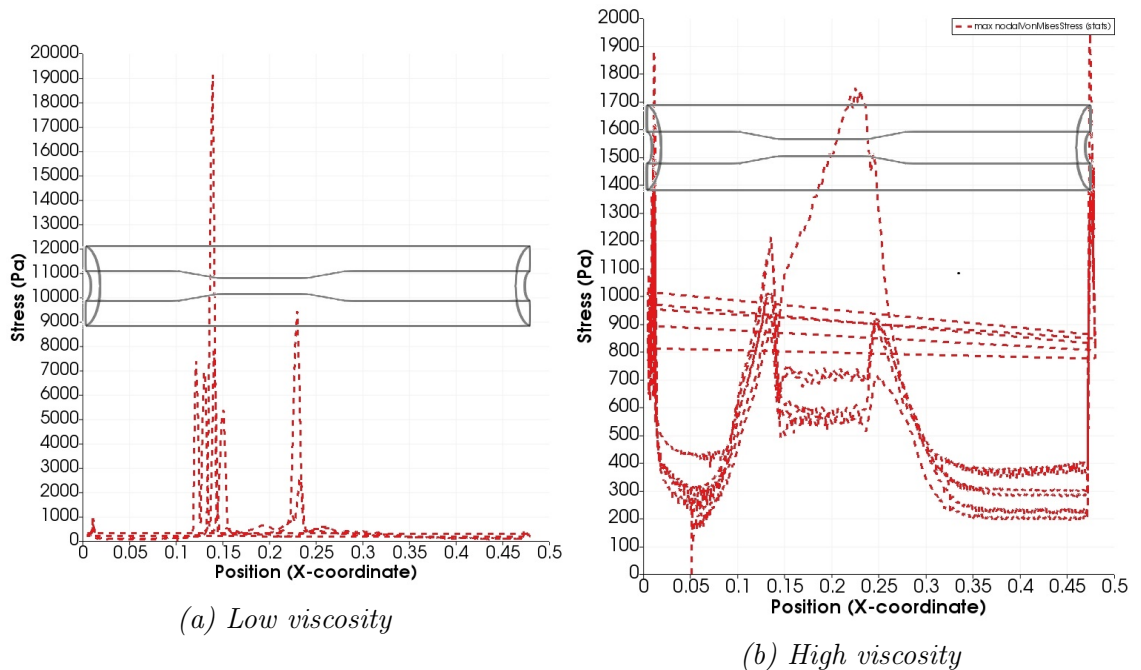
(a) Low viscosity

(b) High viscosity

Figure 6.33: *The maximum nodal stress on the particle with respect to x-position for different viscosities.*

(a) Low viscosity
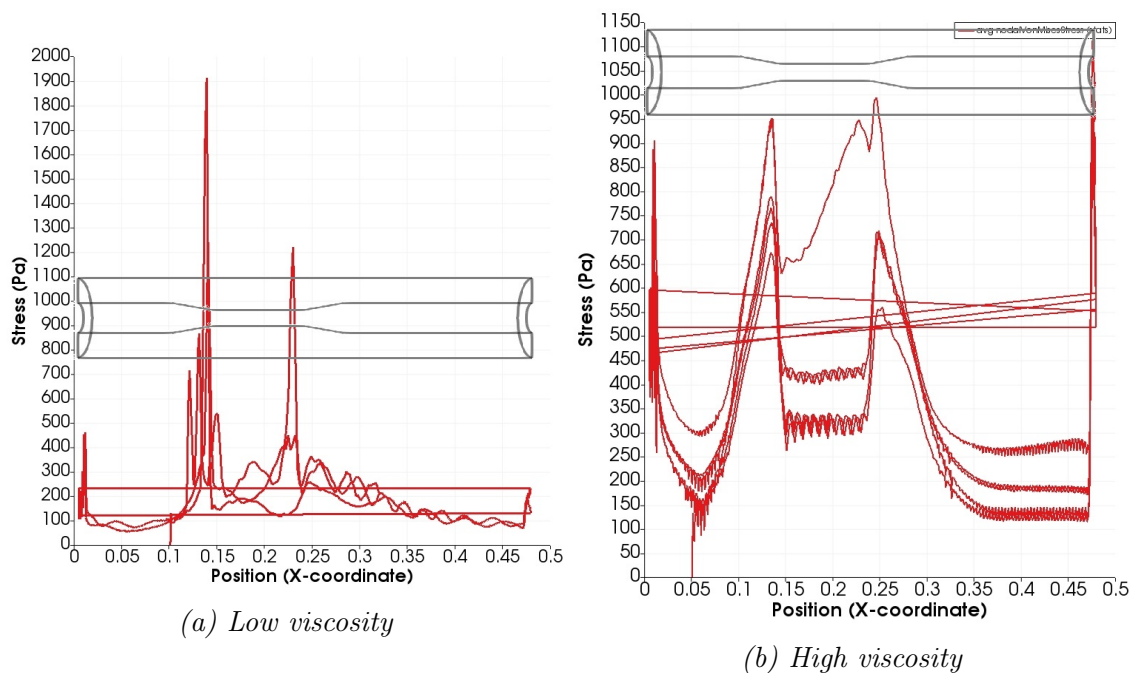
(b) High viscosity

Figure 6.34: The average nodal stress on the particle with respect to x-position for different viscosities.

Similar to the 16 mm pipe there is a significant difference in shear stress on the particle in the low and high viscosity fluid. In figure 6.35 the particle is subjected to shear stress with corresponding histogram of the nodal stress distribution for each viscosity. By taking the same argument for the difference in shear stress as previously, the difference seen in the 26 mm pipe does also seem valid. The ratio in shear stress magnitude on the particle between the low and high viscosity fluid is around two. Overall the 26 mm pipe seem to much more gentle towards the particle with regard to stress level, both in shearing and collision.

In conclusion for a single particle, shear stress subjected on particle by the fluid occurs every time it goes through the contraction due to the acceleration of the fluid flow field. A large part of the particle is subjected to the same level of stress due to the shearing when not in contact with the wall. The shear stress is significantly higher in the high viscosity fluid compared with the low viscosity fluid. Collision subjects the particle to a much higher stress compared with shearing but might occurs less frequent. The number of collisions depends on the viscosity of the fluid. The high viscosity fluid prevents the particle from ever colliding with the wall. Collision with the wall only effects a small part of the entire particle volume but with high stress. It should be emphasized that is only for a single particle. Different behaviour is could be possible for a higher number of particles.
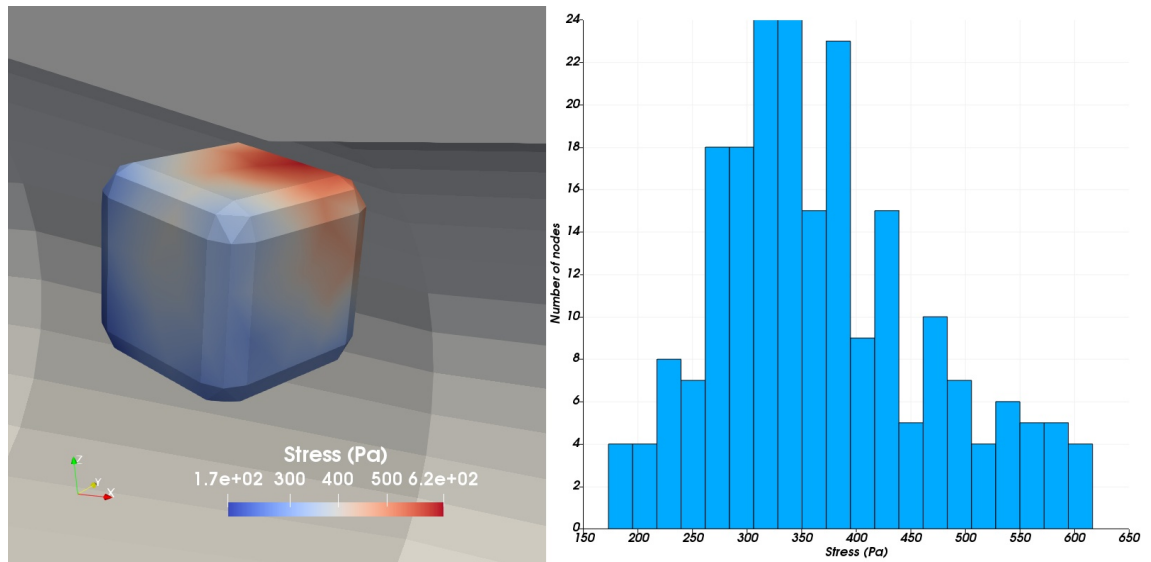
(a) Low viscosity
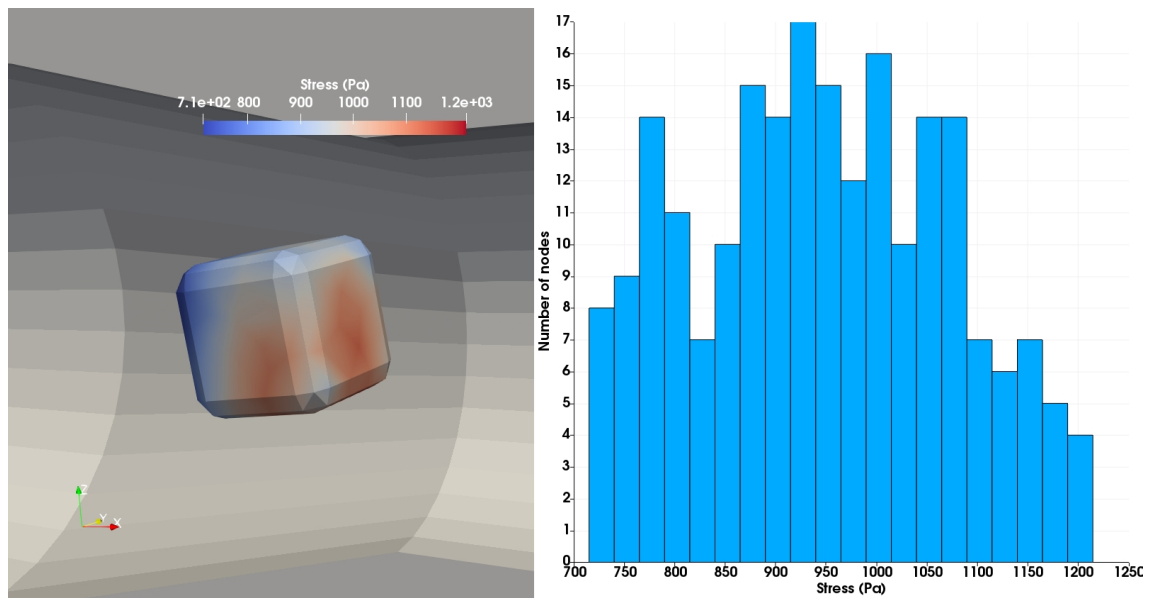
(b) High viscosity

Figure 6.35: Stress field of the particle due to shearing in the contraction with corresponding histogram of the nodal stress.

High concentration

The simulation was ran for approximately ten days with an average of 93 seconds per time step and produced a simulation length of 1.15 seconds. Each particle passed through the entire simulation domain between 2-3 times, with an average of 2.3 passing's per particle. The simulation reached state of approximately homogeneous distribution of particles around 0.4 seconds.

There existed no areas of recirculation in the expansion for the 26 mm pipe with the low viscosity fluid. This meant that high velocity impact between particle never occurred as they did in the 16 mm pipe. This is due to the significantly lower velocity and larger area of the jet at the expansion. Another implication of not having any recirculation was that the particles tended to stay grouped together in the center of the fluid flow as can be seen in figure 6.36. Due to these flow conditions minimal contact between particle and wall could be seen. Particle-particle contact was much more common, but as the particles had nearly the same velocity these contact were much less severe in comparison to the 16 mm pipe.
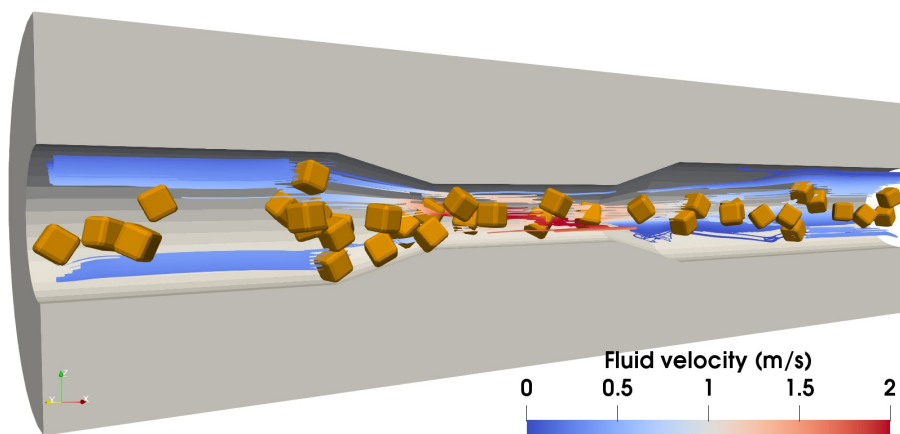
Figure 6.36: Visualization of the simulation as particles has reached a homogeneous distribution in the entire domain with fluid stream lines.

In figure 6.37 the maximum stress of any particles in three different areas can be seen. All areas show similar magnitude of maximum stress between approximately 10-20 kPa as the particles has reached a homogeneous distribution after 0.4 seconds. By observing maximum stress in the expansion in figure 6.37c it can be seen that the majority of the peaks are before 0.4 seconds. This is prior to the particles reaching a homogeneous distribution in the pipe that resembles the experiment. The peaks are due to particle collision after the expansion and is a result of the initial set-up of the simulation. After around 0.35 seconds the maximum stress has significantly decreased with a few peaks between 0.8 and 0.95 seconds with an average of roughly 7500 Pa. These peaks in maximum stress was due to particle-particle collision in the center of the pipe. This might give some indication that in this particular set-up the expansion is an area where the particles are subjected to low stresses with occasional small peaks. It should be noted that the duration of the simulation is only roughly 1.15 seconds and relatively short to be able to draw any definitive conclusions from. It is however a good indicator of might be expected to occur when particles pass

through this system over a longer period of time.
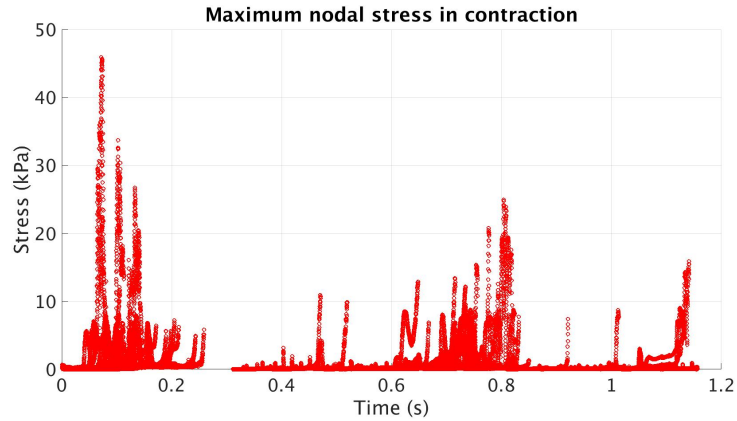
(a) Contraction and before
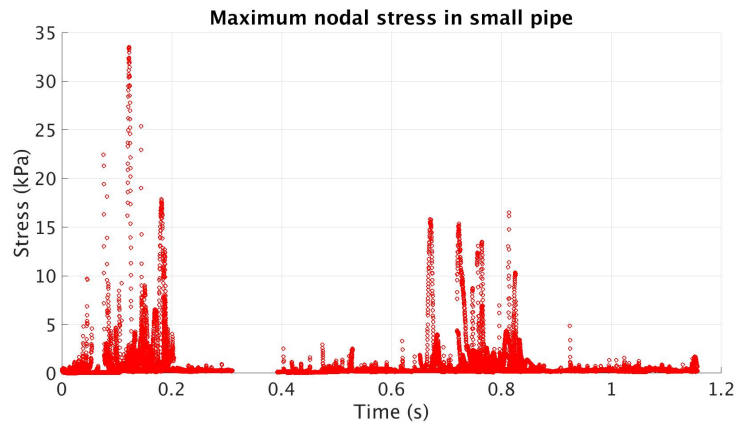
(b) In the small pipe
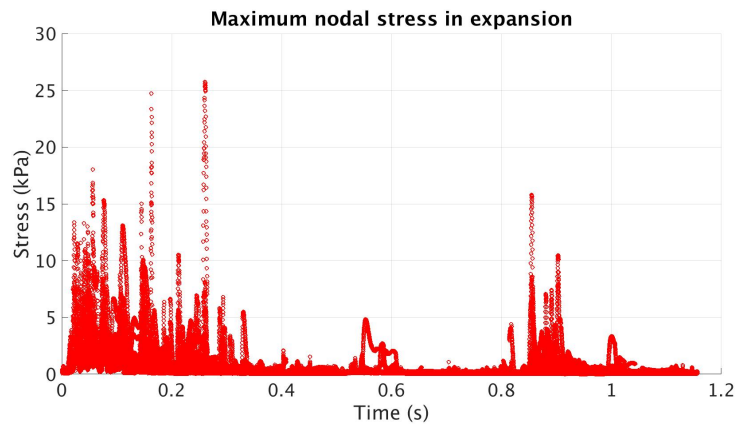
(c) Expansion and after

Figure 6.37: Maximum stress over time in different areas in the entire 26 mm pipe with the low viscosity fluid.

In figure 6.37a there are recurring peaks of maximum stress after 0.4 seconds. This indicates that there exist some phenomena that recurs and causes particles to be subjected to higher stresses. It might be squeezing of particles as seen in 6.39. From visual observation, the phenomena of squeezing in the contraction took place relatively few times. However the number of squeezing events occurring is assumed to
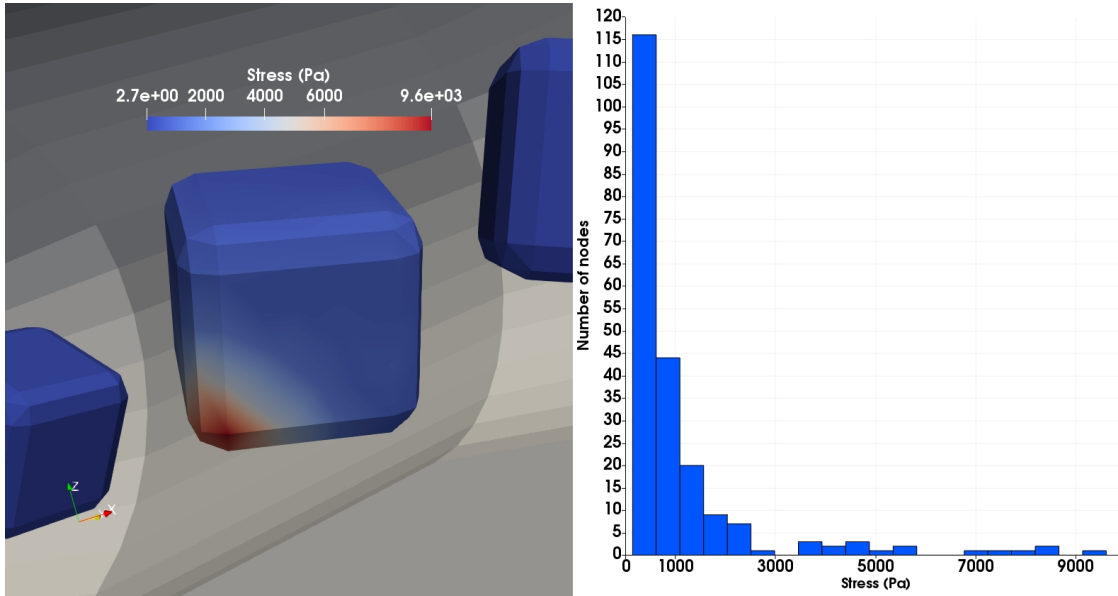
Figure 6.38: Example of particle-wall contact in the 26 mm pipe with the low viscosity fluid with corresponding histogram of the nodal stress in the particle.
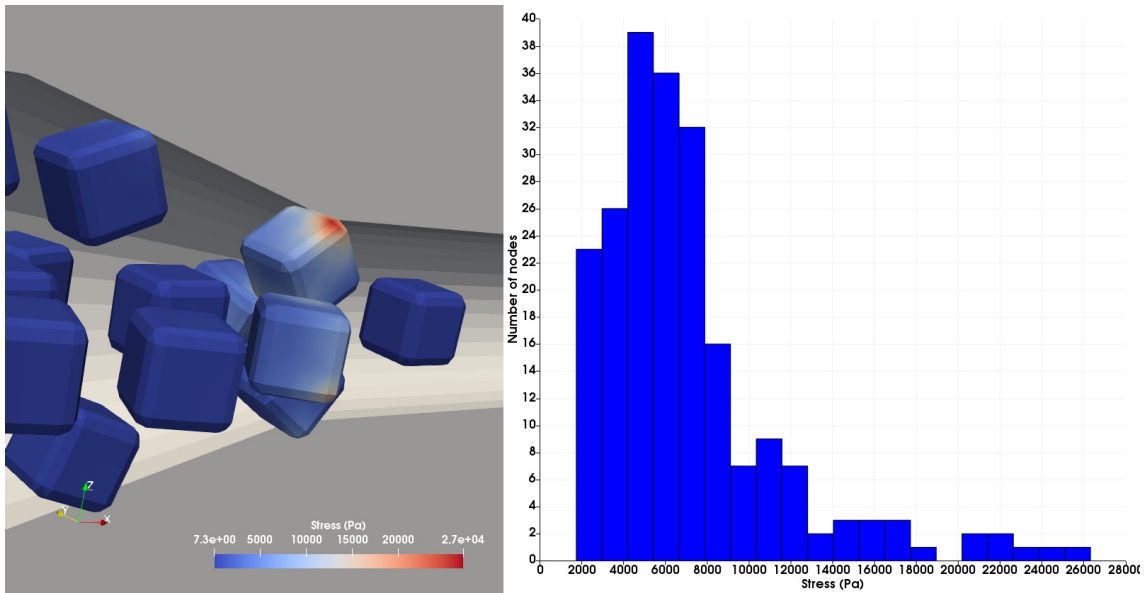
Figure 6.39: Squeezing of particles in the 26mm pipe with the low viscosity fluid with histogram of the stress distribution in the particle at the top.

be directly proportional to the volume concentration of particle. For higher concentrations than used here, squeezing should become an increasingly more common phenomena. A more common event in the contraction was wall collision as depicted in figure 6.38. In the specific case shown, only a small part of the particle is subjected close to the maximum nodal stress. The volume of the particle subjected to maximum stress is however dependent on number of contact points and contact area. For other particle-wall contact cases with "more" contact, a larger part of the particle might be subjected to or close to the maximum nodal stress. This would lead to a larger percentage of the particle being exposed to higher stresses due to more contact points and contact area.
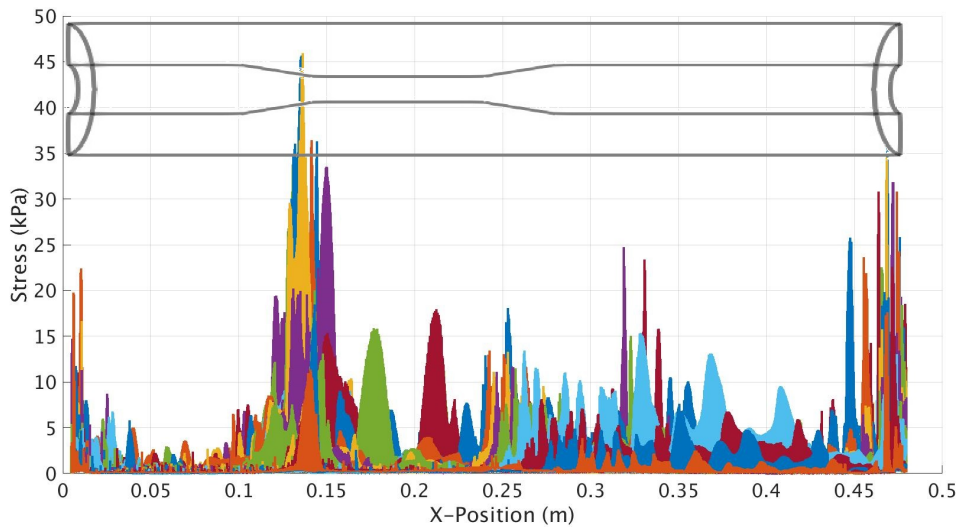
Figure 6.40: Maximum stress at different locations in the 26 mm pipe with the low viscosity fluid. Each color represent an individual particle.

In figure 6.40 the maximum stress of individual particles in different locations in the pipe is depicted. The peaks at the inlet and outlet is due to the treatment of the particles in the cyclic domain and is not physically accurate. From this figure is can be seen that the highest peak stresses occur at the contraction. In comparison to figure 6.37a these peaks can be determined to occur in the first 0.2 seconds of the simulation. Therefore the magnitude of these values should be interpreted with some restriction as the system has not reached a homogeneous distribution. They can however not be neglected, as in reality concentrations and distributions vary. As this level of stress only occurs two or three times in the simulation, it might be something that happens rarely in reality for the same type of system.

6.5.3 26 mm pipe with 17 mm particles

It was discovered that the system was not stable for the large 17 mm particles with a Young's modulus of 0.1 GPa. It showed similar behaviour as the unstable set-up discussed in section 6.2.1, the Young's modulus was therefore increased to 1 GPa from 0.1 GPa. As the particle has increased in size from 10 mm to 17 mm in side length the eigenfrequency has changed. This might be an indication that the eigenfrequency of the particle has an impact on the stability of the system. This is still

a vague hypothesis as mentioned previously and requires further work in order for confirmation.

The shear stress on the 17 mm particle for the low viscosity is similar to 10 mm particle in the same system. The difference in shear stress in the high viscosity fluid between the 17 mm and 10 mm is about 50%. It might be that the high viscosity fluid has a stronger correlation with the particle-pipe size ratio. To confirm this hypothesis further investigation is needed.

The difference in shear stress on the 17 mm particle in the low and high viscosity is about a factor of three. As discussed in previous sections, this seems to be accurate when regarding the shear rate and Stokes number for each case.

Figure 6.41: Shearing of 17 mm particle when entering contraction in the 26 mm pipe with low viscosity fluid.

Figure 6.42: Shearing of 17 mm particle when entering contraction in the 26 mm pipe with high viscosity fluid.

6.6   Comparison with experiments

In this section the results and findings in this thesis work will be compared and discussed with the parallel experimentally focused master's thesis work by Roland and Tuck Hutasingh within the same area.
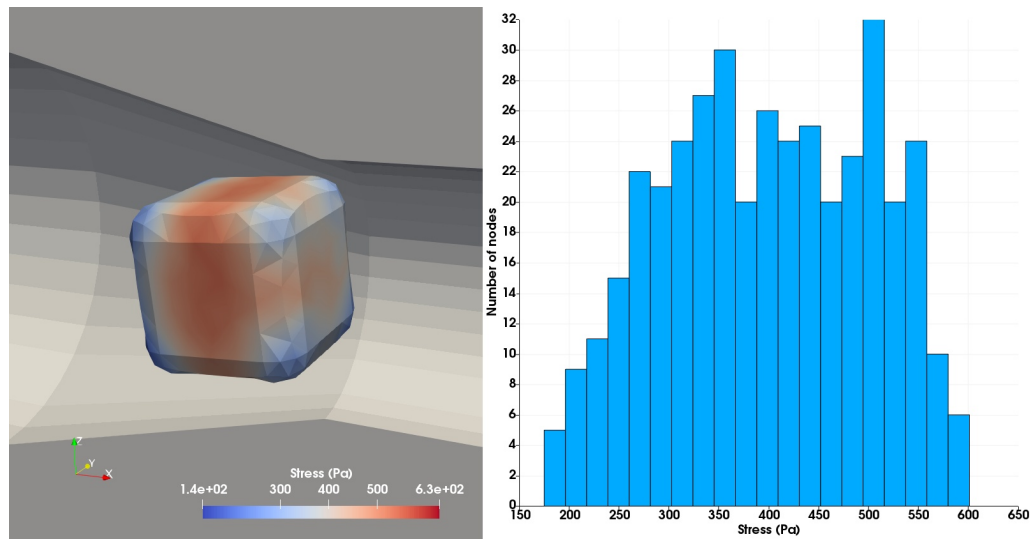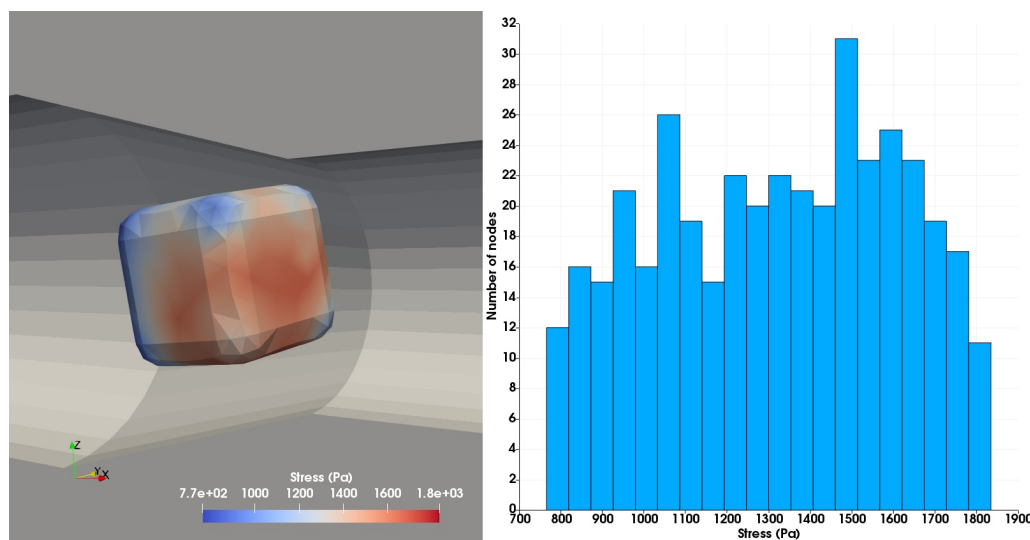
High speed videos were captured during the experiments by Roland and Tuck Hutasingh of mango particles, with an average size of 17 mm, in the low viscosity fluid going through the 26 mm contraction rig. The videos displayed a tendency for the mango particles outer layer of fruit flesh to being ripped off when entering the contraction. This is assumed to be mainly caused by shearing from the fluid. At a few instances a part of the mango particle was partly or completely broken into two separate pieces as it went through the contraction. It is uncertain if this occurs due to the shearing or wall/particle collision, but by subjective observation it seems to be mainly caused by shearing rather than collision. If this assumption is correct, by observing the difference in shear stress on the particle in figures 6.41 and 6.42, the high viscosity fluid should have an increased affect on the mango's integrity. This due to the higher viscosity subjecting the particle to a higher shear stress. In theory the mango should therefore experience more breakage and tearing of fruit flesh in the high viscosity fluid as it seemed to be more sensitive towards shearing than collision.

From the experiments by Roland and Tuck Hutasingh they concluded that no significant breakage could be seen for either the mango or the potato in the 26 mm and 16 mm pipe respectively with the low viscosity fluid. The carrot did show some breakage in the 16 mm pipe with low viscosity. However it was still relatively low amount of breakage to draw any decisive conclusions from. In table 6.2 the results of a compression test for three different types of sample can be seen. The bio-yield stress refers to the stress where initial breakage of the sample occurs and the load it can withstand decreases. In table 6.3 approximated stress levels that are expected to occur for each identified phenomena in each pipe can be seen. Note that these are highly approximate and taken from data presented in previous sections with the assumption that the simulations has predicted a correct stress level. Another point to consider when viewing the stress levels is that each phenomena affect the particle volume differently as dicussed previously. The common maximum stress in the 16 mm pipe and 26 mm pipe with a high concentration of particles ranges from approximately 50-100 kPa and 10-25 kPa respectively. There are some peaks that are higher and bottoms that are lower in maximum stress value for both pipe cases. The level of stress that commonly occurs in the 26 mm pipe is significantly lower than any of the measured bio-yield stresses. This indicates that the particle does not break and remain intact through the contraction rig. However this is highly dependent on the mechanical properties and micro-structure of the sample. This was confirmed by the experiment as no significant breakage due to the contraction could be determined.

Sample	Bio-yield stress
Potato	79 kPa
Carrot	450 kPa
Mango	39 kPa

Table 6.2: Table of measured Bio-yield stress from compression test of each sample extracted from experiments [26].

STRESS LEVEL APPROXIMATION	16 mm pipe		26 mm pipe	
	Low viscosity	High viscosity	Low viscosity	High viscosity
Particle-Particle collision	40-50 kPa	NT	5-10 kPa*	NT
Particle-Wall collision	1-10 kPa	**	1-5 kPa	**
Shearing	900-2100 Pa	1200-4700 Pa	200-600 Pa	700-1200 Pa
Squeezing	20-60 kPa		10-20 kPa	

Table 6.3: Table of approximate expected stress levels for each identified phenomena from the simulations. NT = Not Tested.
* Very uncertain and occurs rarely
** Not enough data for a reasonable approximation

In the 16 mm pipe the range of commonly occurring stress levels are above both the bio-yield of the potato and mango. This was identified to be mainly due to particle-particle collision in the expansion. The bio-yield of the carrot is still significantly higher than the common stress range. This proved to be contradicting as the potato showed no significant breakage while the carrot did. This seem to indicate that the quantification and use of the bio-yield compared with the predicted stress level in the simulation is not an accurate way of predicting breakage. The designed pipe contraction rig might not create a harsh enough environment and flow for the particles to break. However as the experiments showed no significant external breakage of the potato occurred does not prove that there is no internal breakage. As stresses above the bio-yield does occur, the internal structural integrity of the particle might have been weakened and/or broken without any external indications. This is highly unlikely but can not be disregarded as a possibility. More reasonable explanations towards the disagreement in results and predicted stress levels can be made. Firstly, the actual predicted stress level in the simulation might be incorrect. As the Young's modulus was out of necessity towards numerical stability chosen very high which could have influenced the stress level. Another possible source of error in the simulation is the contact model, which is also connected to the Young's modulus to a certain extent. As presented, the contact stiffness had to be subjectively chosen by visual interpretation. This could have introduced a human induced error in the already uncertain applicability of the contact model in this type of problem. Perhaps a different contact model would have provided a better approximation for the collision of soft bio-material. Lastly, as discussed by Roland and Tuck Hutasingh in their experimental work, there exists a level of uncertainty from the experiments and the sampling method due to different factors. Also no previous conducted studies, either experimental or numerical simulation, has been made on this type of system.

Therefore no comparison or validation towards other external work could be made.

Each tested sample had different properties and micro-structure, thus their mechanism of breakage are different as proven by Roland and Tuck Hutasingh in their experimental work. They showed that each sample had a unique fracture mechanism and characteristic. The potatoes tended to have corners being chipped off, making them more spherical. The carrots tended to split along the structural fibers, creating two separate oblong particles. The mango tended to have its outer fruit flesh ripped and dispersing countless small micro fibers of mango. It seemed as the potato and carrot were more brittle and partly or completely break when subjected to high stresses. The mango seemed to be more sensitive towards shearing as fruit flesh is being torn off, but resistant towards collisions. It is therefore not sufficient to alone examine the level of stress subjected to the particles without knowing their micro structural composition and mechanism of breakage.

7

Conclusion and future work

7.1 Conclusion

As the experiments did not show any conclusive results of particle breakage due to the pipe restriction, no definitive conclusion could be drawn in the comparison. The simulations visualized different phenomena occurring and particle behaviour that was considered realistic when comparing it to the high speed videos from the experiment. Three main phenomena were identified from the simulations as, shearing and squeezing of the particles as they enter the contraction. As well as collision, either particle-particle or particle-wall collision. Shearing subjected the particles to the lowest stress magnitude but affected a large part of the particle. It occurs every time a particle enters the contraction and is due to the acceleration of the flow field. No trend in either stress magnitude or volume influence could be seen for the squeezing phenomena, but did in a few cases provide the highest stress magnitude. It occurred rather infrequent in comparison to collision. The collision phenomena varied depending on number of contact points and contact area between the solids. This meant that there was a major variation in volume influence. The stresses were however in a fairly even range for both pipe restriction geometries.

The experiments showed that the different particle materials seemed to have different mechanisms of breakage. The potato and carrot showed more chipping and/or splitting, while the mango showed more tearing of the outer layer of fruit flesh. This seems to indicate, due to the difference in break mechanism, that each sample were sensitive to different phenomena. It is hypothesized that the potato and carrot are more brittle and sensitive towards high localized stresses, as seen in collision or perhaps squeezing. The mango seemed to be more sensitive to shear and squeezing as it affected the outer layer and a majority of the particle volume. When studying particle integrity in fluid flow it is thus important to consider the micro-structure and fracture mechanics of the particle in order to predict and identify areas of concern.

In both pipe geometries the expansion showed to have the most frequent peaks in stress exerted on the particles. These were concluded to be caused mainly by particle-particle collision. The collisions were much more frequent and subjected the particle to a higher stress in the 16 mm pipe. This was due to the formation of recirculations zones after the expansions. This lead particles to collide with high

relative velocities thus subjecting them to high stresses. This was initially thought to cause breakage of the particles when comparing to measured Bio-yield stress from compression test. This could not be confirmed from the experiments. This flow situation should however be avoided as it creates relatively violent and unpredictable particle behaviour and motion. More gentle expansion slope or a smaller size ratio between the small and large pipe section are possible options to avoid this issue.

The modelling of deformable particles in the IBOFlow software is thought to be accurate with some limitations. The limitation in choice of Young's modulus due to stability issues proved difficult to mend. As numerical stability was achieved the simulation proved to be realistic and stable. The simulations are assumed to provide accurate predictions of the overall stress field subjected to the particles with regards to the strain energy. Some reservation towards the predicted maximum stress level should be taken as it could not be confirmed from reality. The Young's modulus was a factor 10^3-10^5 higher than reality depending on sample, therefore the deformation of the particles is incorrect. The magnitude of the CFL number proved to impact the simulation heavily in various ways and needed consideration when choosing the set-up. The simulation time was relatively long for the case with the 16 mm pipe, in order to obtain a sufficient length in real time. This was due to a shorter time step required to maintain an acceptable CFL number. The time per iteration was also longer for the 16 mm pipe as it had a more extreme flow case compared with the 26 mm pipe. Optimization in domain size and simulation initiation are possible actions that could be taken to decrease the computational cost and required total simulation time. Overall the software performed well and made some important observations possible. From this, the main phenomena that is hypothesized to be of importance towards particle integrity could be identified together with the stress field and magnitude. This has major implications towards industrial applications. If crucial areas in a system and component can be identified it can possibly be redesigned with regards to geometry or flow case to reduce or eliminate these situations. Even though it had a relatively long simulation time, can be both more time and cost effective than performing real experiments but requires expertise in the area. Experiments are still necessary for validation and confirmation. As development for both hardware and software is continuously made to improve multiphase simulation capabilities and cost efficiency, it may play a significantly more important part in the future.

In conclusion, the simulation model seemed to accurately predict the behaviour of both particles and fluid flow with some limitations. It proved to be a good way to identify different phenomena and their characteristics that occurs and visualize the overall behaviour. It has a wide field of potential application in industry and is highly useful in R&D exploration and development. As no clear conclusion of breakage could be drawn between simulations and experiments, the pipe contraction does not seem to have a significant affect. It is therefore assumed that flow situations of this kind in a pipe restriction in industrial applications does not have a significant impact on the particle integrity.

7.2   Future work

In the study of the Rayleigh damping, it showed issues of numerical instabilities depending on set-up. It is hypothesized that these instabilities are linked to the eigenfrequency of the solid material. A possible continuation might therefore be to investigate how the eigenfrequency affects the numerical oscillations in the system. Another point could be to investigate the validity of using Rayleigh damping in applications with particles with low Young's modulus. Other numerical available numerical methods for damping might perhaps prove to be more suitable.

If the numerical instabilities could be resolved such that a lower Young's modulus could be used, further investigation towards material model should be conducted. With more experimental data the standard deviation could possibly decrease and it would give a more clear indication of which material model is best suited for each case. This would open another wide area of study, a more correct deformation of the particles. It would allow to more accurate study the actual deformation of the particles during specific events. It could also give some insight into what mechanism of fracture is likely to occur as the deformation process could be investigated.

From the mesh dependence study a number of important parameters were discovered to have a significant impact on the accuracy of resolving the contact between solid objects. This results showed and indicated that for the selected parameters the numerical framework was stable and provided accurate predictions of both behaviour and stresses. To confirm this further and more extensive studies in this area need to be made.

The pipe restriction showed to have a negligible effect on the particles integrity. It was discovered from the experiments that the agitation in the tank and the pump had the most effect. It might therefore be of interest to model and perform simulations on these systems and compare with behaviour and stress level from simulations on the pipe restriction. Other components thought to have an impact on particle integrity that are found in a processing line could also be investigated, such as valves or T-junctions. The simulation model developed in this work could be used directly. This could provide fast insight into if the system or component in question is likely to have an affect in the particles integrity. This could speed up the research process to the point where the particles are expected to break. At that point the simulation could be improved by tailoring it towards the specific system.

Bibliography

[1] J. Crank and P. Nicolson. "A practical method for numerical evaluation of solutions of partial differential equations of the heat-conduction type". In: *Mathematical Proceedings of the Cambridge Philosophical Society* 43.1 (1947), pp. 50–67. DOI: 10.1017/S0305004100023197.

[2] N. M. Newmark. *A method of computation for structural dynamics*. Department of Civil Engineering, University of Illinois, 1959.

[3] C. S. Peskin. "Flow patterns around heart valves: A numerical method". In: *Journal of Computational Physics* 10.2 (1972), pp. 252–271. DOI: 10.1016/0021-9991(72)90065-4.

[4] J. P. van Doormaal and G. D. Raithby. "Enhancements of the SIMPLE Method for Predicting Incompressible Fluid Flows". In: *Numerical Heat Transfer* 7 (Apr. 1984), pp. 147–163. DOI: 10.1080/01495728408961817.

[5] N. Wang and J. Brennan. "Changes in structure, density and porosity of potato during dehydration". In: *Journal of Food Engineering* 24.1 (1995), pp. 61–76. ISSN: 0260-8774. DOI: https://doi.org/10.1016/0260-8774(94)P1608-Z. URL: http://www.sciencedirect.com/science/article/pii/0260877494P1608Z.

[6] H. Hu. "Direct simulation of flows of solid-liquid mixtures". In: *International Journal of Multiphase Flow* 22.2 (1996), pp. 335–352. DOI: 10.1016/0301-9322(95)00068-2.

[7] J. Mohd-Yusof. "Combined immersed-boundary/b-spline methods for simulations of flow in complex geometries". In: *Annual Research Briefs* (1997). URL: https://web.stanford.edu/group/ctr/ResBriefs97/myusof.pdf.

[8] T. J. V. Dyke and A. Hoger. "A comparison of second-order constitutive theories for hyperelastic materials". In: *International Journal of Solids and Structures* 37.41 (2000), pp. 5873–5917. ISSN: 0020-7683. DOI: https://doi.org/10.1016/S0020-7683(99)00157-2. URL: http://www.sciencedirect.com/science/article/pii/S0020768399001572.

[9] H. H. Hu, N. Patankar, and M. Zhu. "Direct Numerical Simulations of Fluid–Solid Systems Using the Arbitrary Lagrangian–Eulerian Technique". In: *Journal of Computational Physics* 169.2 (2001), pp. 427–462. DOI: 10.1006/jcph.2000.6592.

[10] G. Kalitzin and G. Iaccarino. "Toward immersed boundary simulation of high Reynolds number flows". In: (Dec. 2003), pp. 369–378. URL: https://apps.dtic.mil/dtic/tr/fulltext/u2/p014818.pdf.

[11] C. Förster, W. A. Wall, and E. Ramm. "Artificial added mass instabilities in sequential staggered coupling of nonlinear structures and incompressible viscous flows". In: *Computer Methods in Applied Mechanics and Engineering* 196.7 (2007), pp. 1278–1293. ISSN: 0045-7825. DOI: https://doi.org/10.1016/j.cma.2006.09.002. URL: http://www.sciencedirect.com/science/article/pii/S0045782506002544.

[12] A. Mark and B. G. van Wachem. "Derivation and validation of a novel implicit second-order accurate immersed boundary method". In: *Journal of Computational Physics* 227.13 (2008), pp. 6660–6680. ISSN: 0021-9991. DOI: https://doi.org/10.1016/j.jcp.2008.03.031. URL: http://www.sciencedirect.com/science/article/pii/S0021999108001770.

[13] S. Krenk. *Non-linear modeling and analysis of solids and structures*. Cambridge University Press, 2009.

[14] W. Timberwolf. Mar. 2010. URL: upload.wikimedia.org/wikipedia/commons/2/20/Octree2.svg.

[15] A. Mark, R. Rundqvist, and F. Edelvik. "Comparison Between Different Immersed Boundary Conditions for Simulation of Complex Fluid Flows". In: *FDMP: Fluid Dynamics & Materials Processing* 7.3 (2011), pp. 241–258. URL: http://www.techscience.com/fdmp/.

[16] C. T. Crowe, J. D. Schwarzkopf, M. Sommerfeld, and Y. Tsuji. *Multiphase flows with droplets and particles*. 2nd ed. CRC Press, 2012.

[17] G. Hou, J. Wang, and A. Layton. "Numerical Methods for Fluid-Structure Interaction — A Review". In: *Communications in Computational Physics* 12.2 (2012), pp. 337–377. DOI: 10.4208/cicp.291210.290411s.

[18] M. Machado, P. Moreira, P. Flores, and H. M. Lankarani. "Compliant contact force models in multibody dynamics: Evolution of the Hertz contact theory". In: *Mechanism and Machine Theory* 53 (2012), pp. 99–121. ISSN: 0094-114X. DOI: https://doi.org/10.1016/j.mechmachtheory.2012.02.010. URL: http://www.sciencedirect.com/science/article/pii/S0094114X1200047X.

[19] E. Svenning, A. Mark, and F. Edelvik. "Simulation of a highly elastic structure interacting with a two-phase flow". In: *Journal of Mathematics in Industry* 4.1 (2014), p. 7. DOI: 10.1186/2190-5983-4-7.

[20] A. Y. Petrov, P. D. Docherty, M. Sellier, and J. G. Chase. "Multi-frequency Rayleigh damped elastography: in silico studies". In: *Medical Engineering & Physics* 37.1 (2015), pp. 55–67. ISSN: 1350-4533. DOI: https://doi.org/10.1016/j.medengphy.2014.10.007. URL: http://www.sciencedirect.com/science/article/pii/S135045331400277X.

[21] Y. Pan and Z. Zhong. "A viscoelastic constitutive modeling of rubber-like materials with the Payne effect". In: *Applied Mathematical Modelling* 50 (2017), pp. 621–632. ISSN: 0307-904X. DOI: https://doi.org/10.1016/j.apm.2017.06.018. URL: http://www.sciencedirect.com/science/article/pii/S0307904X17304109.

[22] P. Balasubramanian, G. Ferrari, and M. Amabili. "Identification of the viscoelastic response and nonlinear damping of a rubber plate in nonlinear vibration regime". In: *Mechanical Systems and Signal Processing* 111 (2018), pp. 376–398. ISSN: 0888-3270. DOI: https://doi.org/10.1016/j.ymssp.2018.03.061. URL: http://www.sciencedirect.com/science/article/pii/S0888327018301882.

[23] W. Kim, I. Lee, and H. Choi. "A weak-coupling immersed boundary method for fluid–structure interaction with low density ratio of solid to fluid". In: *Journal of Computational Physics* 359 (2018), pp. 296–311. ISSN: 0021-9991. DOI: https://doi.org/10.1016/j.jcp.2017.12.045. URL: http://www.sciencedirect.com/science/article/pii/S0021999118300056.

[24] M. Ottosson. "Coupling Algorithms for Fluid Structure Interaction at Low Density Ratios". MA thesis. Chalmers University of Technology, 2018. URL: http://studentarbeten.chalmers.se/publication/256396-coupling-algorithms-for-fluid-structure-interaction-at-low-density-ratios-accuracy-and-stability-ana.

[25] N. K. Jha, U. Nackenhorst, V. S. Pawar, R. Nadella, and P. Guruprasad. "On the constitutive modelling of fatigue damage in rubber-like materials". In: *International Journal of Solids and Structures* 159 (2019), pp. 77–89. ISSN: 0020-7683. DOI: https://doi.org/10.1016/j.ijsolstr.2018.09.022. URL: http://www.sciencedirect.com/science/article/pii/S0020768318303780.

[26] J. Roland and N. Tuck Hutasingh. "Development of food particle characterization method." MA thesis. Lund University, Department of Food Technology, Faculty of Engineering, 2019.